Kobe University Repository : Kernel

PDF issue: 2026-11-22

Spatial patterning and morphogenetic mechanism of cephalic furrow formation during Drosophila gastrulation

Eritano, Anthony Stephen

(Degree)
博士（理学）

(Date of Degree)
2020-03-05

(Date of Publication)
2021-03-01

(Resource Type)
doctoral thesis

(Report Number)
乙第3383号

(URL)
https://hdl.handle.net/20.500.14094/D2003383

※ 当コンテンツは神戸大学の学術成果です。無断複製・不正使用等を禁じます。著作権法で認められている範囲内で、適切にご利用ください。

Doctoral Dissertation

Spatial patterning and morphogenetic mechanism of

cephalic furrow formation during *Drosophila* gastrulation

(ショウジョウバエ原腸胚 cephalic furrow 形成における

空間的パターンと形態形成機構)

January 2020

Graduate School of Science, Kobe University

Anthony Stephen Eritano

Abstract

Background

Establishment of complex biological structures is crucial for embryonic development. These complex structures are form during morphogenesis through dynamic remodeling and folding of epithelial tissues. It is important that these folding and remodeling events can be faithfully reproduced spatially and temporally throughout the population of an organism. While robust morphogenesis is common during embryonic development, the mechanism that underlie this robustness are poorly understood. Robustness of morphogenetic processes relies on the establishment and maintenance of a genetic pattern, which dictates cell behaviors. Next, the cells must interpret the information provided by the genetic pattern. The establishment of the genetic pattern has been shown to be highly refined and spatially precise (Bentovim et al., 2017; Lagha et al., 2012). Additionally, some aspects of embryonic growth and shape changes have been shown to exhibit some level of self-correcting properties (Aliee et al., 2012; Hong et al., 2008; Xiong et al., 2013; Yevick et al., 2019). But it is unclear how morphological precision stems from the apparent spatial information. Specifically, it is unknown if the mechanisms involved in epithelial morphogenesis possess the same kind of self-correcting system that ensures proper morphological events and faithfully interpret the genetic pattern.

Results

In this study, my coauthors and myself conducted a systematic, multiscale characterization of cephalic furrow formation in the *Drosophila* embryo on a genetic, cell, and tissue scale. By revisiting the known genetic network that regulates cephalic furrow initiation, I have identified additional regulatory elements that further refine the spatial pattern of the cephalic furrow, thus

generating highly precise spatial information. Fixed and live imaging analysis on the cellular level shows that cephalic furrow initiation cells display two distinct cell behaviors that are spatially and temporally heterogeneous. However, we found that 80% of these initiating events are specified by the positional information generated by the genetic pattern. The remaining 20% of mis-specified initiation events are attributed to heterogeneous and fluctuating myosin behavior on the cellular scale. Despite this 20% misspecification, a linear cephalic furrow is formed. We also identified a novel myosin behavior in which myosin is localized to the lateral surface of the initiating ells and drives the shrinkage of the lateral membrane. On a tissue scale, the lateral myosin becomes enriched and planar polarized to form supracellular ribbons across the tissue. Using laser ablations and optogenetics, we have shown that the initiating cells are mechanically coupled to each other.

Conclusion and discussion

From this work, I have shown that precise spatial information generated by the genetic patterning of the embryo is vital for ensuring not only the location of cephalic furrow development but also providing necessary cues that lead to specific types of cell behaviors. Despite this precise positional information, heterogeneity in cell behavior still exists in the cells. Removal of this “noise” is accomplished by the mechanical coupling on the initiating cells on the tissue scale. Through this coupling of cells on the tissue scale, the embryo can ensure morphogenetic precision is preserved and consistent despite developmental noise generated during the interpretation of positional information.

Definitions and abbreviations

CF: Abbreviation for Cephalic furrow

DF: Abbreviation for Dorsal folds

VF: Abbreviation for Ventral furrow

GBE: Abbreviation for Germband extension

Btd: Abbreviation for the transcription factor Buttonhead

Eve(N): Abbreviation for the transcription factor Even-skipped. Individual stripes of Even-skipped are indicated by the numeral following “Eve” (i.e. Eve1 indicates the first stripe of Even-skipped).

P(N): The designation system used to identify nuclei position based on the expression of Eve. The cell containing the highest level of nuclear Eve is designated at P(0). This unified system allows for the alignment of cells for cross embryo analysis

Interface(N): The unified system used to identify and designate the membrane interfaces between the cells involved in cephalic furrow formation. Interface(0) is defined as the lateral membrane that is anterior to the P(0) cell.

Ribbon: In this thesis, Ribbon is defined as the phenomenon visualized on the tissue scale of the cephalic furrow. The “Ribbon” represents the planar polarized enrichment of myosin along interface(0) in a 3-dimensional view.

Initiating cell: An epithelial cell that undergoes cell shortening and leads to the start of cephalic furrow invagination

Initiating behavior: The differential cell shortening behaviors seen in initiating cells

Initiating event(s): a term used to identify initiating cells within the epithelial tissue

Cephalic furrow initiation: the behavior of initiating cells undergoing cell shortening

A-P axis: abbreviated designation for the anterior posterior axis of the embryo

D-V axis: abbreviated designation for the dorsal ventral axis of the embryo

Noise: a term used to represent the heterogeneity of cell behaviors that is the result of misinterpretation of positional information, or differential behavior of myosin activity between individual cells.

Table of Contents

Chapter 1: Introduction 9

Pattern formation and tissue morphogenesis in the gastrulating *Drosophila melanogaster* embryo 10

Development of the early *Drosophila melanogaster* embryo 10

Establishment of the embryonic genetic pattern 11

Morphogenesis during *Drosophila melanogaster* gastrulation 13

Cephalic furrow, a precisely position epithelial fold that is formed by an unknown mechanism and has an unknown function 14

Mechanical mechanisms of epithelial folding 16

The mechanics of epithelial folding 17

Tissue-scale epithelial mechanics 21

Precision of embryonic patterning and morphogenesis in the *Drosophila* embryo 23

Precision in the genetic patterning of Drosophila embryo 24

About this thesis 25

Chapter 2: Methods and materials 28

Drosophila strains and genetics 28

Generation of TRAP lines (pTRAP) 29

Generation of Btd misexpression lines (pMIST) 30

Generation of the Eve-LlamaTag line via CRISPR/Cas9 genome editing 31

Immunofluorescence and fixed imaging 32

Live imaging 33

Laser ablation 35

Optogenetics 35

Purification and Western blot of GFP-tagged ribosomes 36

Theoretical estimate of RMSE 37

3D vertex modeling 38

The model 38

Patterning of cell mechanics 40

Model settings for simulation of spatial and temporal noise: conditions at the tissue boundaries, spatially patterned differential tension, and noise introduction 41
Quantification of tissue morphology: cell alignment and tissue fold depth 42
Summary of parameter values used in the simulations 42

Quantification and Statistical Analysis 43
Image processing and quantification 43
Live imaging time alignment 44
Cell tracking and analysis for in toto SPIM time-lapse data 44
Cell membrane interface tortuosity analysis 45
Identification of the initiation types in en face imaging 45
Cell-by-cell intensity analysis of Eve and Btd in 3D 46
Identification of type I and II events, and P(0) position mapping 47
Assay for the linearity of P(0) and CF cleft positions 48
Classification of type III+ initiation events 48
Quantitation of MyoII at the lateral interface in the coronal images 48
Estimation of total, apical and lateral lengths of interface in coronal images 49
Quantitative analysis for the laser ablation experiments 49
3D rendering of P(0) cells, interface (0) “ribbon”, and MyoII foci 50
Tissue-scale MyoII intensity analysis 51
Analysis of Eve-LlamaTag and MyoII-mKate2 in live and fixed embryos 52
Comparison of CF and GB MyoII intensity and polarization 53
Straightening and angle analysis of the interconnected interface “ribbons” 54
Unwrapping and 3D tortuosity analysis 55
Analysis and quantitation for the optogenetic experiments 56
Statistical Analyses 58

Chapter 3: Spatial patterning and refinement of morphogenetic noise during CF formation during Drosophila embryogenesis 59

Introduction 59

CF initiation is temporally and spatially heterogeneous 60

Differential interface shortening manifests as two morphologically distinct cell shape changes 62

The CF genetic network generates positional information with single-cell row resolution, which restricts the number of initiating cells 64

CF initiation behaviors obey the Btd/Eve positional code with 80% precision 67

The initiating cells linearly align among themselves, irrespective of deviation from the CF positional code 68

Interface shortening is associated with lateral myosin contractility....70

Lateral MyoII enrichment is planar polarized and appears to straighten the supracellular 3D “ribbons” of interconnected interfaces....71

MyoII variabilities do not scale with patterning noise....72

CF initiation requires the local activity of Btd and Eve, each of which plays a distinct role in the control of MyoII behaviors....74

Force transmission between interfaces across adherens junctions underlie CF spatial alignment....76

Local reduction of myosin contractility via optogenetics temporarily disrupts mechanical continuity and increases imprecision in CF spatial alignment 78

3D vertex modeling reveals that a CF-like mechanical system is robust against spatial and temporal noise....80

Conclusion 82

Chapter 4: Pursuit of cellular effector genes that are downstream of the Btd/Eve regulatory circuit....84

Introduction 84

Region-specific expression of GFP-tagged ribosomes in the early *Drosophila* embryos....86

Development of an isolation and purification protocol for GFP-tagged ribosomes from the *Drosophila* embryos....88

Conclusion 89

Chapter 5: Examination of the function of the CF 90

Introduction 90

Localized requirement of Eve expression for CF initiation....91

Analysis of the spatial contribution of Eve on MyoII regulation in CF and GBE regions 92

Analysis of phenotypes associated with mis-expression of Btd....93

Conclusion 96

Chapter 6: Future directions 97

Refinement of translatome analysis....97

Identify the role of the cephalic furrow during embryogenesis and its evolutionary function through ectopic furrow formation 99

Embryonic influence on cephalic furrow initiation events 100
Chapter 7: General discussion....101
Tissue-scale mechanical coupling as a denoising mechanism 101
The mechanical system underlying cephalic furrow formation 103
Evolutionary significance of the cephalic furrow....105
References 107
Acknowledgements 116
Figure legends 118
Main figures legends 118
Supplemental figure legends 130
Movie figure legends 138
Figures....140

Chapter 1: Introduction

A cornerstone of developmental biology is understanding how organisms gain complex 3D structures from morphologically uniform cells. Higher organisms develop specialized tissue architecture and organ systems, each of which serves an important function for the survival of the organism. The tissues and organs possess precise 3D shape and size to ensure proper function. Failure to obtain these characteristics can have devastating consequences. To ensure precision in the formation of complex structures, organisms must establish genetic and morphological mechanisms that can ensure that the accuracy and robustness in the process of development. Although developmental precision is a well-recognized concept, how this is accomplished has only been partially understood.

In this dissertation research, I focus on revealing the mechanistic principle underlying the formation of cephalic furrow (CF), an epithelial fold structure, that is formed during the early embryonic stage of *Drosophila melanogaster*. To help readers better appreciate the subject of this research, I will first in this Introduction provide a general description of the context in which the CF is formed, including the spatial patterning and the developmental processes that occur prior and during CF formation. This will be followed by a brief review of the published results on CF formation prior to this thesis work. In addition to these two sections of specialized background information, I will present two sections of general consideration, one on the mechanics of epithelial folding and another on the conceptual understanding of morphogenetic precision, as these represent the central concerns of this research. This chapter will end with a general summary of the ensuing chapters that follow.

Pattern formation and tissue morphogenesis in the gastrulating *Drosophila melanogaster* embryo

Development of the early *Drosophila melanogaster* embryo

Drosophila melanogaster is an excellent model organism to examine genetic patterning and morphogenesis. Over the years, researchers have established various protocols that allow for the genetic manipulation of the embryo (Gyoergy et al., 2018). Additionally, the development of *Drosophila melanogaster* has been studied and mapped from oogenesis to the adult (Bate and Arias, 1993; Campos-Ortega and Hartenstein, 1997). For this thesis, I will focus primarily on the development of the embryo from fertilization to gastrulation.

At the time of fertilization, the *Drosophila* embryo is a single cell in which the nucleus undergoes 13 rounds of cell division (Sung et al., 2013). During these cell divisions, the embryo becomes a syncytial blastoderm, where the dividing nuclei are contained within a common cytoplasm (Sung et al., 2013). By the 10^{th} round of cell division, the nuclei have migrated to the periphery of the embryo and form a single monolayer (Foe and Alberts, 1983). After the 13^{th} round of cell division, individual nuclei become enclosed in membrane in a process known as cellularization, resulting in the formation of single layer of cells that encircles the yolk (Foe and Alberts, 1983; Lecuit and Wieschaus, 2000).

The completion of cellularization generally coincides with the onset of gastrulation. During gastrulation, the now cellularized monolayer undergoes morphological movements that will give rise to the primary germ layers of the embryo (Leptin, 1995). The morphological movements that occur during gastrulation are stereotypical, occurring in precise locations at precise times (Ferree et al., 2016). These consistent and reliable morphological movements offer a robust and

outstanding system to study the complex interplay between patterning and morphogenetic events.

Establishment of the embryonic genetic pattern

Genetic patterning of the developing embryo is a highly complex and intricate process. Countless amounts of research have gone into understanding how the genetic pattern is formed. The *Drosophila* embryo is patterned by a hierarchical system of gene regulation and expression that undergo successive levels of genetic refinement. Below, I will briefly summarize these elements to provide the necessary background information for the understanding of the factors and procedures that are relevant to the spatial patterning of CF formation.

Establishment of A-P and D-V coordinate systems during *Drosophila* oogenesis

Patterning of the *Drosophila* embryo begins during oogenesis during which three global, maternal coordinate systems are established. At the mid-stage egg chamber, the first maternal coordinate system is established for the anterior-posterior axis (A-P axis) via the localization of *bicoid* and *gurken* mRNA to the anterior pole of the developing egg; in addition to *oskar* and *nanos* mRNA to the posterior pole of the developing egg (Kugler and Lasko, 2009). Following this, the localization of *gurken* mRNA and *torpedo* mRNA (ligand and receptor for EGF signaling respectively) (Figure1.1B, Ovary) to the dorsal aspect of the anterior pole sets up the second maternal coordinate system that gives rise to the dorsal-ventral axis (D-V axis) (Schüpbach and Roth, 1994). By the time the oocyte matures, the A-P and D-V axes are established within the oocyte.

Refinement of the A-P spatial pattern

After the establishment of the A-P and D-V coordinate system in the oocyte, upon fertilization, the A-P genetic patterning is further refined through a hierarchy of genetic regulation. The first

level of regulation is based on the expression of the maternal genes that were loaded into the oocyte. The maternal genes Bicoid and Nanos establish the anterior and posterior regions of the embryo, respectively, through gradients of expression from their respective regions (Figure 1A, maternal morphogen gradients). Through genetic feedback and regulation, the Bicoid and nanos gradients give rise to the next layer of patterning genes called the gap genes.

The gap genes are a set of zygotically expressed transcription factors that specify broad, but localized patterns along the A-P axis of the embryo (Figure 1A, gap genes).The core gap genes comprise of Hunchback (hb), Giant(gt), Krüppel (Kr), Kirps (kni) and Caudal (Cal) in the embryonic region that gives rise to the future trunk, and Buttonhead (Btd) in the region that give rise to the future head (Wimmer et al., 1995, 1997). The expression of these gap genes is refined through positive and negative feedback regulation with the maternal genes and other gap genes, leading to highly defined spatial expression and patterning of the embryo. Through the defined spatial expression of the gap genes, the next layer of gene expression is generated, known as the pair-rule genes. Pair-rule genes are also zygotically expressed transcription factors that help to establish the genetic pattern of individual segments of the Drosophila body plan (Figure 1A, pair-rule genes). Unlike the gap genes, the pair rule genes are expressed in spatially periodic domains through the trunk of the embryo (Baumgartner and Noll, 1990). Notable pair rule genes include Even-skipped (Eve), hairy (H), odd-skipped (odd), and runt (run) (Clark, 2017). Similar to the gap genes, the pair rule genes are spatially refined through feedback interactions with the gap genes and with other pair rule genes. These pair rule genes help dictate the individual behaviors of specific cell populations.

Refinement of the D-V spatial pattern

On the ventral aspect of the embryo, the high level of Dorsal expression activates the expression of the transcription factor Twist (twi) and the downstream target of twi, Folded

Gastrulation (fog) (Sandler and Stathopoulos, 2016) (Figure 1B, Embryo). The ventral localization of Twist and the expression Folded gastrulation will trigger the formation of the ventral furrow and germband extension, which I will discuss in the next section of this chapter.

Establishment of anterior and posterior poles through the terminal coordinate system

The terminal system helps establish the pole regions of the embryo through the localized activation of the membrane receptor called Torso (tor), via the Perforin- like protein torso-like (tsl) (Henstridge et al., 2014; Nüsslein-Volhard, 1991). Local activation of Torso results in the expression of the downstream gap genes huckebein (hkb) and tailless (tll) (Weigel et al., 1990). Tailless also regulates the expression of folded gastrulation, which provides genetic cues needed for the cell behaviors required for the invagination of posterior midgut, the presumptive endoderm (St Johnston and Nüsslein-Volhard, 1992).

Morphogenesis during *Drosophila melanogaster* gastrulation

With the establishment of the genetic pattern throughout the embryo, the embryo then interprets this pattern to initiate morphogenesis. Upon the start of gastrulation, key morphological events help give rise to the primary germ layers of the embryo. While the ectoderm is mainly comprised of cells that remain on the surface of the embryo, the formation of the mesoderm and endoderm involve complex and highly coordinated movements of epithelial invagination.

Internalization of the presumptive mesoderm cells is driven by a morphological event known as the ventral furrow (VF) (Conte et al., 2009; Sweeton et al., 1991)(Figure 1C). The VF is one of the first epithelial folds that occur at the onset of gastrulation in which cells along the entire ventral surface of the embryo invaginate into the embryo (Campos-Ortega and Hartenstein, 1997). The invagination of the ventral epithelial tissue is regulated by the expression of fog, which triggers the cell shape change required for invagination (Dawes-Hoang et al., 2005).

These internalized cells delaminate from the epithelial layer and further differentiate to form the mesoderm of the embryo (Sweeton et al., 1991). Linked to the formation of the mesoderm, the formation of the presumptive endoderm is driven by the internalization of the posterior midgut (PMG) (Reuter et al., 1993). Both PMG and VF share a similar process of cell shape change leading to the internalization of the endoderm and mesoderm, respectively (Lye et al., 2015) (Figure 1.1D). Additionally, the invagination of the PMG pulls on the ventral cell populations and, with the cell convergence extension behavior in the extension of the germband (Figure1.1D, blue overlay and yellow arrow), helps with the internalization of mesoderm cells (Lye et al., 2015).

One other morphological event that occurs at the same time as the VF, is the cephalic furrow (CF) (Campos-Ortega and Hartenstein, 1997). Despite its prominent presence on the lateral surface of the gastrulating embryo, little work has been done on the cell behaviors, mechanics, and function of the CF. Below, I will summarize published data on the morphological processes that underlie the formation of the CF.

Cephalic furrow, a precisely position epithelial fold that is formed by an unknown mechanism and has an unknown function

The cephalic furrow (CF) is a large epithelial fold that appears at the onset of gastrulation, along with the VF. The CF is a linear structure that forms in a very stereotypic manner, forming at the same position throughout the population of *Drosophila melanogaster* (Campos-Ortega and Hartenstein, 1997). It is formed at ~33-34% of the embryo length from the anterior pole (Liu et al., 2013). Formation of the CF is marked by the appearance of a shallow groove on the lateral surface of the embryo (Spencer et al., 2015; Vincent et al., 1997). As gastrulation progresses, the CF rapidly increases in depth and eventually forms a ring around the entire embryo (Spencer et al., 2015). Interestingly though, as gastrulation comes to an end, the CF begins to

retract back to the surface of the embryo. Thus, the CF is a transient epithelial fold that neither the initial folded architecture is retained, nor does it contribute to an eventual tissue or organ structure (Campos-Ortega and Hartenstein, 1997).

Previous work has stablished the genetics responsible for CF formation. An important genetic regulator that controls the positioning of the CF is the expression of the maternal loaded gene *bicoid* (Bcd). When the expression of Bcd is altered, the position of the CF shifts accordingly; showing that the spatial position of the CF is dependent on the A-P patterning system of the embryo, and more specifically, the dosage of Bcd (Driever and Nüsslein-Volhard, 1988a; Liu et al., 2013). Further work has shown that two zygotically expressed transcription factors downstream of Bcd the gap gene *buttonhead* (Btd) and the paired-rule gene *even-skipped* (Eve), are necessary for CF formation (Vincent et al., 1997). Importantly, it is the overlapping expression of Btd and the first stripe of Eve (Eve1) that marks the location of CF initiation (Vincent et al., 1997). This suggests that the formation of the CF is tightly controlled by the spatial pattern generated by the A-P patterning system.

Downstream of these transcription factors, the mechanical mechanism of CF formation, however, remains largely unknown. Prior analysis suggested that CF initiation begins with the shortening of a single cell in the epithelial layer (Spencer et al., 2015; Vincent et al., 1997). Additionally, it was reported that the initiation event is associated with an increase of F-actin, but not the actin motor MyoII, which will be explained in a later section, (Spencer et al., 2015). There has thus far been a lack of functional analysis on either actin or myosin, however, nor has any connection been made between the upstream transcription factors and the cytoskeletal components that may be involved in the initiation of these cell shape changes. The theoretical analysis of CF formation has been equally murky. Numerical modeling suggests that initiation of the CF is similar to the initiation of the VF (Allena and Aubry, 2012). But this model made a key assumption that CF initiating cells behaves like the VF cells, an assumption that lacks empirical

evidence. Taken together, there remains a lack of understanding on the mechanics that underlie CF initiation prior to this thesis work.

Unlike the other epithelial folds, the function of the CF remains largely unstudied. Given the transient nature of the CF it is difficult to determine what the actual function the CF serves. Classic fate map analysis of the Drosophila embryo suggest that the cells within the CF do not constitute a distinct cell fate (Hartenstein and Campos-Ortega, 1985), indicating that the cells that are specified and form the CF are not ultimately contributing to the establishment of a fate restricted structure in the embryo. Based on the spatial position of the CF, it is suggested that the CF is responsible for the demarcation of the presumptive head from the presumptive thorax and is potentially required to establish a more detailed segmentation field (Costa et al., 1993). Another suggested role for the CF is to provide an anchor for the anterior most cells on the ventral surface and directs the germband to extend only posteriorly (Costa et al., 1993). Computational modeling of cell geometry provides numerical supports the possibility that the CF could be acting as a barrier that guides cell flow from the GBE posteriorly (Dicko et al., 2017). But *in vivo* analysis has not been performed to test any of these hypotheses.

Mechanical mechanisms of epithelial folding

Epithelial folding requires coordinated changes in cell and tissue behavior. The changes in cell and tissue behaviors during epithelial folding typically require force generation and transmission. Two of the key players are non-muscle myosinII (MyoII) (Martin and Goldstein, 2014; Sawyer et al., 2010), and the adherens junction complex (AJ) (Badouel and McNeill, 2009).

MyoII is part of a larger superfamily of motor proteins which are known for their role in the contraction of muscles (Squire et al., 2017). Members of the myosin superfamily share common behaviors, such as exerting power strokes on the actin cytoskeleton as well as cross-linking the

actin filament (Vale and Milligan, 2000). These allow to generate contractile forces on the actin meshwork, which, when linked to cellular structure, can cause changes in the cell shapes. MyoII is predominant form of myosin in the epithelial cells. During epithelial cell shape change, MyoII is often found at the cell cortex, causing localized contraction of membrane surfaces (Heer and Martin, 2017; Munjal and Lecuit, 2014).

While MyoII has been shown to be the source of the forces that lead to changes in cell shape, the adherens junction (AJ) also plays a key role in the mechanics that are responsible for cell shape changes (Badouel and McNeill, 2009). The AJ is an area located on the apical most region on lateral surface of epithelial cells (Farquhar and Palade, 1963). The AJ is comprised of multiple components necessary for the adhesion and force transmission between neighboring cells (Lecuit and Yap, 2015). A key component and marker of the AJ is a protein called α-Catenin (αCat), which is the cytoplasmic linker between the actomyosin network and the adheren proteins that connect the cells (Yonemura, 2011). The mechanics that underline epithelial morphogenesis, and epithelial folding in particular, can be examined both at the cellular-scale and the tissue-scale. I will discuss these in succession.

The mechanics of epithelial folding

The morphological events seen during gastrulation are the result of changes in the epithelial tissue layer. Underlying the changes are changes of individual cell behaviors within the epithelial tissue (Davidson, 2012). These changes in individual cells can range from altering the height of the cells through cell shortening or elongation, or more localized changes such as shrinkage of the apical surface of the cells, or the relaxation of the basal surface (Davidson, 2012; Pearl et al., 2017). The cellular mechanisms that drive epithelial folding can be roughly classified into four categories. 1) Apical constriction dependent mechanisms, in which the primary mechanism is the shrinkage of the apical surface via MyoII, 2) Apical constriction

independent mechanisms, where MyoII activity is not observed at the apical surface of the cell, but controls cell shape change via other mechanisms, and lastly, 3) Myosin independent mechanisms, in which the mechanisms are not driven by MyoII activity, but are the result of other cellular forces.

Apical constriction dependent mechanism

A classic and well-studied example of an apical contraction dependent mechanism is the formation of the ventral furrow (VF). During VF formation, the expression of Fog across the ventral surface of the embryo causes the apical localization of MyoII to the apical surface of the initiating cells and activates Rho kinase activity, which activates the contractility of MyoII (Dawes-Hoang et al., 2005). At the apical surface of the cell, MyoII pulls the outer edges of the apical surface towards the center of the apical surface, followed by a relaxation phase (Mason et al., 2013) (Figure 1.2A). This process repeats until the apical surface of the cell becomes smaller, resulting in a wedge-shaped cell. The wedge shape creates an area of decreased tissue integrity, leading to out-of-plane invagination of the epithelial layer (Martin and Goldstein, 2014).

Another well studied example of apical constriction can be seen during neural tube formation in *Gallus gallus* (chicken) embryos (Nishimura et al., 2012). During neural tube formation a region of the ectoderm, known as the neural plate, undergoes apical constriction creating “hingepoints” which allow for the deformation of the neural plate, aiding in the invagination and eventual closure of the neural tube (Haigo et al., 2003). In both VF and neural tube formation, the apical constriction is driven by MyoII behavior at the medio-apical cortex of the initiating cells (Mason et al., 2013; Nishimura et al., 2012).

MyoII dependent apical constriction has also been found during the formation of bottle cells in *Xenopus laevis* gastrulation. Bottle cells are an important population of cells that help form a

crevice at the blastopore lip (Hardin and Keller, 1988). Prior to the start of gastrulation, the bottle cells undergo apical constriction via MyoII contraction and reorganization of microtubules (Hardin and Keller, 1988; Lee and Harland, 2007). The formation of these bottle-like shape of the cells is believed to generate forces that are required for the initial blastopore formation (Lee and Harland, 2007).

Apical constriction independent mechanism

MyoII behavior is not limited to just the apical surface of the cell. Theoretical analysis suggests that folding can be induced by modulation of cellular mechanics not just on the apical, but also the basal and lateral sides of the cells (Wen et al., 2017). In addition to driving apical constriction, MyoII, or the actin cytoskeletal system through which MyoII generates forces, has also been shown to localize to the lateral membrane of cells, presumably resulting in the lateral constriction of the cell (Sherrard et al., 2010; Sui et al., 2018) (Figure 1.2B). While cell shape change is normally associated with the accumulation of MyoII at the cell cortex, cell shape change can be the result of loss of MyoII accumulation. This is the case in which relaxation of the basal MyoII meshwork allows for the expansion of the basal surface (Eiraku et al., 2011). Additionally, the loss of cells from within the tissue layer through apoptosis can drive the invagination of the tissue layer in the Drosophila leg disc (Ambrosini et al., 2019). This apoptosis driven mechanism of cell shape change is the result of the basal shift of the nuclei and the anchoring of the nucleus to the basal F-actin meshwork, which is required for the apico-basal forces within the cell (Ambrosini et al., 2019).

Myosin independent mechanism and mechanisms involving collective behavior of cells

While MyoII plays a large role in the mechanisms of cell shape change, there are situations in which cell shape change is not driven by the constrictive forces generated by MyoII. An example of a mechanism that is independent of MyoII activity can be seen during the formation of the

dorsal folds (DF) (Figure 1.2C). During initiation of DF formation, the initial cell shape change is driven by a basal shift of the AJ of the cell, which leads to the shortening of the initiating cells (Wang et al., 2012). This novel mechanism of cell shortening during DF formation was expanded upon and it was revealed that the cell shortening is likely the result from the basal shift of microtubule-based pushing forces (Takeda et al., 2018). In this situation, we have a situation where microtubules could be providing the forces required for cell shape change during epithelial folding.

In addition to the effects of cellular forces described above, folding has also been linked to the behaviors of cell collective. The forces that are involved are thus likely more complex as a multitude of cell behaviors are required. In the mouse embryo, the epithelial layer that becomes the non-neural ectoderm (ectoderm placode) receives signals from the mesenchyme underneath the ectoderm placode to give rise to structures such as the tooth, hair follicle, and mammary glands (Pispa and Thesleff, 2003). During the formation of these ectoderm derived structures, cells within the ectodermal placode delaminate apically out of the placode and extend protrusions towards the center of the placode while remaining attached to the basement membrane (Panousopoulou and Green, 2016). Upon reaching the center of the placode, the cells begin to intercalate and generates a force at the edges of the ectodermal placode towards the center of the placode, causing the buckling of the basement membrane and leading to invagination (Panousopoulou and Green, 2016).

Epithelial folding, in some cases, is controlled by a force generated from a structure that is not part of the epithelial layer that is destined to fold. During development of the Villi in the gut, the mesenchyme surrounding the epithelial layer that will form for the villi provides a compressive force on the epithelium, which restricts the expansion of the presumptive endoderm (epithelial layer) (Shyer et al., 2013). The compressive force, generated by the mesenchyme, forces the epithelial layer to buckle and fold into the developing gut lumen (Shyer et al., 2013).

Tissue-scale epithelial mechanics

While mechanical forces generated by individual cells can lead to the initiation of epithelial folding (Davidson, 2012), mechanical forces can also be generated and transmitted by the tissue itself (Martin et al., 2010). These tissue-scale mechanics rely on two key processes, 1) generation of a force and 2) propagation and transmission of the force across multiple cells. As with many cellular-scale mechanics, MyoII plays a critical role in the generation of force (Martin et al., 2010), while the AJs allow the transmission of the force to other cells (Badouel and McNeill, 2009).

Myosin dependent mechanism

One tissue-scale mechanical driver of epithelial folding is the creation of supracellular cables that spans across multiple cells within the tissue. These cables are generated through the polarized distribution of MyoII, leading to the integration and connection of MyoII contractile across the tissue surface (Kong et al., 2017; Zallen and Wieschaus, 2004) (Figure1.2D). These cables can guide cell movements, generate tissue-scale contraction forces, and help establish compartment boundaries.

A well-studied example of planar polarized MyoII cables is the extension of the germband (GBE) in the *Drosophila* embryo. During GBE, MyoII becomes preferentially enriched at the A-P

boundaries of the cells on the lateral surface of the embryo, leading to the formation of supracellular cables of MyoII that spans the D-V axis (Munjal et al., 2015). This enrichment drives T1 transitions within the tissue, which leads to the convergence and extension of the lateral surface with the assistance of a pulling force generated by the movement of the posterior midgut (Lye et al., 2015; Tada and Heisenberg, 2012).

In addition to the planar polarized MyoII cables seen in the GBE, supracellular cables can also be seen during the formation of the *Drosophila* trachea system. During trachea formation, MyoII becomes planar polarized and forms a ring like structure around the presumptive tracheal placodes, the external openings of the respiratory system (Nishimura et al., 2007). The MyoII ring exerts a contractile force that smooths the boundaries of the tracheal placode and compresses the cells in the placode towards the center (Nishimura et al., 2007). Combined with out-of-plane deformation of the tissue generated by mitosis, this compression leads to the efficient invagination of the cells into the tracheal placode (Kondo and Hayashi, 2013).

Similar to the ring like cables seen during tracheal placode invagination, MyoII rings can also be observed during tube budding from an epithelium layer in the *Drosophila* salivary glands (Roper, 2012; Sanchez-Corrales et al., 2018). During tube budding, MyoII plays multiple roles to allow for the invagination of the salivary gland placode, acting on a cellular-scale by driving the apical constriction of the cells at the center of the placode, and on the tissue-scale through the formation of circumferential MyoII cables around the border of the placode (Roper, 2012). This MyoII cable aides in the directional cell intercalation of the placode cells which guides the movement of cells towards the center of the placode (Sanchez-Corrales et al., 2018). The combination of apical constriction and guiding of cell movements via polarized MyoII rings demonstrates that MyoII can display multiple behaviors within a localized population of cells.

Transmission of forces across tissues

Propagation of a localized force to other cells within the tissue is crucial for the collective cell behavior required for epithelial folding (Vasquez and Martin, 2016). This propagation and transmission of forces is made possible through the linking of cells through adherens junctions (AJ) via the Cadherin-family of transmembrane proteins (Oda et al., 1994). A key component of the AJ is called α-Catenin (αCat), which links the AJs to the cell cytoskeleton (Yonemura, 2011). αCat has been shown to be necessary for epithelial organization and morphogenetic movements (Larue et al., 1994). During the closure of the dorsal surface of the Drosophila embryo, supracellular MyoII cables form in the lateral epidermis and surrounds the amnioserosa, which aids the closing the dorsal surface (Peralta et al., 2007). But when the MyoII cables are cut via laser ablation, the cell sheets rip apart; suggesting that tension transmission amongst the cell sheets is necessary for dorsal closure (Hutson et al., 2003; Martin et al., 2010).

Precision of embryonic patterning and morphogenesis in the *Drosophila* embryo

To ensure that necessary complex structures are faithfully reproduced across individuals within a population, organisms require a system that can refine and compensate for factors that can impact development, such as genetic variation and environmental perturbance. Through evolution, organisms have been able to compensate for these variations by the canalization of biological processes to ensure genetic processes are maintained (Hallgrimsson et al., 2019; Waddington, 1957). This canalization is derived from various mechanisms, one prominent mechanism is the establishment of redundant genetic pathways that can lead to the same physiological/phenotypic result despite environmental and genetic perturbation (Krakauer and Plotkin, 2002). Through this system, the organism can ensure that key genetic processes, such

as embryonic patterning and morphogenesis, can be consistently performed and robustly executed throughout the entire population (Gavin-Smyth et al., 2013; Manu et al., 2009). While not all genetic processes experience the same level of canalization, necessary genetic networks that play a crucial role during development, such as embryonic patterning, would be more likely to be highly canalized given its vital role in defining key cell populations within the organism (Lott et al., 2007; Manu et al., 2009; Rünneburger and Le Rouzic, 2016).

Precision in the genetic patterning of Drosophila embryo

Genetic patterning of an embryo is essential for the development of a functional organism. It is critical that the establishment and maintenance of this pattern can be faithfully reproduced with precision to ensure a high resolution of positional information. To accomplish this, the developing embryo employs regulatory mechanisms at the transcriptional level to ensure precision is maintained. In the early *Drosophila* embryo, maternally loaded *bcd* mRNA is localized at the anterior pole to produce a protein gradient (Sauer et al., 1996). It has been shown that by balancing the amount of *bcd* mRNA within the nucleus of individual cells and the syncytial cytoplasm a stable protein gradient with low variability can be formed (Gregor et al., 2007).

Refined Bcd gradient allows for the precise expression of the core group of gap genes (Gregor et al., 2007b). The zygotically transcribed gap genes show stochastic variability in the level of transcription along the A-P axis (Little et al., 2013). Despite this, the individual nuclei manage to overcome the variability in transcription by ensuring that only a certain amount of mRNA present in the cytoplasm is used for translation through an intrinsic averaging system (Little et al., 2013). While mRNA fluctuations are the result of varying amounts of RNA polymerase, the translocation of the mRNA to the cytoplasm appears constant, suggesting that a refined and stable amount of gap gene mRNA is achieved in the cytoplasm, despite the stochastic variability

in transcription (Little et al., 2013). It has been suggested that this averaging process represents an example of an intrinsic self-organizing system that ensures stable and precise gene expression during the genetic patterning of the *Drosophila* embryo.

Precision of morphological events

While self-organization and regulation likely acts to ensure refinement of the genetic pattern, does this regulation apply to morphological events? It has been shown that growth and shape changes within the developing embryo do display some degrees of self-correcting properties that ensure homogeneity and reproducibility (Aliee et al., 2012; Hong et al., 2016; Xiong et al., 2013; Yevick et al., 2019). A thus far unresolved question is whether apparent morphogenetic precision a direct consequence of precise upstream patterning without the need of any noise correction mechanism. Or if not, how precision during morphogenesis ensured?

About this thesis

In this thesis, I set out to address three outstanding questions surrounding the CF. The first question addresses the fundamental processes that are responsible for the development of the CF, specifically, what are the cellular and mechanical mechanisms that underlie the formation of the CF? To answer this question, I had performed comprehensive and systematic multi-view imaging analysis of the CF throughout the development of *Drosophila* embryos. The second question I sought to answer revolves around what dictates the area in which the CF forms. In other words, how is the spatial precision of the CF formation achieved? This question had been addressed through examination and manipulation of the genetic circuit that patterns the region of the embryo that gives rise to the CF. The last question I attempted to answer addresses the significance of the CF, more importantly, what is the function of the CF? To address this question, I had designed strategies that would allow me to examine embryonic development in

embryos in which the CF was genetically ablated. Additionally, I had attempted to genetically create an ectopic furrow in other regions of the embryo and examine how the ectopic furrow effects embryonic development. Comprehensive and detailed methods are outlined in chapter 2, while additional methodological details are further described in individual chapters.

In Chapter 3, I will show data that demonstrates that the initiation of the CF is inherently noisy. This noise is refined through tissue-scale mechanical coupling of cells through the planar polarization of MyoII. Through this MyoII mediated mechanical coupling, the noise generated by heterogenous mechanical and cell behaviors of individual initiating cells can be refined to ensure that, despite the noise, a linear CF can still form regardless of deviation from the genetic patterning. This chapter contains the entirety of the manuscript submitted for publication which represents the combined work of my coauthors, collaborators and myself. Throughout the texts contained in this chapter, I will explicitly acknowledge the contributions of my co-authors.

In chapter 4, I sought to identify the effector genes that are downstream of the Btd and Eve genetic regulatory circuit. Using Translating Ribosome Affinity Purification (TRAP) methodology, I performed preliminary experiments that showed that the TRAP constructs can be expressed under the control of various enhancer sequences and that it may be possible purify the GFP-tagged ribosomes. This proof of concept experimentation will likely allow future endeavors to isolate CF-specific translatome.

In chapter 5, I will describe the preliminary experiments I performed to address the outstanding question of the function of the CF. Through genetic manipulation, I generated mutant backgrounds that lack a CF, and explored ways to potentially create an ectopic CF. The data presented in chapters 4 and 5 are preliminary results that have not been included in the submitted manuscript.

Chapter 6 covers possible future directions and further experimentation that can be done to further expand on the results I present in this thesis. These future directions primarily focus on the refinement of the experiments discussed in chapter 4 and 5, as well as further exploration of the intrinsic forces generated by the embryo and their potential influence on the dynamics of CF initiation. In the last chapter, chapter 7, I will present an overall summary and conclusion of this dissertation research.

Chapter 2: Methods and materials

Drosophila strains and genetics

Drosophila strains used for live imaging were *MyoII-GFP* [also known as *Sqh-GFP*, (Royou et al., 2002)], *H2Av-mCherry* (Krzic et al., 2012), *Gap43-mCherry* (Izquierdo et al., 2018), *MyoII-mKate2* (Pinheiro et al., 2017), *α-Cat-Venus* [*UASp-α-Cat-Venus* (this study) driven maternally by *matαTub-Gal4VP16*^{67C}], Eve-LlamaTag (this study) and *EGFP-STOP-bcd* (for Eve-LlamaTag imaging, (Bothma et al., 2018).

Drosophila mutant alleles used were *eve*^{R13} (FlyBase ID: FBal0003885), *runt*^{B5} (FlyBase ID: FBal0014848), and *btd*^{AX} (FlyBase ID: FBal0030657). In fixed embryos, homozygous *eve*^{R13} and hemizygous *runt*^{B5} and *btd*^{AX} mutant embryos were identified based on the lack of antibody staining of the respective gene products, or for *runt*^{B5} mutants in Figure 2E, by altered expression pattern of Eve and Btd. In live imaging experiments, the mutant embryos were identified based on the absence of a balancer-linked reporter construct. This construct expressed a nuclear localized Venus [modified from pStinger (Barolo et al., 2000)] under the control of a hb0.7 enhancer (Schröder et al., 1988) and was inserted on the FM7h (for *runt*^{B5} and *btd*^{AX}) or CyO (for *eve*^{R13}) balancer via P-element mediated transposition.

A BAC construct, *P[acman]*$^{CH322\text{-}103K22}$ (BACPAC Resources, Center at Children's Hospital Oakland Research Institute), that encompasses the entire *even-skipped* locus was used to create *even-skipped*$^{CH322\text{-}103K22}$*-mNeonGreen*, where the stop codon of *even-skipped* is replaced by an mNeonGreen insertion following a linker region (N-ter-GSAGSAAGSGEV-C-ter) 3' using a standard protocol. To generate *eve2-7* enhancer deletion constructs, stripe1 (+6.6 kb to +7.4 kb from transcription start site of *even-*

skipped locus, Fujioka et al, 1999, Dev.) and Late Element (-6.4 kb to -4.8 kb, Fujioka et al, 1996, Dev.) regions were deleted through homologous recombination

For mis-expression experiments, *UAS-eve* and *UAS-runt* (gifts from P. Gergen, Stony Brook University, USA) were driven maternally by the maternal Gal4 double driver (*matαTub-Gal4VP16^{67C}; matαTub-Gal4VP16^{15}*) and incubated at 18°C; *UAS-btd* (FlyBase ID: FBti0114911) was driven zygotically by *nos-GAL4-GCN4-bcd3'UTR* (Janody et al., 2000) and incubated at 25°C. For *α-Cat* RNAi experiments, *P{TRiP.HMS00317}^{attP2}* (Ni et al., 2011) was driven by *matαTub-Gal4VP16^{67C}; matαTub-Gal4VP16^{1}* and incubated at 18°C.

For opto-DNRho1 experiments, females of *UASp-pmGFP-CIBN; UASp-CRY2-mCherry-Rho1[N19, Y189]* (experimental) or *UASp-CRY2-mCherry-Rho1[N19, Y189]* (control) were crossed with males of *matαTub-Gal4VP16^{67C}; matαTub-Gal4VP16^{15}* double driver containing the *Gap43-mCherry* imaging marker. The resultant F1 flies were used to set up egg deposition cages that were kept at 18°C for collection of embryos used in the experiments. The fly lines containing *UASp-pmGFP-CIBN; UASp-CRY2-mCherry-Rho1[N19, Y189]* and *UASp-CRY2-mCherry-Rho1[N19, Y189]* were unpublished gifts from B. He (Dartmouth College, USA) and E. Wieschaus (Princeton University, USA).

Generation of TRAP lines (pTRAP)

The following construct were generated: 1) pBabr-hsp70-EGFP-RpL10ab: GFP tagged Rpl10ab was amplified from *UAS-GFP_RpL10ab* flies (Bloomington stock center, 42681) using primers () and () and combined with hsp70 promoter through overlap PCR using () and () primers. *Hsp70-EGFP-RpL10ab* fragment was inserted in to pCR®II-TOPO® vector and sequenced. The correct fragment was digested with SpeI and SphI restriction enzymes and inserted between the SpeI and SphI restrictions sites on pBabr, upstream of attB element. Enahcners were amplified from wild-type genomic DNA using the following primer sets: Btd (5'- GAT ACA AGC AAA GAT

AT- 3') and (5'- TCT CAA CCA ACT TGA TC -3'), Eve1 (5'- GGC CTA ATC ACT TCC CTG AAA -3') and (5'- GCC TTG GGA TAT CTG AAT ATC TGG GTA TCC AT -3'), Eve2 (5'- AAT ATA ACC CAA TAA TTT GAA GTA ACT GGC AG-3') and (5'- TCG TGG GGT CCA CCC ACA ACT ACC TGC TGC CC -3'), and Eve5 (5'- GGG CGG GTG CAT CAA ATC CTT T -3') and (5'- TGG CAG GCA AGT CAC CAC GCA CC -3') (Sackerson et al., 1999). Tandem enhancers were generated by overlap PCR using the following primers which include a 5' KpnI restriction site, and a 3' SpeI restriction site: Btd (5'- AAA GGT ACC GAT ACA AGC AAA GAT ATA CAA -3') and (5'- AAA TAG TTT TAA ATC TCA ACC AA -3'), Eve1 (5'- TTT AAA GGT ACC GGC CTA ATC ACT TCC CTG -3') and (5'- TTT AAA ACT AGT TTT AAA GCC TTG GGA TAT CTG AA -3'), Eve2 (5'- TTT AAA GGT ACC AAT ATA ACC CAA TAA TTT GAA GTA ACT GG -3') and (5'- TCG TGG GGT CCA CCC ACA ACT ACC TGC TGC CC -3'), and Eve5 (5'- TTT AAA GGT ACC GGG CGG GTG CAT CAA ATC CTT T) and (5'- TTT AAA ACT AGT TTT AAA TTA TGG CAG GCA AGT CAC C -3'). The tandem enhancers were inserted into pCR®II-TOPO® vector for sequencing. Correct tandem enhancer fragments were digested with KpnI and SpeI and inserted into the KpnI and SpeI restrictions sites of *pBabr-hsp70-EGFP-RpL10ab*. Completed plasmids were injected into w^{118}, P{CaryP}attP2 embryos (Bloomington stock center, 8622) using phiC31 system. Microinjection of constructs was performed by Rainbow Transgenic Flies, Inc. Positive flies were initially balanced over a TM3 balancer and homozygotic flies were used for experiments.

Generation of Btd misexpression lines (pMIST)

The following base construct was created by Genscript Biotech Corp.: 1*) pUC-hsp70-FRT-MCS1-SV40-FRT-MCS2-SV40*. CD4tdmGFP fragement was amplified from *pBabr-mTub-HemmnarGFP* using the following primers: (5'- CCC GGG ATT ACC CTG TTA TCC CTA ATG AAT CCC AAG AGC GA -3') and (5'- TTT AAA CGT ACG TTA GAG

GGC AAC TTC AT -3'). The CD4tdmGFP fragment digested with I-SceI and BsiWI restriction enzymes and inserted between the I-sceI and BsiWI restriction sites into MCS1 site in *pUC-hsp70-FRT-MCS1-SV40-FRT-MCS2-SV40* to generate pUC-hsp70-FRT-CD4tdmGFP-SV40-FRT-MCS2-SV40. Btd cDNA was amplified from wild-type genomic DNA with the addition to a 5' SacII and a 3' PacI restriction sequences using the following primers (5'- TTT AAA CCG CGG ATG ATC GAT GCG GCC TGC AA -3') and (5'- CCC GGG TTA ATT AAT TAC AGC TTT ATC GCC GCA -3'). The Btd cDNA was digested with SacII and PacI restriction enzymes and inserted into the MCS2 site to generate *pUC-hsp70-FRT-CD4tdmGFP-SV40-FRT-BtdcDNA-SV40*. TRAP plasmids containing the tandem enhancers for Btd, Eve1, Eve2 and Eve5 were digested with SpeI and SphI to remove the hsp70-GFP-RpL10ab fragment and replace it with the -*hsp70-FRT-CD4tdmGFP-SV40-FRT-BtdcDNA-SV40* fragment digested with SpeI and SphI. Completed plasmids were injected into w^{118}, P{CaryP}attP2 embryos (Bloomington stock center, 8622) using phiC31 system. Microinjection of constructs was performed by Rainbow Transgenic Flies, Inc. Positive flies were initially balanced over a TM3 balancer and homozygotic flies were used for experiments.

Generation of the Eve-LlamaTag line via CRISPR/Cas9 genome editing

The following constructs were generated: 1) *pBS-LlamaTag-24xPP7-3xP3-dsRed*: A DNA fragment containing Llama-tag coding sequence was amplified from pbPhi-ms2-sna-greenLlama (Bothma et al., 2018) using primers (5´-TTT CCG AAT TCG CTA GCG GAG GAG GTG GAG GTG GCA TG-3´) and (5´-GGA AAC TGC AGC TAC GAC GAG ACA GTG ACC TGA G-3´) and digested with EcoRI and PstI. The resultant fragment was inserted between EcoRI and PstI sites in pBS- 24xPP7-3xP3-dsRed (Lim et al., 2018). 2) *pBS-5´eve-LlamaTag-*

24xPP7-3´eve-3xP3-dsRed: A DNA fragment containing 5´*eve* was amplified from genomic DNA using primers (5´- TTT AAG TCG ACA ATG CCT ATC CAG TCC GGA TAA CTC-3´) and (5´-TTA AAG CTA GCC GCT TCA GTC TTG TAG GGC TTG AAG AGC TTC GGC-3´) and digested with SalI and NheI. The resultant fragment was inserted between SalI and NheI sites in pBS-LlamaTag-24xPP7-3xP3-dsRed. Subsequently, a DNA fragment containing 3´*eve* was amplified from genomic DNA using primers (5´-TTT AAT CTA GAC TGA GGC GTA AGC CCG CGA TCC ACA C-3´) and (5´-TTA AAG CGG CCG CAC ACA GCC GGG ATC AGG GGT GGC-3´) and digested with XbaI and NotI. The resultant fragment was inserted between XbaI and NotI sites in pBS-5´eve-LlamaTag-24xPP7-3xP3-dsRed. 3) *pCFD3-eve-gRNA*: Two DNA oligos (5´-GTC GCT TCA AGC CCT ACA AGA CTG-3´) and (5´-AAA CCA GTC TTG TAG GGC TTG AAG-3´) were annealed and inserted into the pCFD3-dU6:3gRNA vector (addgene # 49410) using BbsI sites. For CRISPR/Cas9 genome editing of the *eve* locus, *pCFD3-eve-gRNA* and *pBS-5´eve-LlamaTag-24xPP7-3´eve-3xP3-dsRed* were co-injected into the *nos-Cas9* embryos (Ren et al., 2013). Microinjection was performed as described (Ringrose, 2009). In brief, 0-1-hour embryos were collected and dechorionated with bleach. Aligned embryos were dried with silica gel for ~7 min and covered with FL-100-1000CS silicone oil (Shin-Etsu Silicone). Subsequently, microinjection was performed using FemtoJet 5247 (Eppendorf) with DM IL LED inverted microscope (Leica) equipped with M-152 Micromanipulator (Narishige). Injection needle was prepared with P-97 needle puller (Shutter). *3xP3-dsRed* marker was used for subsequent screening. The resulting *eve-LlamaTag-24xPP7* allele was balanced over *CyO,* from which homozygous line was subsequently obtained.

Immunofluorescence and fixed imaging

Embryos were fixed by a heat-methanol method (Müller and Wieschaus, 1996) and immunostained with mouse monoclonal anti-Neurotactin (1:20, BP106, Developmental Studies Hybridoma Bank), rabbit polyclonal anti-Eve (1:500, gift from M. Biggin, Lawrence Berkeley

National Laboratory, USA), rat polyclonal anti-Btd (1: 500, gift from E. Wieschaus), and rabbit polyclonal anti-Runt (1:100, gift from E. Wieschaus) antibodies for all experiments with fixed embryos, except Figures S4A and S4B, where embryos were fixed in 10% paraformaldehyde/1xPBS with an equal volume of heptane for 20 minutes at room temp, followed by manual devitellinization in 1xPBS on double sticky tape and immunostaining using rabbit polyclonal anti-Eve (1:500). Secondary antibodies used were Alexa 488, 568 and 647 conjugated secondary antibodies (Thermo Fisher, A-11029, A-21247, A-11036); nuclei were stained with DAPI (Thermo Fisher, P-36962) GFP detection was obtained by using a GFP-Booster (1:200) (Chromotek, gba488-10). in embryos fixed in 10% paraformaldehyde. Imaging was performed on a Leica SP8 system using a 63x oil objective [numerical aperture (N.A.) = 1.4]. For *en face* imaging on the lateral surface of the embryo, including both the 3D quantitation of Btd and Eve nuclear intensities and the whole embryo view tiled images, a deep z stack averaging 60 μm with a z step size of 0.3 μm was performed, based on the system optimized Nyquist function. For the coronal view of CF morphology, a single z slice of coronal optical section was taken. For Eve-LlamaTag versus anti-Eve quantitative imaging in paraformaldehyde fixed embryos, a z stack averaging 30 μm with a z step size of 0.3 μm was performed.

Live imaging

Light sheet microscopy imaging was performed on a MuVi-SPIM essentially as described previously (Caroti:2018bo. de Medeiros et al., 2015). Briefly, embryos were mounted in gelrite gel and imaged using a pair of 25X water immersion objectives (CFI75 Apo LWD 25XW, Nikon; N.A. = 1.1) for detection, and a pair of 10X water immersion objectives (CFI Plan Fluor 10XW; N.A. = 0.3) for illumination. For each time point, embryos were first imaged from two opposing directions and then from two directions orthogonal to the first two. Time resolution was 30 s per complete data point. The four image stacks of every time point were registered using a content-

based registration algorithm, and fused into an isotropic volume using maximum intensity values. Both, fusion and registration were performed using a MuVi-SPIM image registration and fusion pipeline that was kindly provided by Luxendo.

Two-photon time-lapse imaging was performed on an Olympus Fluoview FVMPE-RS system equipped with an InSight DeepSee pulsed IR Dual-Line laser system (Spectra Physics) using a 25X water immersion objective (N.A. = 1.05). The tunable laser line was output at 930 nm for GFP, 960 nm for Venus, while the fixed line output at 1040 nm for mCherry and mKate2. Four different general settings were used: 1) a z stack of ~150 μm depth with a z step size of 3 μm for *en face* lateral view of the whole embryo, 2) a coronal single optical section, 3) a single xz line scan of a total z depth of 70~150 μm with a z step size matching the lateral pixel size for isotropic resolution, 4) a z stack of 42 μm depth with a z step size of 1 μm for *en face* lateral view of the Eve1 region for Eve-LlamaTag and MyoII-mKate2 2-color imaging.

Single-photon confocal imaging was performed on a Leica SP8 system. 3D visualization and quantitation of MyoII distribution was performed on embryos expressing *Gap43-mCherry* and *Sqh-GFP*, or *MyoII-mKate2*, using a 20X oil immersion objective (N.A.= 0.75) with a total z depth of 28 μm and a z-step size of 1 μm or a total z depth of 29 μm and a z-step size of 0.5 μm for 3D unwrapping image processing. Quantitation of lateral *en face* MyoII intensity and polarization was performed on embryos expressing *MyoII-mKate2*, using a 63X oil immersion objective (N.A. = 1.4) with a total z depth of 9.5 μm and a z-step size of 0.5 μm.

The selection of imaging ROIs followed the definition of the “pre-CF domain” (Blankenship and Wieschaus, 2001). When viewed from the lateral side, the pre-CF domain, located approximately 30% embryo length from the anterior pole, displays a slightly more advanced cellularization front with smaller diameters of yolk stalks, as compared to the neighboring regions. The pre-CF domain can be used to predict where the CF will eventually form as early

as the mid-cellularization stage. In the *eve* and *btd* mutants, the pre-CF domain morphology is unaltered, despite the eventual loss of CF, and was used as the ROI for analysis and quantitation of MyoII dynamics and behaviors.

Laser ablation

The tunable laser line on the Olympus Fluoview FVMPE-RS system was set to 930 nm for ablation. The laser power was set at 20%, corresponding to 85 mW measured approximately 0.2 cm away from the objective (Thorlabs, PM16-121). Embryos expressing Gap43-mCherry and MyoII-GFP were used. The positioning of imaging ROIs was based on the pre-CF domain as described. For ablation experiments performed in the CF region, lateral interfaces of the initiating cells with characteristic MyoII accumulation were identified and ablated *en face* with a line of approximately 2.8 μm in length approximately 7.3±1.0 μm below embryo surface at the CF cleft formation stage. Each cut consisted of 50 consecutive iterations of line scan performed at 5x zoom with a scanning speed of 2 μs/pixel with a total duration of 60 ms. Ten frames of single z slice before the ablation and 50 frames afterward were recorded at the same z position as the ablation, all with a frame rate of 1 s/frame. Only one ablation was performed on each embryo. Control experiments were performed on separate embryos in a region 2-3 cell rows posterior to the CF at the same stage.

Optogenetics

Fly crosses, cages for egg deposition, and embryos prior to processing were kept in the dark. To prevent unwanted photoactivation, embryos were processed, staged and mounted in a dark room with the desk lamp and the brightfield light source on the stereo microscope both covered by an amber color filter. Two-photon imaging was performed on an Olympus Fluoview FVMPE-RS system as described above. Inspection and localization of the target embryos prior to the

experiments were performed with an amber color filter on the brightfield light path. For photoactivation, the tunable laser output was set to 950 nm (Guglielmi et al., 2015), and the fixed output at 1040 nm was used for assaying the recruitment efficiency and for visualization of morphology. One photoactivation cycle consisted of two illuminations of a five-slice z-stack spaced by 1 μm starting at a depth of 11 μm below the apical surface. Photoactivation was performed at 5x zoom, and imaging with the 1040 nm laser line at 3x zoom with a scanning speed of 2 μs/pixel with 2x line averaging. The laser power was set at 6%, corresponding to 12.75 mW at 950 nm measured 0.8 cm away from the objective (Thorlabs, PM16-121). No evidence of photodamage was observed when using this laser power. Between each photoactivation cycle, imaging at 1040 nm was performed to visualize the morphology and *CRY2-mCherry-Rho1[N19, Y189]* localization. Imaging at 1040 nm was always performed prior to the first photoactivation cycle in every experiment.

Two experimental designs were used: full and strip photoactivation. The positioning of imaging ROIs was based on the pre-CF domain as described. For full photoactivation the activation ROI covers the entire lateral area of the pre-CF domain, whereas for strip activation the ROI is a narrow strip that bisects the pre-CF domain. For full photoactivation, the ROI size was 76.6 x 86.4 μm, photoactivation took 28 s, and the total cycle time was 50 s. For strip photoactivation, the ROI size was 115.2 x 21.6 μm, photoactivation took 10 s, and the total cycle time was 35 s.

Purification and Western blot of GFP-tagged ribosomes

Immunopurification of GFP-tagged ribosomes was performed following a previously published protocols (Heiman et al., 2014; Kratz et al., 2014). Embryos were collected at times points described in chapter 4 and homogenized using glass pestle in ice cold extraction buffer (20mM HEPES pH7.5, 150mM KCl, 10mM MgCl2, 0.5mM DTT, 10ul/ml SuperAsin, 10ul/ml RNAse OUT, 100U/ml TubroDNAse in RNAse free water). Homogenized samples were centrifuged at 2,000G for 10 min at 4°C. Aqueous fraction was separated from the pellet, which was

resuspended in extraction buffer. 1% NP-40 and 30mM DHPC were mixed via pipetting before re-centrifugation at 20,000G for 10 min at 4°C. Protein quantification was performed using standard BSA techniques.

Immunoprecipitation of samples was performed using GFP-nanobodies coupled to magnetic beads (Chromotek, gtma-10). Beads were washed using extraction buffer prior to the addition of samples. High salt buffer (20mM HEPES, 350mM KCl, 10mMMgCl2, 1% NP-40, 0.5mM DTT, 10U/ml Turbo DNAse in RNAse free water) was added to the bead/lysate mixture and incubated overnight at 4°C, rotating. Beads were subsequentially isolated using magnetic stand and washed in high salt buffer. Samples were resuspended in high salt buffer with β-mercaptoethanol and boiled at 95°C for 15 minutes. Solution was isolated from magnetic beads and stores at -80°C.

Samples were diluted to a 1x concentration of 10ug in extraction buffer containing 1x β-mercaptoethanol and loaded into a precast 10% polyacrylamide gels (Bio-Rad, 4561033EDU) and ran at 30mAmps for 40 minutes. Gels were transferred to PVDF transfer membranes (Millipore, IPVH07850) at 4°C using 100V for one hour. PVDF membranes were blocked in a 10% milk solution (BD Biosciences, 232100) before incubation in mαGFP antibodies (1:1000 dilution in milk buffer, Sigma Aldrich, 11814460001) overnight at 4°C. Membranes were washed using a 0.1% tween20/1xPBS solution and incubated in mαHRP (1:1000 dilution in milk buffer, Invitrogen, 62-6520). Membranes were washed in 0.1% tween20/1xPBS solution. ECL detection was performed using protocol outlined in kit (Thermo Scientific, 34075). Time-lapse exposures were captured using the Fujifilm LAS-3000 imager.

Theoretical estimate of RMSE

To obtain a theoretically estimate of the RMSE under the condition that 20% of initiating cells display a 1-cell-diameter offset from the CF axis, while all others perfectly align along the CF

axis, the procedure below was followed. Let the number of cells that display anterior-offset be A, while the number of cells with posterior-offset be P. Location of the least-square-root linear fitting for all cells can be determined by minimizing the SR function below with respect to the line position X,

$$SR = \sqrt{\sum_{i=1}^{5(A+P)}(x_i - X)^2} = \sqrt{4(A+P)X^2 + P(1-X)^2 + A(1+X)^2}\,,$$

where x_i is the position of the i-th cell along the A-P axis perpendicular to the CF, with one-cell-diameter offset to the anterior at $x = -1$, while one-cell-diameter posterior offset at $x = 1$. From $\frac{d}{dX}SR = 0$, it can be solved that SR is at the minimum when $X = \frac{P-A}{5(A+P)}$. The RMSE of cells to the linear fit can thus be calculated as

$$RMSE = \sqrt{\frac{1}{5(A+P)}\sum_{i=1}^{5(A+P)}(x_i - X)^2} = \sqrt{\frac{4(A^2 + 3AP + P^2)}{25(A+P)^2}}$$

From the formula above, it can be derived that $RMSE \geq \sqrt{\frac{4}{25}} = 0.4$. Thus, the theoretical estimate of the RMSE to linear fit with 20% of cells displaying a 1-cell-diameter offset has a lower bound of 0.4 cell diameter.

3D vertex modeling

The model

To model epithelial deformation caused by spatially patterned mechanical modulation, a vertex-based model was developed to describe morphological changes of a monolayered epithelium in three dimensions (3D), following the previously described approaches (Fletcher et al., 2014; Hannezo et al., 2014; Wen et al., 2017). The 3D cell shape was represented by a hexagonal

prism with vertices and edges (Figure 6A). In a highly viscous environment, the mechanical forces generated by tissue mechanics on each cell vertex are balanced by the surrounding viscous drag, as follows:

$$-\gamma \frac{d\vec{r}_{\mathrm{i}}}{dt} - \frac{\partial U}{\partial \vec{r}_{\mathrm{i}}} = 0 \tag{1}$$

where $\vec{r}_{\mathrm{i}}$ is the position vector of the ith cell vertex, γ is a constant which measures resistance from the surroundings, and U is a potential energy function determined by the entire tissue mechanics.

The potential U, shown as Eq.(2), was constructed by considering the energy contribution from elasticity at the apical surfaces (the first term), tension at the basal and lateral surfaces (the second and the third terms), and elasticity of the cell volume (the fourth term), as follows:

$$U = \sum_{i=1}^{N} \kappa_i \left(P_i - P_{0_i}\right)^2 + \sum_{i=1}^{N} \lambda_{bi} A_{bi} + \sum_{k} \lambda_{l_k} A_{l_k} + \sum_{i=1}^{N} K_v (V_i - V_0)^2 \tag{2}$$

where P_i is the apical perimeter, A_{b_i} is the basal area, A_{l_k} is the lateral area, and V_i is the volume of the ith cell. The first, second, and fourth terms are summed over all the cells with a population size of N, and the third term runs over all the lateral surfaces. The apical elastic modulus κ_i, the preferred apical perimeter P_{o_i}, the basal tension λ_{b_i}, the lateral tension λ_{l_k}, the modulus of cell volume elasticity K_v, and the preferred cell volume V_o describe the mechanical properties of cells within the epithelium. Note that the cell geometric variables, $P_i, A_{b_i}, A_{l_k}, V_i$, are calculated from the position of cell vertices, and thus the potential U is a multivariable function of the vertex positions.

Patterning of cell mechanics

Cells within a flat epithelium were set to possess identical mechanical conditions initially, i.e., $\kappa_i, P_{o_i}, \lambda_{b_i}, \lambda_{l_k}$ were the same for all the cells. For simulation of a CF-like mechanical change, tension at the lateral membrane in a localized tissue area was increased via supplementing the potential energy U with the additional modulation energy function as follows,

$$U_{\Delta l} = \sum_{k'} \Delta\lambda_{l_{k'}} A_{l_{k'}} \tag{3}$$

where $\Delta\lambda_{l_{k'}}$ is the modulation of tension values at the k' th lateral membrane. Thus, for a given setting of cell mechanics parameters, the position of cell vertices was numerically computed according to Eq.(1) with the combined potential $U + U_{\Delta l}$, and a stable tissue morphology was achieved when $U + U_{\Delta l}$ reached a minimum.

To compare the morphological outcomes of mechanical changes distinct from a CF-like system, tissue deformation driven by two types of changes in the apical mechanics were considered. First, to simulate a VF-like apical area constriction, nonhomogeneity was introduced to the apical elasticity term according to the following formula,

$$P_{0_j} \rightarrow P_{0_j} + \Delta P_{0_j} \tag{4}$$

where ΔP_{o_j} is the change of preferred apical perimeter of the jth cell under modulation. Second, to simulate constriction of cell boundaries at the apical surfaces, tension at the apical cell boundaries was modulated by supplementing the potential U with the additional potential energy function as follows,

$$U_{\Delta a} = \sum_{j} \Delta\lambda_{a_j} e_j \tag{5}$$

where $\Delta\lambda_{a_j}$ is the modulation of tension at the jth apical cell boundaries of length e_j.

Eq.(5) allows tuning of individual apical boundaries and is used to introduce polarized apical tension for simulation of GBE-like mechanics. Overall the local modulation of cell mechanics during tissue morphogenesis was simulated by supplementing the potential U with an additional potential $U_{\Delta l}$ in Eq.(3) or $U_{\Delta a}$ in Eq.(5). The introduction of additional potential functions is equivalent to the introduction of nonhomogeneity to the cell mechanical properties, such as Eq.(4), in the potential U. The changes introduced via Eq.(3-5) allowed for a comparison of morphological changes under CF-, VF-, and GBE-like mechanics shown in Figure S7A and S7B.

Model settings for simulation of spatial and temporal noise: conditions at the tissue boundaries, spatially patterned differential tension, and noise introduction

To simulate the response of a CF-like system to noise during epithelial folding, two modifications were made to the original CF-like mechanical setting. 1) Given that deformation of epithelial tissues on the basal side is negligible during CF initiation, the positions of cell vertices on the basal surfaces were fixed, whereas the apical vertices were freely displaced by mechanical forces. 2) For simulations of spatial noise, we considered a variety of spatially-patterned lateral tension as schematized in Figure 6B, patterns (a) to (f), where the tension value remains constant during simulations. In contrast, for simulations of temporal noise, we impose a Gaussian white noise on the prototypical tension pattern (a) via the following formula,

$$\Delta\lambda_{l_{k'}} \rightarrow \Delta\lambda_{l_{k'}} \times [1 + \xi(t)] \qquad (6)$$

where the noise ξ, which has a mean of zero and a standard deviation σ, gives a random value to tension at the k' th lateral membrane at each simulation time step t.

Quantification of tissue morphology: cell alignment and tissue fold depth

To quantitatively describe the features of tissue morphology, two quantities S and D were introduced to measure the alignment of cells and the depth of tissue fold, respectively. The measurement of cell alignment is formulated as

$$S =< cos^2(\theta) >= \frac{1}{m-2}\sum_{i=1}^{m-2} cos^2(\theta_i)$$

where

$$cos(\theta_i) = \frac{(\vec{r}_i - \vec{r}_{i+1}) \cdot (\vec{r}_{i+2} - \vec{r}_{i+1})}{|\vec{r}_i - \vec{r}_{i+1}| \times |\overrightarrow{r_{i+2}} - \vec{r}_{i+1}|}$$

and $i = 1,2,\ldots,m-2$ is the index of apical vertices along the supracellular "ribbon" of interconnected lateral interfaces. $S = 1$ indicates a perfect alignment (i.e., a straight boundary), whereas $S = 0$ corresponds to a zig-zag boundary with an angle of 90 degree between two successive segments. In addition, the depth of folds was measured as the Z distance between the highest and the lowest vertices on the apical surfaces, as follows:

$$D = z_{max} - z_{min}$$

where z_{max} and z_{min} are respectively the maximum and minimum of the Z component of the apical vertices. Larger values of D indicate deeper indentation of the apical tissue surfaces.

Summary of parameter values used in the simulations

The units of energy, length, and time were chosen in such a way that allows $K_V = V_o = \gamma = 1$. The parameter values used for a representative simulation were summarized below.

Parameters	Physical Meaning	Values [a.u.]
γ	Drag constant of viscous resistance	1.0
κ	Elastic modulus of apical perimeter elasticity	0.0689
P_o	Preferred length of the apical perimeter	2.5650
λ_b	Tension of the basal surfaces	0.0477
λ_l	Tension of the lateral surfaces	0.0207
K_V	Elastic modulus of cell volume elasticity	1.0
V_o	Preferred volume of cells	1.0

Quantification and Statistical Analysis

Image processing and quantification

Images were processed, assembled into figures and converted into videos using FIJI and Adobe Illustrator. Quantitative data were analyzed and processed by Excel, Octave and custom-made Python scripts using Numpy, Pandas, and SciPy libraries. Plots were generated by custom-made Python scripts using Matplotlib and Seaborn graphic libraries.

The sections below provide brief descriptions of image processing and analysis procedures.

Live imaging time alignment

Time lapse images were aligned temporally based on the following events: the formation of CF cleft, the end of cellularization, the mitotic rounding or anaphase onset of MD2 or MD6. 1) The formation of CF cleft was defined as the first frame when a gap between the initiating cell and vitelline membrane was greater than more than 4 μm or otherwise when a continuous, persistent process of cell shortening began using the coronal views. For the *en face* imaging at the lateral surface of the embryo, the z stack images were xz resliced and projected to produce a coronal view for CF cleft visualization. 2) To estimate the timing of the end of cellularization, coronal images were first rotated so that the apical-basal axis was parallel to the y axis. To track the advancement of the basal surface during cellularization, a rectangular ROI containing the basal surface was manually selected, the pixel intensities averaged along the x axis of the ROI, and the process re-iterated to create a kymograph of the advancing basal front. The kymograph was blurred, binarized and skeletonized to produce a single pixel line that approximated the basal progression of the cellularization “frontline”. The first pixel at which the “frontline” ceased basal movement was defined as the timepoint of the end of cellularization. This procedure was typically repeated 3 to 5 times in non-overlapping regions along the basal surface. The resultant timepoints were averaged as an estimate of the timing of the end of cellularization. 3) For the estimate of mitotic rounding of MD2 or MD6, one frame prior to the formation of fully circular mitotic cell was used. For the estimate of anaphase onset of MD2 or MD6, the first frame at which the MyoII accumulation at the cleavage furrow became visible was used.

Cell tracking and analysis for in toto SPIM time-lapse data

Tracking of CF initiation was performed in three dimensional (3D) data sets using the FIJI plug-in Mamut (Wolff et al., 2018). In membrane labeled data sets (Figure 1B), CF initiation was determined in a standardized surface view of fixed depth and defined as the time point in which

the apical area of the initiating cell had collapsed to a vertical line. In nuclear labeled data sets (Figure S1A and Movie S1), CF initiation was determined in transverse planes by the basal descent of initiating cell nucleus from its average peripheral position towards the embryo center. The average nuclear position was determined over an interval of 2 minutes during blastoderm stage, initiation was defined as the time point in which the center of the nucleus has descended from this average by at least 5 μm (approximately half a nuclear length). From their time point of initiation, nuclear and membrane labeled cells were tracked back to their blastoderm position; nuclear labeled cells were additionally tracked forward until lost due to low signal-to-noise ratios. Precision of the positioning of CF furrow structure was determined by fitting a plane to the position of the descending nuclei using the *fitPlane* function of the Matlab geom3D toolbox. Left and right sides of the CF were analyzed separately and goodness of fit was assessed by RMSE of the orthogonal distances.

Cell membrane interface tortuosity analysis

Two-photon coronal time lapse images of Gap43-mCherry with a time interval of 5 s were used. Interfaces (-1), (0), (+1) and (+3) were manually segmented using the Freehand Line tool in FIJI with a time interval of 1 min. The total lengths of the interface were normalized by tissue height estimated more than 55 μm posterior to interface (0) for each timeframe. The tortuosity was computed as follows for Figure 1F:

$$\frac{Total\ length}{Euclidean\ distance\ between\ end\ points} - 1$$

Identification of the initiation types in en face imaging

Time lapse *en face* images of Gap43-mCherry and MyoII-GFP with a z depth of 3-5 μm near the surface of the embryo were max projected, pre-processed with Gaussian blur and rolling-ball background subtraction in FIJI, followed by manual annotation of the initiating events.

Representative wild-type and *runt* embryos were shown in Movie S3. Initiation was defined as the descent of cell apex. The apex was manually marked one frame before the descent to estimate the location and the timing of the event. When there was only one cell at a given D-V position that descended, the event was called type I; when two cells descended simultaneously or sequentially, type II; more than two cells, type III+ (Figures 1G, 1H and 2H).

Cell-by-cell intensity analysis of Eve and Btd in 3D

Immunofluorescent images of embryos stained with anti-Neurotactin, anti-Btd, anti-Eve and DAPI were used. Btd and Eve nuclear intensities were masked by 3D nuclear masks based on the DAPI signal generated using the Surface function in Imaris 9 (Bitplane). The nuclear intensities were rescaled and normalized in each embryo between 0 to 100%. For the Btd intensities, the minimum intensity for Btd in the image was used as 0, while for the Eve intensities, the average intensity of the anterior most 10 μm cells (where Eve is not expressed) was used as 0. For both Btd and Eve, the average intensities of the top 5% expressing cells in the image were used as the 100%. The nuclear positions were re-registered along the A-P axis using the following methods. 1) Wild-type and btd^{AX} mutants: Nuclear positions were aligned at the top Eve expressing cell of the Eve1 stripe within each transverse row of cells along the A-P axis (see Figure S2A for a schematic representation). To identify the top Eve1 cell, the D-V axis is subdivided into transverse rows of 5 μm width (y-axis bins), starting from 0 μm (phase 1) or 2.5 (phase 2) μm (Figure S2A, yellow dashed lines in panel 1 and panel 2). To reduce false positives, only cells that were identified as the top Eve1 cell in both phase 1 and 2 y-axis bins were used [(phase 1 positive) $\wedge$ (phase 2 positive), $\wedge$, the Boolean "and" operation]. To establish a unified coordinate system, the x coordinates of the top Eve1 cells were set as 0 for all cells within a y range of 5 μm centered at these top Eve1 cells. This alignment step was carried out from ventral to dorsal y-axis bins in a non-redundant manner, i.e. each cell was counted only once. 2) eve^{R13} mutants: Nuclear position was aligned to the posterior edge of the Btd

expression domain within each y-axis bin of a 10 μm width, defined as the posterior most cell that expresses above the threshold of 50% intensity. 3) *runt*^{B5} mutants: Nuclear position was aligned at the anterior edge of the Eve stripe1 within each y-axis bin of a 10 μm width, defined as the anterior most cell that expresses above the threshold of 50% intensity. For the bar graphs (Figures 2B-2E), Eve and Btd mean intensities within each 5 μm bin along the D-V axis were computed, representing the mean intensities of a single A-P row of cells. The Btd expressing profiles of the *eve*^{R13} and *runt*^{B5} mutant were matched to that of the wild-type to align the x axis of the bar graphs to represent the same A-P region of the embryo.

Identification of type I and II events, and P(0) position mapping

The same immunofluorescent images as above were used. The Neurotactin signal was pre-processed using Gaussian blur and a linear Kuwahara filter. Pre-processed images were imported into Imaris 9, visualized in 3D and coronally re-sliced using the Clipping Plane function. CF initiation cells were identified based on cell morphology using the re-sliced 2D images. The initiating cell morphology was defined as a cell with shortened cell height, compared to the tissue height, and a narrowed apical surface. Initiation types were defined based on the number of cells displaying the initiating cell behavior, with a single initiating cell defined as type I and a pair of initiating cells as type II. The morphology of the lateral interfaces further aided identification. For the type I initiating cell, both lateral interfaces appear shorter than the tissue height and straight. In contrast, between the two type II initiating cells, there exists a single lateral interface that appears to be undergoing shortening and straight, while the flanking interfaces are curved. The morphology of neighboring cells immediately adjacent to initiating cell(s) displays a “wrapping phenotype” that was characterized by an expanded apical surface, a curved interface shared with the adjacent initiating cell, and a cell height comparable to the tissue height.

For positional mapping of the initiating cells, the top Eve1 expressing cells were used to define the P(0) position (Figure S2A). To ensure all top Eve1 cells were identified, the two-phase binning strategy as described was used, followed by the Boolean operation of 'OR' [(phase 1 positive) ∨ (phase 2 positive); ∨, the Boolean "or" operation]. When a type I or type II anterior cell was a top Eve1 cell, a match to P(0) position was called.

Assay for the linearity of P(0) and CF cleft positions

The linearity of P(0) and CF cleft positions were estimated by linear regression fitting. P(0) positions were defined as the top Eve1 expressing cells [(phase 1 positive) ∧ (phase 2 positive), ∧, the Boolean "and" operation; Figure S2A]. CF cleft positions were defined as the centroid of the type I cell or the midpoint between centroids of the type II pair. For linear regression, the image was rotated in order to place the regression lines along the x-axis, and the fit was performed using the Python library Sklearn. P(0) percentage matching to the top Eve cells [(phase 1 positive) ∨ (phase 2 positive); ∨, the Boolean "or" operation] was computed in each embryo and used for scatterplot and correlation analysis.

Classification of type III+ initiation events

The type III+ initiating event was defined as an event that contains three or more initiating cells (Figures 2G, 2H and S3E). The definitions of the initiating and neighboring cells were the same as described above. The type III+ events exhibit two or more interfaces between initiating cells that appear undergoing shortening and straight, while the anterior and posterior most initiating cells share a curved interface with their neighboring cells.

Quantitation of MyoII at the lateral interface in the coronal images

Two-photon time-lapse images of MyoII-GFP with a time interval of 5 s at a coronal view were used. A rectangular box was manually drawn at interface (0) and (+4) to contain only the lateral

membrane. The cropped images were then Gaussian blurred, background-subtracted with a rolling ball, and segmented using Max Entropy thresholding algorithm in FIJI to produce a mask. The mean pixel intensity was computed from the masked MyoII raw intensity, smoothed by a rolling mean with a window length of 5, and plotted as a function of time using a Python script (Figure 3B).

Estimation of total, apical and lateral lengths of interface in coronal images

Two-photon time lapse images of MyoII-mKate2 and α-Cat-Venus at a coronal view were used. The α-Cat-Venus signal was pre-processed and segmented using K-mean cluttering algorithm (http://ij-plugins.sourceforge.net/plugins/segmentation/k-means.html) with 4 clusters, of which the top cluster was used to approximate the junctions. A rectangular box was manually drawn on the first frame of analysis at interfaces (0) and the control interface (+4 or +5) to isolate the junctional cluster, whose centroid defined the junctional position. The x coordinate of the junctional position was further used to create rectangular boxes drawn at the apical and basal edges for segmentation and identification of the apex and base using pre-processed, Otsu binarized α-Cat-Venus and MyoII-mKate2 signals, respectively. The coordinates of the junction, apex, and base were used to create the rectangular boxes drawn in the next timeframe, thus functioning as tracking ROIs that aid in the automation of time series analysis. To estimate the interface, apical and lateral lengths, y distances between apex and base, between apex and junction, and between junction and base were computed, respectively. These distances were normalized by the length of the control interface, smoothed by a rolling mean with a window length of 5, and plotted as a function of time using a Python script (Figure 3D).

Quantitative analysis for the laser ablation experiments

Time lapse *en face* images of MyoII-GFP and Gap43mCherry were used. As described above, these were single z slices taken with 1 s interval at the same z position as the one at which the

ablation was performed. To measure the recoil distance, Gap43-mCherry signals were blurred, binarized, and skeletonized, followed by identification of vertices using the Analyze Skeleton plug-in in FIJI. Two vertices that flanked the interface targeted for ablation were identified, tracked over time, and the distance between them was computed, subtracted by the distance measured at the last timeframe before ablation (pre-ablation) to represent the recoil distance, and plotted as a function of time with the pre-ablation frame designated as t0. The analysis was limited to the first 20 s after the ablation as fluctuations, recovery of MyoII accumulation, or potentially wound healing response began to appear after that. To measure MyoII intensity associated with the interface targeted for ablation, MyoII-GFP signal was used to create a global MyoII mask via Gaussian blur, rolling ball background subtraction with a radius optimized for each image series, and binarization with auto Otsu thresholding in FIJI. A second, local mask was generated by combining two drawn circles centered at the two flanking vertices with a radius of 15 pixels and a line of 30 pixel thickness connecting the two vertices. Pixels shared between the two masks were used to extract MyoII intensities from the raw 16 bit images. Masked intensities were summed to represent total MyoII intensities associated with the interface. The average of interface-associated total MyoII intensities over the 10 s duration before ablation was used to represent MyoII intensity prior to the ablation.

Experiments were curated to remove only those that showed thermal damage immediately after the ablation.

3D rendering of P(0) cells, interface (0) “ribbon”, and MyoII foci

Time lapse *en face* images of Gap43-mCherry and MyoII-GFP with a total z depth of 28 μm were used. P(0) cells were identified as either the type I or type II anterior cell, which aided in the identification of interface (0) as defined in the main text. Both Gap43-mCherry and MyoII-GFP signals were pre-processed with Gaussian blur and rolling ball background subtraction in

FIJI. To segment the “ribbon” of interconnected interfaces (0) and the P(0) cells, the pre-processed Gap43-mCherry signals were loaded into 3D Slicer for manual segmentation with user-defined thresholds using the Segment Editor tool. The resultant segments were exported as the .nrrd file format. A similar procedure was performed to segment the MyoII foci based on pre-processed MyoII-GFP signal. A Python script was created to mask the segmented MyoII foci with the segmented “ribbon” using these .nrrd files. For 3D rendering, the segmented and masked data were converted into the .vtk format for import into ParaView to generate isosurfaces using the Contour tool. The isosurfaces of the P(0) cells, the “ribbon’, the MyoII foci, and the three cross-sectional Z planes at 5, 15, and 25 μm from the embryo surface were further converted into the .stl format for final visualization using Blender (Figure 4A).

Tissue-scale MyoII intensity analysis

Time lapse *en face* images of MyoII-mKate2 with a total z depth of 28 μm were used. The MyoII-mKate2 signal was pre-processed in FIJI and segmented in 3D Slicer as described above with a low intensity threshold to generate 3D cell boundaries. The inverse of the 3D cell boundaries, representing the cytoplasmic regions, was fitted with an ellipse on each Z slice using a Python script to define the geometric center that was used to estimate the centroid of the cell position (Figure S4A, left panel). The centroids of the P(0) cells, identified based on the *en face* behavior of apical descent as described above as either the type I or type II anterior cell, were used to define A-P cell rows with the row boundaries drawn at a equidistance from the centroids the two neighboring P(0) cells (Figure S4A, central panel). Within each A-P cell row, the centroids of cells anterior and posterior to P(0) were then used to establish a “D-V axis ladder” with the space between two “rungs” used to approximate the interface between cells (Figure S4A, right panel). To quantify MyoII intensity associated with each interface, the MyoII-mKate2 signal was pre-processed using a median filter and background subtracted in FIJI, followed by segmentation in 3D Slicer with a higher intensity threshold that approximates the

MyoII foci to generate MyoII 3D masks. The 3D masks were then used to mask MyoII raw intensity at each Z slice, thereby associating the MyoII intensities to a 3D grid system of A-P cell rows, interface positions, and Z slices. The resultant intensity measurements were summed across the Z slices and either summed further across the D-V axis for the analysis of either the cumulative or time-dependent integrated intensity of each interface "ribbon" (Figures 4D and 4E), or plotted as a pair-wise comparison analysis between interfaces (-1) and (0) at each D-V position (Figure 4F).

Analysis of Eve-LlamaTag and MyoII-mKate2 in live and fixed embryos

Time lapse *en face* images of Eve-LlamaTag and MyoII-mKate2 with a total z depth of 42 μm were used. Both Eve-LlamaTag and MyoII-mKate2 signals were pre-processed in FIJI and segmented in 3D Slicer with manually adjusted thresholds to generate Eve and MyoII 3D masks. Thresholds for the Eve masks were adjusted to ensure a constant volume (1100-1200 voxels). For nuclei of which the Eve intensities were too low to be properly segmented, a mask was generated by drawing a circular disk of 37 pixels with a height of 3 pixels manually drawn at the center of the nucleus using the Paint tool of Segment Editor in 3D slicer. To index the cell positions, the "ribbon" of interconnected interfaces (0) was first identified via visual inspection of the 4D stack, followed by assigning the cell rows as position (-1), (0) and (+1) following the definition schematized in Figure S4E. To define the 2D coordinates of the Eve expressing cells, the Eve masks were projected along the z axis, followed by fitting of an ellipse in a Python script, and the geometric center of the ellipse was then used to approximate the cell center. The anterior and posterior boundaries of the interface region was next defined by linking the cell centers of a cell row with the same positional index as in Figure S4E. For example, interface (0) is flanked by the linked cell centers of cell position (0) anteriorly and cell position (+1) posteriorly. Lastly, a grid pattern was established following a similar approach as the "D-V axis ladder" system described above, thereby associating the MyoII intensities to a 3D grid system of

A-P cell rows, interface positions, and Z slices. For the correlation analyses in Figures 4G-I, the position-dependent Eve intensities in Figure S4F, and the cumulative Myo intensities over time Figure S4G, a custom Python script was developed for data processing and plotting. For comparison of Eve-LlamaTag and anti-Eve immunofluorescent intensities (Figure S4C and S4D), DAPI signal was processed through the Gaussian filter, rolling ball background subtraction, manual and Otsu thresholding, and Distance Transform Watershed 3D plug-ins in FIJI to generate a 3D nuclear mask. This was then used to mask the Eve-LlamaTag and anti-Eve intensities within an ROI of 35 x 46 μm centered on the Eve1. The 3D concentration in each cell was further normalized to the min and max intensities within this ROI, defined as the mean intensities of the bottom and top 5% percentiles, respectively, within each embryo.

Comparison of CF and GB MyoII intensity and polarization

Time lapse *en face* images of MyoII-mKate2 with a total z depth of 9.5 μm near the apical surface and a frame interval of approximately 20 s were used. The CF and GB regions were manually selected as rectangular ROIs. For each time frame, a FIJI macro was used to sum project the Z stack, pre-process with Gaussian blur and rolling ball back subtraction, segment using auto local Otsu thresholding, skeletonize, followed by severing the skeleton at the junctions using Analyze Skeleton tool. Each severed skeleton object was used to measure the angle of its major axis using the FeretAngle tool. The severed skeleton was further dilated to produce a 2-pixel width mask that was then used to mask sum projected MyoII raw intensity. For each ROI (CF and GBE), MyoII pixel intensity (M) was normalized using the standard score formula: $\frac{M-\bar{M}_{global}}{\sigma_{global}}$, where the global mean ($\bar{M}_{global}$) and global standard deviation (σ_{global}) were computed from the uncropped MyoII sum projections. For MyoII polarization, the total intensities of D-V polarized MyoII (the MyoII foci that are within 45° of a vertical line) and those of A-P polarized MyoII (the MyoII foci that are within 45° of a horizontal line) were each averaged

among embryo samples. The ratio between the mean intensities of D-V and A-P polarized MyoII was then computed as a single value index for MyoII planar polarization. For both mean pixel intensities and polarization, the values were binned and averaged every minute. A second degree polynomial was fitted to the MyoII polarization plot as the trendline using a Python script (Figures 4B).

Straightening and angle analysis of the interconnected interface "ribbons"

Time lapse *en face* images of Gap43-mCherry with a z depth of approximately 6 μm near the apical surface were sum projected and pre-processed with Gaussian blur and a linear Kuwahara filter in FIJI (Figures 3G and S4B). Skeletonized images were generated from filtered membrane images using a custom-made MATLAB (Mathworks) software called FiFA (Takeda et al., 2018). Target interfaces were manually identified by examining the time series and looking for interfaces involved in CF initiation, additionally an interface approximately two to four cells anterior to the target interface was used as a control (Figures 4C). For embryos that lack CF, the pre-CF domain described above was used to identify the presumptive CF region (Figure S4B). For quantitation of angles formed by the interconnected interfaces, a single z slice of Gap43-mCherry image was pre-processed, segmented and binarized, followed by visual inspection and manual identification of the initiating cells based on their descent from the surface as described above. The interconnected interface (0) was then identified following the definition established in Figures 1E and 2I. To compute the angles formed by two interconnected interfaces, the coordinates of the shared vertex and the two flanking vertices were isolated using the Analyze Skeleton and Ultimate Points plug-ins in FIJI, followed by computing the obtuse angle centered on the shared vertex using a Python script.

Unwrapping and 3D tortuosity analysis

The surface of the *Drosophila* embryo is highly curved along the D-V axis. To analyze interface (0) geometry across a greater D-V span, the z stack images were "unwrapped" to create a stack of 2D representations of pixel intensities (called the "z′ stack" hereafter) located at the same apical-basal depths from the embryo surface. Such "unwrapping" required a reference geometry approximating the curvature. To create the reference geometry, the original 3D image stack was binarized to identify the outer contour of the embryo. To generate a smooth, curved surface that approximates the outer contour, coordinates at the surface of the binarized 3D image were sampled using a grid size of 100x100 pixels and interpolated using cubic splines with the multi-dimensional interpolation function in Octave. The resultant 3D surface was then used as the reference surface contour (z'_{ref}, orange surface in Figure S6A). To "unwrap", pixel intensity values located at the same distance along the normal directions from z'_{ref} were projected on to a 2D surface (e.g. z' = 4 μm, Figure S6A). This was performed in steps of 2 μm to generate the "z′ stack". The resultant "z′ stack" was used for inspection, manual selection of initiating cells, and 2D segmentation. For each pixel in the "z′ stack", coordinate transformation could be performed for conversion back to the original z stack coordinate system so that the actual geometry could be computed

To perform 3D tortuosity analysis, the type I or type II anterior cells were manually selected using the "z′ stack" as described, allowing for the identification of interface (0) following the definition established in the main text. To approximate the shortest distance between the two end points of the interconnected interfaces (0) on the curved surface of the "z′ slice" ("reference arc", Figure S6C), the steps described below were followed. Starting with the straight line discretized by a single segment connecting these two end points ("initial arc", Figure S6C), the segment was first discretized into two segments connected by a new point located in the center of it. The coordinate of the new point was recalculated to be the closest pixel on the reference

surface. This procedure was iterated as illustrated in Figures S6C and S6D until the arc length plateaued, producing the reference arc. The 3D tortuosity was then computed as follows:

$$\frac{Total\ interface\ length}{Reference\ arc\ length} - 1$$

where the total interface length was estimated by the sum of Euclidian distances between two adjacent points on the interconnected interface (0) based on the 3D coordinates of the original z stack.

To compare MyoII intensities between wild-type and *α-Cat* RNAi embryos, coordinates of the skeletonized interfaces in the "z′ stack" were transformed into coordinates according to the original z stack geometry. The resultant pixels representing the interfaces in 3D were then extruded 2 μm towards the surface along the normal direction of the reference geometry. To generate the final mask, we further dilated four times along the x-y plane. An identical procedure was followed to obtain a control "ribbon", 3-4 cell rows anterior to interface (0). The highest pixel intensity present in the mask of control "ribbon" was used as the cut off for computing the percentage of "positive" pixels at the "ribbon" of interface (0), and the resultant percentages were compared between wild-type and *α-Cat* RNAi embryos.

Analysis and quantitation for the optogenetic experiments

To characterize the efficiency of CRY2-mCherry-DNRho1 recruitment, which is localized in the cytoplasm in absence of activating light due to the Y189 mutation in the C-terminal CAAX membrane localization signal, four 24 μm x 24 μm ROIs were selected, two inside and two outside of the photoactivated area (Figure 6A). Membranes were segmented and intensity over

time was measured. An average of the intensities was computed for each of the four ROIs, and then an average of the two ROIs inside and outside was obtained. The normalized intensity for each timepoint was computed as $\langle I_{inside} \rangle / \langle I_{outside} \rangle - 1$. Since 1040 nm excites both CRY2-mCherry-DNRho1 and Gap43-mCherry, any increase in this normalized value should reflect changes in CRY2-mCherry-DNRho1 recruitment while accounting for photobleaching.

For full photoactivation experiments, line scans were used to give coronal sections and reveal if and when the CF cleft forms (Figures 6B and 6C). To allow comparison between experimental and control embryos, t = 0 was set as the time of MD2 formation. CF cleft formation was defined at the frame when the CF cleft depth was greater than 4 μm. CF cleft depth was defined as the distance between the top of the initiating cell and the vitelline membrane (Figures 6D and 6E).

For strip photoactivation experiments (Figures 6F and 6G), maximum intensity projections from z stacks covering 5 μm were used to visualize the morphology across the photoactivated area. For each embryo, the time at which at least one cell at each position along the DV axis outside the ROI has descended below the imaging plane was determined and subtracted from the time at which the same condition was met inside the ROI to give the “time gap” (Figure 6H). Cells that have moved outside of the ROI during the activation period, and therefore will not have been activated after moving out, are not considered. For quantitation of angles formed by the interconnected interfaces (Figure 6I), handpicked segmented cells (Figures 6F and 6G, top left panels) undergoing initiation were used to identify the interconnected interfaces (0) one timeframe prior to the first cells descend below the first imaging z slice, followed by the procedure described above .

To examine furrow linearity, the deviation from 360˚ was determined to quantify the alignment between the dorsal and ventral furrow structures before they connect across the activation ROI. The deviation from 360˚ was measured at the time when at least one cell at each position along

the DV axis outside the ROI has descended below the imaging plane, as per the above explanation. The segmented line tool in ImageJ was used to manually define the position and angle of each furrow structure with connected straight lines (Figures 6F and 6G, top center panels). The obtuse angles formed between these furrow lines and the connecting line were measured, summed, and subtracted from 360˚ to give the deviation from 360˚. This calculation was performed 3 times for each embryo, and an average was calculated. The greater the deviation from 360˚, the greater the deviation from perfect straight alignment of the two furrow structures.

Embryos were only removed from the analysis when they were mounted at the wrong angle, meaning that alignment could not be assessed.

Statistical Analyses

Welch's t-tests for two independent samples with unequal variance, and the calculation of Spearman rank-order correlation coefficient, RMSE and coefficients of variation were implemented in Python scripts using SciPy and Sklearn libraries.

Chapter 3: Spatial patterning and refinement of morphogenetic noise during CF formation during Drosophila embryogenesis

Introduction

Tissue morphogenesis is a fundamental developmental process. The complex structures that form during morphogenesis must be precise and reproducible as they contribute to body parts or are otherwise vital for development. Although stereotypical and robust morphogenesis is a common feature during development, the mechanisms by which morphological constancy is attained remain poorly understood. Morphogenetic processes typically involve two modules of information processing: 1) acquisition and maintenance of gene expression patterns, and 2) interpretation of such patterns to reprogram cell shape and function. Recent work suggests that the transcriptional regulation of developmental gene expression is precise (Bentovim et al., 2017; Lagha et al., 2012), while processes of growth and shape changes associated with morphological remodeling have been shown to exhibit self-correcting properties that promote homogeneity and reproducibility in a variety of developmental contexts (Aliee et al., 2012; Hong et al., 2016; Xiong et al., 2013; Yevick et al., 2019). However, it remains unclear to what extent morphological precision stems from the apparent spatial information encoded in the gene regulatory network and the fidelity of the mechanical decoding downstream of such positional information.

The contents of this chapter have been submitted for publication under the title “Tissue-scale mechanical coupling reduces morphogenetic noise to ensure precision during epithelial folding”. This manuscript, of which I am one of the three equal contributing first authors, is the result of a collaboration that spans three laboratories, my lab, Dr. Steffen Lemke’s lab at University of

Heidelberg, and Dr. Tatsuo Shibata's lab at RIKEN BDR. Throughout this chapter, I will explicitly distinguish work that I performed for this manuscript from contributions made by my co-authors. Data that were contributed by my co-authors will be presented separately in the supplemental figures that follow the section of the main figures.

CF initiation is temporally and spatially heterogeneous

Despite being one of the first prominent epithelial folds that marks the transition of the cellular blastoderm into gastrulation, little research has been performed on the CF. To understand the cell dynamics and the morphological process that give rise to this structure, with the assistance of Dr. Wang, I used a multi-view live imaging approach to systematically characterize the initiation behaviors that give rise to the CF. To better understand the timing and location of the cephalic furrow initiation, I established a rough timeline of events from the onset of gastrulation to the internalization of the posterior midgut and pole cells (Figure 2A).

This timeline was based on the appearance of gross morphological events such as the formation of the ventral furrow and the extension of the germband and internalization of the posterior midgut. This allowed me to define three stages of CF formation. 1) Initiation: CF formation begins with the shortening of initiating cells (see below for definition). The first morphological sign of initiation is an indentation that forms at the embryonic surface, the "CF cleft" (Spencer et al., 2015; Vincent et al., 1997), which becomes visible concurrently with ventral furrow (VF) initiation. Although the end of cellularization, when the lateral membrane finishes extending basally to form the columnar epithelial layer, is traditionally used to define the onset of gastrulation, CF cleft formation occurs several minutes before the complete cellularization of the epithelial layer. 2) Basal expansion: After the initial cell shortening during the initiation, the basal surface of the epithelial layer begins to bulge into the internal yolk space of the embryo. By relaxing the basal surface, the shortening initiating cell invaginates

and quickly leads to the rapid increase in the depth of the furrow. The basal expansion of the CF initiating cells also coincides with the onset of germband extension (GBE). 3) Cell division: The depth of the CF invagination is further increased by synchronized local cell division of the 14th mitotic cycle, the mitotic domains (MDs; Foe, 1989). MDs are spatially and temporally stereotypical, always occurring in the same order and in the same location across all embryos, providing fixed time points for comparative analysis between multiple embryos (Foe, 1989). MD2 occurs partially within the furrow, 3 to 5 cells anterior to the initiating cells, while MD6 occurs in the region immediately posterior to the CF (Figure 2A). MD2 and MD6 form approximately 10~15 minutes after CF cleft formation. By having a defined timeline, I was able to explore the spatial and temporal dynamics of CF initiation and address the questions of how the CF is specified precisely along the A-P axis, and how a linear CF structure is formed along the dorsal-ventral (D-V) axis .

To monitor the spatial pattern and temporal dynamics of CF initiation at the embryo scale, Dr. Lucas Schütz in the Lemke lab, performed *in toto* imaging of the entire embryo using selective plane illumination microscopy (SPIM). Our collaborators found that CF initiation begins in the lateral region before spreading dorsally and ventrally, demonstrating the presence of a global pattern of initiation along the D-V axis (Figure S1A). Focusing locally on the lateral most cells of the epithelial layer, they observed heterogeneities in initiation timing on the scale of 3 to 5 minutes, in addition to localized spatial heterogeneity. When our collaborators compared both the left and right side of the embryo, they observed bilateral differences in the timing and spatial distribution of initiation (Figure S1A and S1B). Despite the spatial and temporal heterogeneity of the initiating events, our collaborators showed that the nuclei of the initiating events display a near perfect linear fit a single 3d plane. Additionally, when they examined the root mean square error (RMSE) after the linear regression analysis, which measures the deviation of the initiating nuclei from a planar fit, they saw that throughout initiation, the

initiating events maintain a linear fit and show less than half a cell diameter deviation (Figure S1C and S1D; Movie S1).

From our collaborator's SPIM data, I can conclude that the initiation of the cephalic furrow is not a uniform process. But, despite the localized heterogeneity of initiating events during CF development, throughout the process of initiation, the initiation cells remain linearly aligned, illustrating that the spatial alignment of initiation events is continuously precise (Figure S1C and S1D; Movie S1) This raises the question of how a linear furrow structure can form without uniform initiating behaviors. Since the tissue/embryo scale development of the CF is linear, I sought to determine how the individual initiating cells behave.

Differential interface shortening manifests as two morphologically distinct cell shape changes

The behavior of initiating cells has previously been examined. It is known that lateral membranes of individual initiating cells decrease in length relative to their neighbors (Spencer et al., 2015; Vincent et al., 1997), and 2D optical sectioning of fixed embryos suggests that a single cell undergoes this shortening process (Vincent et al., 1997). To further understand how initiating cells behave during cephalic furrow initiation, our research team conducted a systematic multi-scale characterization of the initiating cells to determine how they can possess spatial and temporal heterogeneity, yet form a uniform cephalic furrow.

Initial two-photon live imaging I performed, that was later expanded on by Dr. Claire Bromley, showed two quantitatively distinct types of initiating events. In "type I initiating events" (Figure 2B, movie S2 top), a single shortening cell undergoes initiation, corresponding to the originally described "initiator cell" (Vincent et al., 1997). In contrast, in "type II initiating events" (Figure 2B, movie S2, bottom), a pair of cells shorten simultaneously with a shared straight interface. The cell shape of this initiating pair displays varying degrees of mirror-image symmetry across

the shared interface depending on the extent of synchronicity (Figure 2C). In both events, neighboring cells maintain a broad apical dome and form contacts with each other during shortening.

I devised a common index system for the lateral interfaces of the initiating and neighboring cells based on shared gene expression coordinates (Figure 2B; see the section below). Dr. Bromley measured lateral interface length to quantify shortening and tortuosity over time (Figure2D). For type I initiation, together with Dr. Bromley, we found that interfaces (0) and (-1) shorten nearly simultaneously and remain relatively straight throughout, suggesting comparable active contraction. Between the two posterior neighboring cells, interface (+1) shortens far less, but becomes curvy, suggestive of low contraction, but an increased strain due likely to external loads. In contrast, during type II initiation, the shortening of interface (0) precedes that of interface (-1), while interface (-1) becomes curvy similar to interface (+1). This suggests that interface (0), which is shared between the initiating cell pair, has higher contractility than interfaces shared between the initiating and neighboring cells [(-1) and (+1)]. These data indicate that the lateral interfaces undergo differential contraction. The quantitative differences between interface (0) and (-1) can distinguish initiation types.

To determine if these cell behaviors display some spatial preference along the lateral surface of the embryo, Dr. Wang and I analyzed the frequency and spatial distribution of both initiating behaviors. Focusing on the lateral most initiating cells, we found that both initiating behaviors can be identified in a given embryo, with varying frequency amongst multiple embryos. During both fixed and live imaging, we noticed that there was no obvious pattern in terms of the location of the initiating events along the D-V axis. Dr. Wang and I analyzed the frequency of initiating behaviors along the dorsal ventral axis. From examining the spatial location of the initiating events, we found that the location of both initiation behaviors is variable along the D-V

axis, indicating no set pattern that favors one initiation behavior over the other (Figure 2E and 2F).

From the analysis, I have shown that the behavior of initiating cells during CF initiation are not as uniform as previously expected and has an unappreciated degree of complexity. CF formation involves two distinct cell behaviors, in contrast to a single behavior reported previously (Spencer et al., 2015; Vincent et al., 1997). Our analysis shows that at the cellular level the lateral interfaces display quantitively heterogeneous characteristics of differential membrane shortening. Given the heterogeneities, it can be inferred that the number of a specific initiating behaviors or the location of these behaviors does not have an impact on CF formation. This suggests that within the intact epithelial tissue two initiation behaviors coexist in the presumptive CF region, and despite such heterogeneities the CF remains linear.

The CF genetic network generates positional information with single-cell row resolution, which restricts the number of initiating cells

From the previous experiments, I have shown that CF formation is more complex than originally thought. In addition to spatial and temporal heterogeneity of the initiating events, the initiating cells themselves display two distinct cell behaviors. The presence of these two behaviors raises the question as to what is causing their different behaviors. The differential cell behaviors seen during CF initiation could be caused by fluctuations or misinterpretation of the genetic patterning of the embryo. Since the CF has been shown to be a direct readout for positional patterning (Driever and Nüsslein-Volhard, 1988a, 1988b), I revisited the known genetic network that controls CF to determine how important the spatial patterning is in both defining the location of the CF initiation events and its possible role in the two differential cell behaviors. By the onset of CF formation, Btd is expressed in a single domain in the head region, while Eve is expressed in a pattern of seven transverse stripes along the A-P axis of

the embryo (Figure3A). The presumptive CF area corresponds to the overlapping expression of Btd and the first stripe of Eve (Eve1) (Vincent et al., 1997) (Figure3B). It is possible that the co-expression of Btd/Eve could be causing the two different behaviors.

To find out how this expression pattern correlates with initiation, I examined the expression of Btd and Eve in fixed wild-type embryos. Using a 3D mask generated by DAPI expression, I was able to extract the nuclear concentration of both Btd and Eve. With the assistance of Dr. Michiko Takeda, I estimated the average nuclear concentration of Btd and Eve for each D-V row of cells by aligning the data to the position of the highest Eve expressing cell of the Eve1 stripe, which we have called position P(0) (Figure4A). Analysis shows that there is a quantitatively discrete combination of Btd and Eve nuclear concentrations in each D-V cell row (Figure4B). This suggests that CF specification is associated with a quantitative “Btd/Eve positional code” that has single-cell row resolution, consistent with previously published results (Dubuis et al., 2013).

To test whether CF initiation is governed by the Btd/Eve positional code, I examined the spatial expression of Btd an Eve. Quantitative analysis of the Eve spatial pattern in *btd* mutants confirms that Btd promotes expression of Eve1 (Figure3C and 4C); (Vincent et al., 1997). Unexpectedly, the Btd pattern expands posteriorly in *eve* mutants, while overexpression of Eve inhibits Btd expression and causes loss of the CF (Figure 3D, 3F, 4C, and 4D). This suggests that Eve represses Btd to restrict its expression domain posteriorly. In addition to examining Btd and Eve expression, I investigated the role of Runt, a pair-rule transcriptional repressor that is expressed posterior to Eve1. In *runt* mutants, the domains of Eve1 and Btd expression expand, while Runt overexpression decreases Eve1 and Btd expression, and prevents CF formation (Figure 3E, 3F, and 4C-E). Data from these experiments confirms that Runt restricts the posterior boundary of Eve1 (Vavra and Carroll, 1989; Vincent et al., 1997) in addition to Btd. This data suggests a genetic network in which

Btd and Eve1 form a negative feedback loop to restrict their overlap, while Runt represses both Btd and Eve1 to further refine it (Figure 4F).

This network analysis enabled me to identify two ways to genetically broaden the width of the Btd/Eve overlap, which I employed to “blur” the resolution of the Btd/Eve positional code. Specifically, I engineered an expansion of Btd expression either directly by ectopically expressing Btd in the anterior 40% of the embryo (the Btd/Eve overlap corresponds to 33% EL; Figure 4D and 12A and B), or indirectly by removing Runt using the *runt* mutant (Figures 3E, 4C and 4E). In both cases, I observed the occurrence of “type III+” initiation events in which three or more cells undergo shortening simultaneously (Figures 3G and 4G; Movie S4, *runt* mutant) and an increase in the total number of initiating cells per unit area (Figure 3H; Movie S3, *runt* mutant).

Through these experiments, I found that spatial patterning of the CF is not as simple as initially thought. The overlapping expression of Btd and Eve1 is spatially restricted not only through the feedback circuit between these two, but also through the expression of Runt, which acts to restrict the posterior expression domain of both Btd and Eve, ensuring that initiation occurs in a single or a pair of initiating cells. Thus, the restriction of initiating events is important for proper CF formation. “Blurring” of the positional information that increase the number of cells in which the expression of Btd and Eve overlap leads to an increase in the number of initiating cells. It is currently impossible to determine if the increased number of initiating cells has a negative effect on embryonic development, however, since both of the methods used cause alterations of genetic patterning other than the CF specification *per se*.

CF initiation behaviors obey the Btd/Eve positional code with 80% precision

Now that I have established that precise spatial patterning is required for proper cephalic furrow formation, I wanted to determine how this spatial pattern correlates with the cell behaviors I have noticed during cephalic furrow development.

To determine if the positional information is sufficient to account for the specification of initiating cells, I manually identified Type I and Type II behaviors based on 3D reconstructions of the lateral surface of fixed embryos (Figures 4A and 4B). Identification of cell behavior types was made based on the morphology of the cell, independent of the expression of Btd and Eve. With the assistance of Dr. Takeda, the location of the initiating cells was mapped back to the coordinates of the expression pattern of Eve. When the location of the initiating events was compared to the positional information, I noticed that 75.3% of Type I initiating cells and 93.8% of Type II anterior cells matched the P(0) position (Figure 3I). Combined, this data demonstrates that the positional information generated by the genetic pattern accounts for the spatial positioning of 80.1% of the total initiation events. This data shows that while approximately 80% of initiating cells follow the positional information, there remains a 20% spatial inaccuracy in the specification of cephalic furrow initiation events.

This analysis reveals a previously overlooked 20% spatial inaccuracy in the specification of CF initiation. Dr. Takeda and I asked whether this inaccuracy could be due to fluctuations in Btd/Eve expression. Indeed, we observed Btd/Eve fluctuations in some mis-specified cells: for example, Btd expression in the P(-1) initiating cells is comparable to that in the P(0) initiating cells, but lower than that in the non-initiating P(-1) cells (Figure 3J). While these analyses reveal the existence of genetic noise, there were mis-specified cells that altogether lack the proper Btd/Eve positional code. For example, the P(+1) initiating cells express lower Eve and

Btd than the P(0) initiating cells (Figure 3J), indicating that the genetic noise alone does not account for all CF mis-specification. This interpretation is supported by the analysis of *runt* mutant embryos, where a near 19-fold increase of low Eve expressing cells being mis-specified as the initiating cells (Figure 3K).

From the analysis of the correlation between initiating events and the positional information, I have shown, with the help of Dr. Takeda, that the initiating cells display only 80% match to the positional information for the Btd and Eve expression pattern. But analysis of the Btd and Eve expression within initiating cells reveals genetic noise contributes only partially to the 20% mismatch. This data suggests: 1) fluctuations in the interpretation of the genetic positional information can account for some mis-specified initiating cells: 2) When more cells undergo initiation, the rate of mis-expression increases, suggesting a potential mechanical influence from the interconnected cells contributes to the misspecification.

The initiating cells linearly align among themselves, irrespective of deviation from the CF positional code

From the data presented thus far, I have shown that the initiation of cephalic furrow formation is very noisy and heterogeneous, contrary to our accepted understanding that cells respond faithfully and stereotypically to positional information. Despite the noise during the initial formation of the cephalic furrow, a uniform and linear structure is faithfully formed and maintained throughout cephalic furrow formation (Figure S1C). These data raise the question of how global and spatial alignment of the cephalic furrow is achieved despite the inaccuracies and noise seen during initiation. To address this question, I sought to investigate the spatial precision of both the Btd/Eve positional code and the initiating events, by analyzing the P(0) and CF cleft positions, respectively.

To address how spatial alignment of the cephalic furrow is achieved, I examined the spatial precision of the positional information, indicated by P(0), and the CF cleft positions. With the assistance of Dr. Takeda, I found that both the P(0) cells and the CF cleft cells both fit well to a linear alignment. The error in cleft alignment was generally lower than the theoretical lower bound of 0.4 cell diameter estimation based on the 20% mis-specification rate (Figure 3L; see Methods for the estimate, which was formulated by Dr. Fu-Lai Wen in the Shibata lab), consistent with the linearly aligned CF initiation observed in the SPIM analysis (Figure S1C).

This indicates that both the P(0) cells and the CF cleft cells are linearly aligned amongst themselves. But when we performed the same analysis and examined the deviation of the CF cleft cells from the P(0) cells, we found that there was a higher level of deviation; suggesting that the presence of mis-specified initiating events cause a greater offset between the two alignments. In support of this, and the RMSE error between CF cleft positions to the P(0) linear fit negatively correlates with the percentage match to P(0) position (Figures 2L and 2M). The RMSE of cleft alignment also negatively correlates with the P(0) percentage match, but to a much lesser degree. Thus, the initiating cell alignment can overcome imprecise specification of initiation to ensure furrow linearity.

The data suggest that the alignment of the initiating cells themselves overcomes the noise generated by the heterogeneity of the initiating cell behaviors to ensure linearity. Given that the genetic noise only contributes partially to the mis-specified initiation behaviors, it is possible that mis-specified initiation events could be the result of differential cellular mechanics.

Interface shortening is associated with lateral myosin contractility

Next, I sought to examine the possibility that the cellular mechanics contribute to noisy initiation behavior. To explore the mechanics of these initiating cells, I examined a key protein responsible for epithelial cell shape change, known as non-muscle myosin II (MyoII). MyoII has been linked to various epithelial cell shape changes, primarily by contracting the cell cortex (Heer and Martin, 2017; Munjal and Lecuit, 2014). Given its role in driving cell shape change, I looked at the dynamics of myosin during the initial cell shape changes and invagination of CF initiation cells.

To investigate CF mechanics, Dr. Bromley and I imaged MyoII and found that it is dynamically enriched as discrete foci along the lateral membrane in both type I and II events (Figure 5A; Movie S2). These foci are most frequently associated with interface (0), and their intensities fluctuate as a function of time (Figures 5B). During interface shortening, MyoII foci are often seen at adherens junctions, but can also be found in the membrane regions basal to the junctions (Figure 5C). To better understand how MyoII foci contract interface (0), Dr. Wang quantified the changes of apical (from apex to junction) and lateral (from junction to the base) lengths and found that the lateral lengths decrease, whereas the apical lengths increase, suggesting that MyoII primarily contracts the lateral surface basal to the junctions (Figure 5D).

To estimate MyoII dependent forces during CF initiation, Dr. Antonio Bolea Albero performed laser ablation experiments *en face* at the lateral interface of the initiating cells (Figures S2A and S2B). He observed a small, but discernible recoil after ablation, and the recoil distance correlates with pre-ablation MyoII intensity (Figures S2A-D), indicating that MyoII foci confer contractile forces to the lateral interface. During interface shortening, we observed a slight up shift of the basal surface (Figure 5A; Movie S2). Given that lateral MyoII contractility may not

be directional, strong resistance provided by the basal MyoII meshwork likely acts as an anchor (Dawes-Hoang et al., 2005) to direct lateral contraction towards the basal side.

Lateral MyoII enrichment is planar polarized and appears to straighten the supracellular 3D “ribbons” of interconnected interfaces

When I examined MyoII behavior earlier at the cellular scale, I saw that myosin accumulates in foci along the lateral membrane of the initiating cells. Since myosin behavior of individual cells can lead to changes at the tissue-scale, as seen during GBE (Bertet et al., 2004; Zallen and Wieschaus, 2004), I wanted to see how the lateral accumulation of MyoII is influencing tissue-scale cell dynamics.

From previous experiments I have seen that, while MyoII displays heterogeneous cellular behaviors, MyoII is generally enriched at Interface(0) (Figure 5A and 5B). I wanted to examine how the accumulation of MyoII at the interface(0) of initiating cells is distributed along interconnected interfaces that span the D-V axis. To visualize the distribution of MyoII, Dr. Bolea Albero and Dr. Takeda generated a 3D reconstruction of cell membranes of the interconnected interface(0), which was termed the “ribbon”. Along this “ribbon”, they noticed that MyoII foci are enriched primarily at the apical-lateral areas and more sporadic in the basal-lateral regions (Figure S3A). This distribution is consistent with the 2D coronal image analysis that Dr. Bromley and I performed earlier (Figures 5A and 5C; Movie S2). When they examined the distribution of MyoII along the D-V axis, they found that the distribution was not uniform. This suggests that the temporal heterogeneity seen during the shortening of initiating cells (Figure S1A) could be the result of this non-uniform MyoII distribution along interface(0).

On a tissue-scale, when I examined MyoII dynamics, I saw that MyoII is preferentially enriched along the A-P boundaries of the cells (Figure 6A, Movie S3, wild-type). This

enrichment leads to the planar polarization of MyoII, which coincides with the straightening of the apical side of the “ribbon”. This suggests that lateral contractility at the individual Interface(0) of initiating cells integrates into supracellular forces that align the Interface(0) along the D-V axis (Figure 6B, cyan line).

To analyze the tissue-scale spatial pattern of forces, Dr. Takeda plotted the cumulative total MyoII intensities along each “ribbon” of interconnected interfaces as a function of time (Figure S3B). She observed that the “ribbon” of interfaces (0) often accumulates more MyoII than other interfaces (Figure S3B-D and S4H-I), consistent with the 2D coronal data (Figure 5A) and supporting the findings of differential interface contractility (Figure 2D). There is, however, embryo-to-embryo variability, and in particular at the “ribbon” of interfaces (-1), MyoII could be as high as, or sometimes higher than that at the “ribbon” of interfaces (0). Such embryo-to-embryo variability is even more pronounced when MyoII accumulation is analyzed over time (Figure S3C and D).

From these experiments, I have shown, despite the heterogeneity of MyoII activity seen on the cellular-scale, at the tissue-scale, MyoII planar polarization appears to assist in the straightening of interface (0), which may allow for the organized invagination of CF initiation cells. This interface straightening suggests that the observed planar polarization of MyoII function as a tissue-scale mechanism to ensure ordered alignment of the initiating cells.

MyoII variabilities do not scale with patterning noise

Even though I have observed enrichment and planar polarization of MyoII along interface(0), MyoII accumulation was still very heterogeneous (Figure S3C and D). Somehow, despite the heterogeneous enrichment of MyoII, the embryo still forms a linear CF. It is possible that the heterogeneity in MyoII accumulation I have seen at the tissue-scale could be due to potential

noise that is inherent in the spatial patterning. To examine if the variability of MyoII behavior is due to the noise generated by the genetic pattern, Dr. Takeda sought to explore MyoII intensity pattern in individual cells along the D-V axis by focusing on the comparison between interfaces (-1) and (0) (Figure S3E).

For the majority of D-V positions and timepoints, interface (0) has higher MyoII intensity than interface (-1). Interestingly, the highest MyoII interface intensity is more changeable between the two interfaces in type I initiating events (Figure S3E). These observations provide molecular support for the proposed model that differential interface shortening distinguishes type I from type II behaviors (Figure 2D). Despite these spatial patterns, the cell-to-cell variability is high. Additionally, the fluctuations of MyoII intensity are often asynchronous along the D-V axis (Figure S3E). This suggests that the noisy initiation behaviors observed at the cellular level, including the local temporal heterogeneities along the D-V axis and the spatially mis-positioned initiating cells, are the result of variable MyoII contractility. It is possible, that this MyoII variability is a result of noise found within the spatial pattern.

To assess this possibility, Dr. Takeda performed correlation analyses between MyoII and Eve using live imaging. To image Eve in live embryos, our collaborator, Dr. Takashi Fukaya, engineered an Eve-LlamaTag line by inserting the GFP LlamaTag into the endogenous *eve* locus at the C-terminus of its coding region and combined it with the maternally loaded, cytoplasmic GFP (Bothma et al., 2018). Dr. Takeda first verified that the Eve-LlamaTag intensities linearly scale with Eve immunofluorescent staining (Figure S4A and S4B). The Eve-LlamaTag was imaged together with MyoII-mKate2. At the cellular scale, both time-dependent and cumulative MyoII intensities correlate poorly with Eve intensities (Figures S4E and S4F; see also Figure S4C). At the tissue scale, the cumulative MyoII intensity summed across the “ribbon” of interfaces correlates slightly better with the mean intensity of Eve in the cell row posterior to the “ribbon” (Figure S4G, “A” correlation; see also Figure S4C). Analyzed the data

on an embryo-by-embryo basis, showed that in embryos in which MyoII intensities at interface (0) dominate, Eve intensities at P(+1) are comparable to P(0) (Figure S4H and S4I, Embryo 1 and 2), while embryos with high MyoII at interface (-1) show lower Eve at P(+1) (Figure S4H and S4I, Embryo 3 and 4), accounting for the modest tissue-scale correlation. Overall, however, low correlation coefficients at all levels indicates that MyoII variability does not scale with the patterning noise resulting from Eve variability. Consistent with this, quantification using coefficients of variation (CV) showed that the CV of MyoII far exceeds those of Eve (Figure S4J).

From the experiments and analysis performed by Dr. Takeda, I can conclude that, while there is some noise in the expression of Eve, the amount of variability of Eve expression between the P(+1) and P(0) cells does not account for the variability of the noise we see in MyoII behaviors. Thus, the extent of spatial information to which CF positional code provides for MyoII patterning is limited.

CF initiation requires the local activity of Btd and Eve, each of which plays a distinct role in the control of MyoII behaviors

Previous work had not elucidated the function of Btd and Eve on the behaviors of MyoII during CF initiation. To gain insights into how MyoII behaviors are controlled genetically, I sought to examine MyoII dynamics in *eve*, *btd* and *runt* mutant embryos.

It has been shown previously that *eve* mutants do not form a CF (Vincent et al., 1997) in the presumptive CF region, and the epithelium does not undergo any overt cell shape change or out-of-plane deformation prior to MD2 cell rounding (Movies S5 and S6). Quantitative analysis of *en face* imaging indicates low MyoII intensity and lack of planar polarization when the CF cleft should have formed (Figures 6C and 6D). Consistent with the lack of MyoII polarization,

the interconnected interfaces along the D-V axis retain a zigzag appearance (Figure 6E, *eve* mutant). This indicates that Eve is required for the enrichment and accumulation of MyoII during CF initiation.

Similar to the *eve* mutants, the *btd* mutants also do not form a CF (Vincent et al., 1997). Within the normal timeframe of CF initiation, the CF cleft was not observed (Figure 6F and 7A, *btd* mutant) in the *btd* mutant. However, many *btd* mutant embryos undergo out-of-plane deformation at later time points (Figure 7B). The timing and location of these lack consistency and given that the epithelium could be under compression due to GBE and mitoses. This suggests that these deformations could be a result of buckling instabilities (Figure 7C). *En face* imaging revealed polarized localization of MyoII near the embryonic surface in the presumptive CF region around the normal timing of CF initiation (Figure 8A; Movie S6). This, however, appears to be temporally concurrent and spatially contiguous with the polarized MyoII behavior in the presumptive GB region that has been previously described (Bertet et al., 2004; Zallen and Wieschaus, 2004). Coronal imaging showed that the MyoII foci are associated with the apical vertices, but these do not dynamically fluctuate along the lateral membrane as in the wild-type (Figure 8C; Movie S4, *btd* mutant). This loss of dynamic fluctuation along the lateral membrane in the *btd* mutant demonstrates that Btd expression is required for the CF-specific MyoII behaviors seen in the presumptive CF region.

Given that the Btd/Eve overlap is essential for the CF-specific MyoII behaviors, I asked whether this overlap spatially restricts CF MyoII behaviors. In *runt* mutants, in which the width of the Btd/Eve overlap is broadened, I observed an increase in the number of planar polarized supracellular MyoII cables (Figure 8B; Movie S3, *runt* mutant), consistent with the occurrence of the “type III+” initiation events (Figures 3H, 4G, 7A; Movie S4, *runt* mutant).

From these experiments, I identified the distinct roles that both Btd and Eve play in regulating the MyoII dynamics involved during CF initiation. Specifically, I showed that Btd expression is responsible for CF-specific MyoII behavior by redirecting MyoII to the lateral membrane of the initiating cells. Additionally, I demonstrated that expanding the Btd/Eve overlap causes more cells to acquire the CF-specific MyoII behavior.

Force transmission between interfaces across adherens junctions underlie CF spatial alignment

Although the Btd/Eve overlapping expression genetically confers and spatially restricts CF-specific MyoII accumulation and polarization, the contraction of CF cells is intrinsically noisy. Additionally, the contractile noise does not scale with genetic variability, suggesting that a denoising mechanism does not operate at the level of spatial patterning. The presence of planar polarized MyoII supracellular “ribbons” and initiating cells being linearly aligned suggests to me that the denoising mechanism is an emergent property of mechanical coupling at the tissue-scale. Mechanically coupled cells typically depends on the transmission of cellular forces across adherens junctions (Lecuit and Yap, 2015). To examine whether the linear alignment and precision of CF requires force transmission and mechanical coupling across the adheren junctions, I asked whether disruption of α-Catenin (α-Cat), the cytoplasmic linker between the actomyosin network and adherens junctions (Yonemura, 2011), affects CF alignment.

Live imaging analysis performed by Dr. Bolea Albero and Dr. Wang showed that the initiation of CF occurs normally, and in fact the depths of CF can often be greater in the *α-Cat* RNAi than in the wild-type (Figures 7A, *α-Cat* RNAi, and S5A), reminiscent of the dorsal fold phenotype reported previously (Wang et al., 2013). In contrast to this normal initiation and invagination, when the cells within the presumptive CF region were examined using the

angles formed by the interfaces, the *α-Cat* RNAi embryos showed a zig-zag pattern, contrasting with the wild-type (Figure S5B). This failure of interface straightening was confirmed on the tissue-scale by examination of the 3D tortuosity of the initiating cells. In wild-type embryos, the tortuosity decreases towards the apical side of the "ribbon", where the adherens junction integrate tissue-scale forces (Figure S5C and S5H-K), In contrast, *α-Cat* RNAi embryos lacked such a pattern (Figure S5C), suggesting that straightening of the interface at the junctional level is disrupted. To confirm that this failure to straighten the interface is not related to possible changes in the spatial patterning caused by the loss of *α-Cat*, immunostaining for Btd and Eve showed that the spatial patterning appeared normal Figures 4H and 4I). Additionally, the alignment of P(0) position remains precise (Figure S5D). Contrary to the precision of the P(0) position, examination of the CF cleft cells showed reduced linearity and an increased offset from a linear fit with the P(0) position and an increase in the percent mis-specification (Figures S5D and S5E).

A potential confounding variable while using the *α-Cat* RNAi embryos, is the possibility that MyoII dynamics are also affected by the loss of *α-Cat.* This suggests that the loss of spatial linearity within the initiating cells as well as the increase deviation between the initiating cells and the P(0) position may be the result of additional noise from MyoII that was generated in the *α-Cat* RNAi embryos. To determine if MyoII is affected by loss of *α-Cat*, Dr. Bolea Albero analyzed 1) the mean MyoII voxel intensity, 2) the percentage of MyoII voxels, and 3) the noise (measured by the coefficient of variation) for the MyoII voxel intensities that are located along "ribbon" that was previously described. Analysis showed that there was no statistical difference in the mean voxel intensity of MyoII or a change in the percentage of MyoII voxels, indicating that the amount of MyoII accumulation is not affected by the loss of *α-Cat* (Figures S5F-G). Additionally, there was no significant difference between the noise seen in MyoII noise (Figures S5F-G). Taken together, the phenotypes seen in the *α-Cat* RNAi embryos

cannot be attributed to an alteration in the MyoII behavior; suggesting that force transmission through the junctions underlies the spatial alignment of initiating cells during CF formation.

Local reduction of myosin contractility via optogenetics temporarily disrupts mechanical continuity and increases imprecision in CF spatial alignment

Next, I sought to disrupt tissue-scale mechanical coupling via local, direct perturbation of MyoII contractility. I reasoned that this could sever the “ribbon” and temporarily create two furrow structures that are mechanically decoupled. Rho1 GTPase activates MyoII to promote contractility (Levayer and Lecuit, 2012; Matsumura, 2005). To locally reduce MyoII contractility with spatiotemporal specificity, Dr. Bromley employed an optogenetic system, opto-DNRho1, that allows for light-dependent membrane recruitment of a dominant-negative Rho1 construct, CRY2-mCherry-DNRho1, to the plasma membrane anchor, pmGFP-CIBN (Guglielmi et al., 2015). In the absence of photoactivation, CRY2-mCherry-DNRho1 does not affect cortical contractility as it is localized in the cytoplasm.

Dr. Bromley first tested whether this optogenetic system can be used to block CF formation. To induce the CRY2 conformational change required for CRY2-CIBN dimerization, she used two-photon excitation at $\lambda = 950$ nm to illuminate a rectangular ROI that covers the entire lateral region of the pre-CF domain at least 20 minutes prior to the end of cellularization. Within the illumination ROI, she observed efficient recruitment of CRY2-mCherry-DNRho1 within 5 minutes at the plasma membrane (Figure S6A). To visualize cell shape, she used two-photon illumination at $\lambda = 1040$ nm to excite a membrane localized Gap43-mCherry probe, which has been shown to have no effect on CRY2 recruitment (Izquierdo et al., 2018). In the experimental embryos, in which both CRY2-mCherry-DNRho1 and pmGFP-CIBN are expressed, cortical

recruitment of DNRho1 disrupts CF formation (Figures S6C and S6E, 100%, n = 6). Coronal sections revealed that the CF cleft does not form, indicating that interface shortening is blocked. In contrast, control embryos that express CRY2-mCherry-DNRho1, but not pmGFP-CIBN, form the CF cleft at least 9 minutes before MD2 mitotic rounding, indicating that neither the illumination protocol nor the cytoplasmic DNRho1 affects CF initiation (Figures S6B, S6D and S6E, 86%, n = 7). These experiments demonstrate that the opto-DNRho1 system can block CF initiation, supporting that CF initiation depends on myosin contractility.

To investigate whether local activation of opto-DNRho1 reduces contractility locally, Dr. Bromley illuminated a narrow strip ROI (“activation ROI”) that bisects the pre-CF domain (Figures S6F and S6G). she imaged the CF region *en face* in a lateral ROI spanning ~15 cells along the D-V axis (“imaging ROI”). Because the embryonic surface is curved, imaging a single Z plane produces the visual effect that initiation at the periphery of the imaging ROI begins earlier than at the center, as the central cells are imaged at a more basal position. This visual effect allowed us to quantify the time gap between the descent of the last cells outside and inside the activation ROI. She found that the time gap is longer in the experimental embryos than the controls. The delay in initiation indicates that local activation of opto-DNRho1 autonomously reduces lateral MyoII contractility (Figure S6H). To find out whether local opto-DNRho1 activation mechanically decouples the two flanking furrows, she measured the angles between the interconnected interfaces (0) and found that those within the activation ROI are smaller with opto-DNRho1 than without, while outside the ROI there is no difference between control and experimental embryos (Figure S6I). These results indicate that opto-DNRho1 locally perturbs interface straightening, suggesting a decrease in mechanical coupling. She next assayed the spatial alignment between these two furrow structures. She quantified the extent of deviation from perfect alignment before they connect across the

activation ROI (Figures S6F, S6G and S6J) and observed greater deviation in the experimental embryos than the controls (Figure S6K).

Take together with the α-Cat RNAi experiments, the optogenetic studies demonstrate that tissue-scale mechanical coupling of CF initiating cells ensure the spatial precision and linearity of the cephalic furrow.

3D vertex modeling reveals that a CF-like mechanical system is robust against spatial and temporal noise

The experimental data suggest that mechanical coupling at the tissue-scale functions as a noise correction mechanism to ensure precision. I wanted to examine this experimental interpretation via a theoretical approach. Our collaborator Dr. Wen in the Shibata lab formulated a 3D vertex model [Eq.(1-2), Methods] based on the 2D model that he described previously (Wen et al., 2017). In this 3D model, the early embryonic epithelial tissue is modeled as a flat sheet of cells represented by an interconnected array of hexagonal prisms composed of vertices and edges. The edges contain tunable mechanical tension or elasticity and change their lengths based on force balance and energy relaxation, while the sheet itself has a defined geometry with free boundary conditions.

Dr. Wen first examined whether the 3D model phenomenologically recapitulates key morphological features when subjected to our empirically determined CF-like mechanical conditions, i.e. planar polarized lateral contraction [Eq.(3), Methods]. He found that the epithelium exhibits substantial out-of-plane deformation, as measured by the z distance between the highest and the lowest vertices on the apical surface (Figure S8A; “CF”). He also observed planar alignment of the lateral interfaces (Figure S8B; “CF”), recapitulating the interface straightening observed during CF initiation (Figures 3E and 3G). In contrast, only

one of these two was observed when other mechanical conditions were used (Figures S7A and S7B). Specifically, he observed 1) out-of-plane deformation, but no planar alignment with an isotropic increase of lateral contraction ("CF_{homo}"), 2) a modest degree of out-of-plane deformation, but no alignment with an isotropic reduction of apical perimeter simulating VF-like apical constriction [Eq.(4), Methods; "VF"], and 3) efficient planar alignment, but minimal out-of-plane deformation with an increase of planar polarized apical line tension that simulates GBE-like mechanics [Eq.(5), Methods; "GBE"]. Thus, planar polarized lateral surface tension can produce CF-like morphological features at the tissue scale, while non-polarized lateral tension, VF-like or GBE-like mechanical modulation cannot, providing theoretical support to our experimental interpretation.

To simulate a CF-like initiation process with noise, Dr. Wen made two modifications to the prototypical model described above. First, he immobilized the basal vertices to prevent unrealistic basal deformation, which phenomenologically approximates the high levels of MyoII at the basal surface that likely acts as an anchor (Figure 4A). Second, he introduced differential interface tension that reflects our experimental observations that the contractility was increased, in descending order of magnitude, at interfaces (0), (-1) and (+1) (Figures 2D and S2D). He called this model tension pattern (a), and it exhibits an all-type II initiation behavior [Figures S7A and S7B, pattern (a)]. He introduced two types of noise to the model. (i) To simulate spatial noise, he designed five additional tension patterns, schematized in Figure 6B as patterns (b) to (f), to mimic situations that were observed experimentally, such as the presence of a mixture of type I and II cells, and the existence of mis-specified cells. (ii) To simulate temporal noise, he added random Gaussian white noise to the prototypical tension pattern (a) [Eq.(6), Methods]. The noise is set to have a zero mean across the tissue at any given time and for any individual interface over the entire simulation time, so that the added noise does not alter the global mechanical settings at long timescales. The strength of noise is

tuned by the SD (σ), where high σ represents strong noise. Together, he chose σ values that produce spatial variabilities of contractility (Figure S7C) that are comparable to those observed in the experiments (FigureS 4J). To assess variability, he analyzed four morphological features: the straightness of interface alignment, the depth of furrow deformation, and the cross-sectional profiles of furrow depth along D-V axis and A-P axis (Figures S7C-S7E). For the six distinct spatial tension patterns, he found that the alignment of interfaces is swift and near perfect (Figure S7D, D1). The fold depths are very similar throughout the simulation duration and along the D-V axis with small SD relative to the length scale of the cells (Figure S7D, D2 and D3), and the A-P cross-sectional profiles are also quite similar (Figure S7D, D4). These results suggest that the CF-like mechanics are robust against spatial noise. Similarly, when he simulated with added temporal noise, he found that the degree of variability is small among iterations of simulations across a wide range of noise strengths (Figure S7E, E1 and E2). The D-V and A-P cross-sectional profiles are almost indistinguishable among multiple iterations of random noise (Figure S7E, E3 and E4). Thus, the 3D vertex modeling data provide theoretical evidence that a CF-like system is intrinsically robust against mechanical noise.

Conclusion

The predominant view on developmental precision posits that complex gene regulatory networks produce high-content and reproducible positional information. As a natural outcome, phenotypic consistency emerges. Despite this, in our study we showed that the precision of information content *per se* are insufficient to ensure invariant morphology, if the interpretation is variable due to heterogeneous cell behaviors or minor levels of noise in the genetic patterning. In the context of CF initiation in the early *Drosophila* embryo, we identified tissue-scale mechanical coupling as a denoising mechanism that refines the variability of initiation events. It is this denoising mechanism that ensures spatial precision of the epithelial fold

structure, despite noisy mechanical behaviors downstream of an otherwise precise genetic patterning network.

Chapter 4: Pursuit of cellular effector genes that are downstream of the Btd/Eve regulatory circuit

Introduction

A crucial question left unanswered in chapter 3 concerns the cellular mechanism downstream of Btd and Eve that controls the CF-specific MyoII behavior. I have demonstrated that Btd and Eve play distinct roles in controlling MyoII activity within the CF region, but the downstream targets of the initiating cells remain unknown. To identify potential effector genes within the presumptive CF region, I sought to identify genes that are actively transcribed and translated in the CF initiating cells.

Identifying components of a genetic pathway has historically relied on comparative analysis of gene expression profiles generated through microarrays (Sobek et al., 2006). Recently, major advancements have been made to improve the spatial and temporal accuracy of gene expression profiles through the adoption of RNA sequencing (RNAseq) technology and next-generation sequencing (NGS) to precisely quantify the RNA present in a biological sample at any given time (Chu and Corey, 2012).

To identify the gene expression pattern of individual cell populations, attempts have been made to combine GFP tagged proteins and Fluorescence-activated cell sorting (FACS) (Porter et al., 2017). In the procedure, a GFP reporter was expressed in specific cell populations and processed through FACS sorting to isolate the GFP containing cells. Once isolated, the mRNA can be sequenced, and the expression pattern obtained.

Early applications of RNAseq was performed on the *Drosophila* embryo, to obtain embryo-scale quantitative data of gene expression. Through a technique known as SliceSeq (Combs and

Eisen, 2013), the embryo scale RNA expression pattern was obtained by cryosectioning along the A-P axis of the *Drosophila* embryo. RNAseq analysis was performed on individual cryosections, and the results were compiled and revealed temporally and spatially refined gene expression data at discreet locations along the A-P axis of the embryo (Combs and Eisen, 2013). Recently, RNAseq has advanced to the state where the transcriptomes of individual single cells (scRNAseq) can be identified, allowing for the single cell mapping of gene expression (Karaiskos et al., 2017; Wagner et al., 2018).

While SliceSeq and scRNAseq have drastically improved on quantitative analysis of gene expression, both techniques are not without their flaws. The SliceSeq methods requires the embedding and sectioning of embryos, which requires a high level of spatial precision and orientation of sectioning. This can lead to spatial inaccuracy and cross contamination of individual slices, resulting in faulty data. Additionally, cell sorting through FACS analysis involves destruction of the embryo which can alter mRNA levels and skew results. A major setback for these procedures is the mapping of RNAseq data to individual positions within the embryo. Which requires a highly precise reference database of known expression patterns. Currently only established expression patterns exist for wild-type embryos, but not for different mutant backgrounds making it difficult to dissect alterations in gene expression in different genetic backgrounds. Lastly, there are differences between genes being transcribed and what genes are being translated, suggesting that transcriptome analysis may not accurately reflect which mRNA are translated to functional proteins (Li et al., 2018).

For my research, I have chosen a recently established method of identifying gene expression within specific cell populations. Translating Ribosome Affinity Purification (TRAP), is an effective method to isolate and identify genes that are actively being translated in cell populations (Heiman et al., 2008, 2014). The backbone of TRAP relies on the expression of GFP-tagged ribosomes under the control of a cell type specific enhancer. By expressing the TRAP construct

in a specific population of cells, it is in principle possible to isolate GFP-tagged ribosomes from those cells by simply homogenizing the whole embryos, followed by standard immunoprecipitation, avoiding the need to establish an effective cell dissociation and FACS sorting protocol and without the concern of damage response that the cells might trigger during cell dissociation. Following the enrichment of GFP-tagged ribosomes from the target cell population, the mRNAs that are associated with these GFP-tagged ribosomes could be isolated for RNAseq analysis, thus allowing the identification of transcripts that are actively translated in this specific cell population. In addition, this method could potentially be implemented in embryos mutant for *btd* or *eve*, thereby allowing for identification of Btd- or Eve-dependent genes that are specifically expressed in the CF initiating cells.

In the following sections, I will describe the progress that I have made in implementing this method for the isolation of CF-specific genes.

Region-specific expression of GFP-tagged ribosomes in the early *Drosophila* embryos

To isolate GFP-tagged ribosomes, I incorporated key enhancers for btd and eve into the TRAP system. While the expression of Btd is driven by a single enhancer (Wimmer et al., 1997), the expression of the Eve stripes is controlled by five enhancers. Eve stripe 1 (Eve1), 2 (Eve2), and 5 (Eve5) are controlled by their own unique enhancer regions (Sackerson et al., 1999). Eve stripe 4 and 6 share a single enhancer region (Eve4+6) and Eve strip 3 and 7 also share their own unique enhancer (Eve3+7) (Sackerson et al., 1999). For my experiments I incorporated the enhancers for Btd, Eve1, Eve2, and Eve5 into the TRAP expression system (Figure 8A). By driving the TRAP system with the Btd and Eve1 enhancers, I can target the cells in the presumptive CF region. TRAP expression via the Eve2 and Eve5 enhancers will allow me to rule out genes that are downstream of *eve* that are not specific to the CF region. Additionally,

the expression of Eve1, Eve2, and Eve5 are controlled by individual enhancers that do not regulate the expression of other stripes, like the Eve4+6 or Eve3+7 enhancers (Sackerson et al., 1999), allowing me to spatially restrict the translatome data to only areas of interest.

Embryos expressing TRAP constructs being driven by either Btd, Eve1, Eve2, or Eve5 enhancers were live imaged using two-photon imaging to confirm successful expression (Figure 8B). From the imaging results, I was able to verify that the TRAP constructs are expressed during embryogenesis. Surprisingly, the expression of the constructs appeared to be wider than expected and didn't appear to undergo spatial refinement that is normally seen (Figure 8B), but CF formation did not appear to be disrupted (Figure 8B, yellow arrows). To verify this, I performed fixed immunofluorescent imaging using Btd and Eve antibodies. When I compared the expression of the GFP-tagged ribosomes to the native expression of Btd and Eve, I found that the expression of the TRAP construct was indeed wider than the protein expression in the case of Eve1 and Eve2, and in the case of Eve5, the TRAP construct did not overlap with the endogenous protein expression (Figure 8C).

From these data, the current TRAP constructs express GFP-tagged ribosomes in a larger area than the intended pattern. It would be desirable to improve the spatial restriction of the TRAP expression (see Chapter 6 for further discussion) to isolate the CF-specific translatome. Nonetheless, the current constructs could potentially provide a substantial degree of enrichment for the CF-specific transcripts that are actively translated. Because of this, I decided to proceed with the development of a protocol for the isolation of the GFP-tagged ribosomes.

Development of an isolation and purification protocol for GFP-tagged ribosomes from the *Drosophila* embryos

I wanted to confirm that I was able to isolate the GFP-tagged ribosomes using the established protocol before proceeding. While the TRAP constructs described above could provide a reasonable amount of CF-specific transcripts, the cell type specific expression of the TRAP construct limits the number of GFP-tagged ribosomes I can purify, making potential trouble shooting difficult. To overcome this, I chose to express the TRAP construct ubiquitously using a maternal-tubulin driver and the Gal4/UAS expression system. By doing this, I will be working with a larger number of GFP-tagged ribosomes, which will allow me to refine the established protocol to suit my experimental system.

Using two-photon imaging, I confirmed that using the maternal-tubulin GAL4 driver, the UAS-TRAP construct was expressed ubiquitously (Figure 8C, left column). I proceeded to collect embryos from two time points; 1) embryos from an overnight lay that represent a broad collection of embryos aged between 0~12 hours, designed to see whether it was possible to isolate tagged-ribosomes, and 2) a timed (2.5-3.5hr) lay, aimed to assess the feasibility of the TRAP strategy in harvesting sufficient amount of GFP-tagged ribosomes under a tighter temporal control that could better match the timing of CF formation. Embryos from these two time points were homogenized in the lysis buffer described in the established protocol (Heiman et al., 2014), and separated via centrifugation into an aqueous fraction, representing the cytoplasmic contents of the embryos (Figure 9A, P2 supernatant), and an insoluble fraction composed of yolk and membrane bound organelles (Figure 9A, P2 pellet). Additional detergents were added to both fractions to further disrupt membrane structures for an additional round of fractionation, resulting in four distinct fractions (Figure 9A, F1-F4). Western blot analysis showed that for both timepoints GFP-tagged ribosomes can be isolated through

immunoprecipitation using α-GFP nanobodies coupled to magnetic beads (Figure 9B, F1 and F2; 9C, F1 and F2). But, despite the purification of the cytoplasmic fraction, GFP-tagged ribosomes were still present in the insoluble fraction at both timepoints (Figure 9B, F3 and F4; 9C, F3 and F4), suggesting that the current protocol is not sufficient to fully extract GFP-tagged ribosomes that are associated with membrane organelles such as the Endoplasmic reticulum (Kratz et al., 2014).

Conclusion

From my preliminary experiments, I have tested the feasibility of isolating mRNAs that are actively translated in specific cell populations in the developing *Drosophila* embryo using the established protocol. The results that I have obtained thus far suggest the need of further optimization. I will discuss potential future improvement of the current procedure in Chapter 6.

Chapter 5: Examination of the function of the CF

Introduction

The function of the CF remains unclear. While some research has attempted to address the functionality of the CF (Costa et al.,1993; Dicko et al., 2017), the lack of any solid experimental data fails to provide a clear function of the CF. Given the transient nature of the CF, it is understandably difficult to examine the function of the CF as the cells within the CF are not fated to any specific cell type (Hartenstein and Campos-Ortega, 1985). Additionally, a putative CF specific gene has not been identified, rendered targeted destruction of CF using genetic mutants or RNAi infeasible. While *btd* and *eve* mutants fail to form a CF (Vincent et al., 1997), both are transcription factors that may have numerous downstream targets that extend beyond those required for CF initiation (Li et al., 2008). Given the robust and stereotypical formation of the CF in *Drosophila melanogaster*, the CF must serve some function during development. Understanding its function can provide greater insights into the role of epithelial folds during embryonic development.

To address the functionality of the CF, I designed two separate approaches within the limitation of our current ability to targeted manipulate CF formation. Specifically, in the first approach I attempted to remove only the Eve1 expression, while leaving the remaining Eve stripes undisturbed. The rationale was, while it remains possible that Eve1 expression has target genes unrelated to CF and the embryonic phenotype of embryos that have lost Eve1 may reflect the requirement of those, Eve1 deletion represents the best targeted disruption of CF that one can achieve at the present time. In the second approach, I attempted to mimic the Btd/Eve expression pattern seen in the CF region in another region of the embryo to seek to ectopically generate a CF. This strategy aims at first assessing the sufficiency of Btd/Eve overlap in

reconstituting the CF-like behaviors in a different part. In the sections described below, I will present the results that have been obtained thus far.

Localized requirement of Eve expression for CF initiation

To explore the local requirements of Eve1 expression, I had sought to express Eve either only in the Eve1 region or in all other Eve stripes (Eve2-7), except Eve1. Dr. Wang has previously generated flies that only express the Eve1 stripe based on the work of Dr. Fujioka by using the Eve1 enhancer to drive the expression of the *eve* coding sequence within an *eve* mutant embryo (Sackerson et al., 1999). Additionally, Dr. Takeda generated flies that does not express Eve1 and does not perturb the expression the remaining Eve stripes (Figure 10A, eve^{R13}*+Eve2-7*). To accomplish this, Dr Takeda used a recombineering approach on a BAC construct that encompassed the entire Eve locus to remove the stripe1 enhancer(Sackerson et al., 1999) and the Late Element (Fujioka et al., 1995) (Fujioka et al., 1995), resulting in the Eve2-7 genomic construct. Note that, for live imaging purposes, the Eve2-7 construct contained an in-frame fusion of the fluorescent protein mNeonGreen at the C-terminus of the coding region of *eve*. Both the transgenics constructs of Eve1 and Eve2-7 crossed into the *eve* mutant background. Using these files, I examined the formation of the CF with the presence or absence of Eve1 expression.

Immunostaining of *eve* mutant embryos expressing Eve1 showed that the CF is formed normally (Figure 10B, wild-type and eve^{R13}*+Eve1,* yellow arrows). In contrast to this, Immunostaining of eve mutants expressing Eve2-7 showed that the CF fails to form in the presumptive CF region similar to the *eve* mutant (Figure 10B, wild-type and eve^{R13}*+Eve2-7,* yellow arrows). From these data, I demonstrated that localized Eve activity, specifically Eve1, within the CF region is sufficient and necessary for CF formation. These data indicate that a genetic condition, namely eve^{R13}*+Eve2-7*, has been established to allow for targeted elimination

of CF, while leaving all other embryonic regions intact. These embryos have the potential to unlock the mystery of CF functionality.

Analysis of the spatial contribution of Eve on MyoII regulation in CF and GBE regions

It is possible, given the role of Eve in promoting MyoII accumulation, that the MyoII behaviors are linked between the CF and the GBE. It is possible that in addition to the local requirement of Eve1, CF initiation may depend on Eve expression within the GBE encompassing the remaining Eve stripes (Eve2-7). To see if the MyoII behavior in the GBE influences the cell behaviors seen in the CF, I asked whether to CF MyoII behaviors could be decoupled from the GBE.

En face imaging of the *eve* mutants showed a decrease in MyoII expression as well as a decrease in planar polarization (Figure 11A and 11B). Interestingly, in the *eve* mutant I saw two distinct behaviors in the epithelial layer in which the basal MyoII disassembles early and leads to retraction of the basal surface towards the apical surface (Figure 11C), or late disassembly in which I see apical shift of the basal surface, but the basal MyoII pool is still intact (Figure 11D). In *eve* mutants that express only Eve1, *en face* imaging reveals the increase of MyoII intensity and polarization in the CF region leading to CF cleft formation, whereas in the GB region, low levels of MyoII intensity and polarization were observed, similar to the wild-type (Figures 11E, 11G, 11I and 11J; Movie S7, wild-type and eve^{R13} + Eve1). In contrast, in the *eve* mutant embryos that express only Eve2-7, MyoII intensity and polarization are low both in the pre-CF and GB region 14 minutes prior to MD6 anaphase onset, similar to the *eve* mutant (Figures 11F, 11H, 11I; Movie S7, $eve^{R13}$and eve^{R13} + Eve2-7).

These data suggest that local Eve activity is essential for CF-specific myosin behaviors, whereas Eve expression in the trunk is dispensable. Thus, CF initiation can be decoupled from GBE. The caveat with this analysis, is that Eve1 may be playing other developmental roles in addition of CF formation and thus making it difficult to separate out phenotypes associated with the loss of the CF, and the phenotypes associated with the loss of Eve expression.

Analysis of phenotypes associated with mis-expression of Btd

A key feature present in the CF region is the overlapping expression of Btd and Eve which is necessary to trigger CF initiation (Vincent et al., 1997). Since I have demonstrated that Eve1 expression is sufficient to induce CF formation in the normal CF region of the embryo where Btd is present, I wanted to explore whether other Eve stripes can also induce CF-like cell shape change and folding behaviors if Btd is expressed. To explore the sufficiency of Btd/Eve overlap in triggering CF initiation, I sought to ectopically recreate the Btd/Eve overlap in regions posterior to the presumptive CF region.

I first attempted to generate ectopic Btd/Eve overlapping expression by ubiquitously expressing Btd using a maternal-tubulin driver. Immunofluorescent analysis confirms that a uniform amount of Btd was expressed throughout the embryo (Figure 12B, *MatGal4>Btd*). While the *per cell* expression level of Btd was not as high as the endogenous Btd, in a *btd* mutant, it appears to be sufficient to generate a CF-like structure in the CF region of the embryo. These results suggest that despite being uniformly expressed, global mis-expression of Btd produces an overlapping region in the Eve1 region that is capable of inducing CF-like formation. One potential caveat of this analysis is that I have now ruled out the possibility that the CF-like structures that I obtained in these embryos are in fact bucklings that can often be observed in *btd* mutants (Figure 7C, *MatGal4>Btd*, green arrow). When I examined the lateral surface of embryos expressing

uniform Btd in both the wild-type and *btd* mutant backgrounds, I found the presence of shallow wrinkles along the lateral surface of the embryo (Figure 12C, *MatGal4>Btd*, cyan arrows). Although these wrinkles suggest the possibility that ectopic Btd expression in the non-CF regions induces CF-like initiating cell behaviors, I did not perform a cellular scale analysis, and thus cannot be certain that these indeed result from cell shortening and lateral interface shrinkage, features that characterize CF initiation. While these data remain preliminary, they suggest that only the Eve1 region is primed to initiate CF.

To examine this possibility, I used two different local Gal4 driver to mis-express Btd. Using a driver localized anteriorly by the *bicoid* 3'UTR, I found that cephalic furrow formation in the Eve1 region can be rescued in *btd* mutants, similar to the ubiquitous expression of Btd (Figure 12C, *BcdGal4>Btd*, green arrows). In the region posterior to Eve1, I did not observe any visible wrinkles, consistent with the spatial of pattern of this mis-expression, which appears to pass just the first stripe of eve (Figure 12B, *BcdGal4>Btd*). In contrast, when I used the *Krüppel*-Gal4 driver (Figure 12B, *KrCD1Gal4>Btd*), whose expression spans between the second and fifth stripe of Eve, I observed deeper and more pronounced wrinkles in regions posterior to Eves (Figure 12C, *KrCD1Gal4>Btd*, cyan arrows). As the experiments described above, I did not perform a cellular scale analysis and cannot ascertain whether these wrinkles display features of CF initiation. Surprisingly, however, in *btd* mutants, I observed rescue of cephalic furrow formation in the Eve1 region (Figure 12C, *KrCD1Gal4>Btd*, green arrow). This result remains puzzling as Eve1 is outside of the *Krüppe*-Gal4 expression domain (Figure 12A, *KrCD1Gal4>GFP*). Given the frequent buckling instabilities seen in *btd* mutant, it cannot be ruled out that this is not a rescue but buckling. Taken together, the preliminary data generated with the local Gal4 drivers also tentatively support the idea that the Eve1 region is primed to form a CF-like structure.

To further analyze the local potential of CF induction, I mis expressed Btd using a flip-out expression system. The flip-out system is a genetic method that allows site-directed recombination of DNA segments using a recombination enzyme called flipase (FLP) (Theodosiou and Xu, 1998; Wimmer et al., 1997). Dr. Wang and I chose to utilize the FLP system to ensure that Btd is specifically expressed in the maturing spermatocytes, thus ensuring early expression independent of the time required for UAS/Gal4 maturation time (Struhl et al., 1993). In my experiments, membrane localized GFP (CD4-GFP) and an SV40 polyA sequence, were flanked by flipase recognition target (FRT) sites (FRT-CD4-GFP-FTR) followed by *btd* cDNA (Figure 13A). In the absence of FLP, the embryo expresses CD4-GFP, providing a visual marker for the expression of the construct. When female flies expressing the FRT-CD4-GFP-FRT construct are crossed to male files expressing male-specific FLP, the FRT-CD4-GFP-FRT cassette is excised, allowing the transcription of *btd* cDNA.

I constructed FLP mediated Btd misexpression constructs under the control of the Btd, Eve1, Eve2, and Eve5 enhancers. Two-photon live imaging confirmed the pre-flipped expression of CD4-GFP. Similar to the TRAP experiments, the expression domains of CD4-GFP were wider than expected, but CF formation was again not altered (Figure 13B, yellow arrow). Focusing primarily on the embryos that utilize the Eve 2 enhancer (Eve2), I crossed females expressing FRT-CD4-GFP-FRT to males with germ line specific β-tubulin driven FLP to ensure early expression. I was unable to visualize the misexpression of Btd through immunostaining (Figure 13C, flpeve2>Btd), but when the flip-out was performed in a *btd* mutant, I saw that CF formation appeared to be restored (Figure 13D, flpeve2>Btd, green arrow). This suggests that misexpression of Btd at Eve2, given its wide expression pattern, is sufficient to induce a CF-like structure in the Eve1 region. Once again, however, the possibility that the CF-like structures that are considered as evidence of rescue are in fact bucklings cannot be ruled out, but further analysis of the cell behaviors will shed insight on the if these buckling events are indeed CFs.

Conclusion

Through genetic manipulation of Eve expression, I have demonstrated that localized activity of Eve1 is essential for CF formation. Local Eve activity in the Eve1 region likely ensures the accumulation of MyoII to the lateral interface of CF initiating cells to induce CF formation. Additionally, the localized initiation behaviors in the Eve1 region appear to be independent of germband extension, suggesting that CF formation can be decoupled from GBE.

From the Btd misexpression experiments I performed; it looks as if that Btd could be sufficient to induce a CF-like structure mainly within the presumptive cephalic furrow region of the embryo. Further examination of the cell behaviors will be needed to ascertain if these CF-like structures are formed with characteristics typical of the CF initiating cells, and not buckling instabilities that often occur in *btd* mutants. The true test of sufficiency would be the ability for Btd expression to trigger CF formation in other regions of the embryo, provided the presence of Eve. This remains inconclusive, despite the presence of wrinkles. Taken together, my data thus far suggest that the Eve1 region could be specifically primed to form the CF. A tentative, yet interesting observation was that in the wild-type background, misexpression of Btd tends to lead to the appearance of ectopic wrinkles in regions posterior to Eve1, whereas in the *btd* mutant background, misexpression of Btd appears not to show the same degree of wrinkle formation. It remains unclear why this is the case, however.

Chapter 6: Future directions

Refinement of translatome analysis

In this thesis, I have adapted a methodology to identify cell-type specific translatomes using translating ribosome affinity purification (TRAP). From the preliminary experiments I performed, it seems possible to purify GFP tagged ribosomes from embryos expressing the TRAP construct ubiquitously (Figure 9B and 9C, F1). Expressing TRAP using the Eve stripe and Btd enhancers, however, further improvement in spatial resolution would be desirable (Figure 8B).

One possibility that can explain the spatially broad expression of the TRAP construct, could lie within the actual construct itself. TRAP was designed originally for use in determining the translational profile of mammalian CNS cells (Heiman et al., 2008) and later adapted for use in *Drosophila* brain (Thomas et al., 2012). In these systems, the analysis was being performed at later stages in development and the level of protein turnover and regulation could be significantly different from the early embryo. Because more differentiated cells could be expressing the target protein at a stable level, the requirement for mimicking the endogenous regulatory dynamics is less stringent. For this potential reason the original TRAP construct that was used in the previous studies, as well as the initial experiments in this project, contained the SV40 3'UTR (Figure 8A). Like most poly(A) tails, SV40 poly(A) tail is commonly used to end transcription of mRNA and provide stability of mRNA transcripts (Banerji et al., 1981; Kosman and Small, 1997). The presence of the SV40 terminator likely allows the expressed mRNA to perdure for a prolonged period time. It is interesting that the broad pattern of expression is similar to the early stages of Eve stripe refinement. Given that the refinement of Eve expression relies on the regulatory sequences found within the 3'UTR of the Eve locus (Sackerson et al., 1999) and the *eve* 3'UTR can lead to rapid turnover over of mRNA sequences (Kosman and

Small, 1997), it could be possible to use the *eve* 3'UTR, in place of SV40, to remake the TRAP constructs. Considering that I want the expression of the TRAP constructs to mimic the endogenous expression as much as possible, I will remove the SV40 element and place the GFP-tagged ribosome cDNA under the regulation of both 5' and 3' UTR sequences of *eve*, while using the *btd* UTR sequences for the TRAP construct driven by the Btd enhancer sequence. By recapitulating the regulatory mechanisms found natively at the *eve* and *btd* loci, I expect the expression of the TRAP constructs will undergo refinement.

In addition to refining the spatial expression of the TRAP construct, the extraction of the GFP-tagged ribosomes also needs improvement. Given the fractionation procedure (Figure 9A), the pellet is mainly composed of membrane bound components, including the endoplasmic reticulum (ER) and Golgi. Presence of GFP-tagged ribosomes in the pellet could potentially be ER-bound ribosomes that are translating proteins into the secretory pathway of the cell. In previous studies using TRAP, a significant number of genes expressed in the secretory pathway were not present in the first rounds of analysis of the cytoplasmic fraction (Kratz et al., 2014). This suggests that the isolated ribosomes located in the pellet could potentially be translating membrane localized proteins.

This problem can be addressed by systematically changing the purification protocol. One possible method to overcome this problem is to repeat the experiments using a much stronger lysis buffer, such as radioimmunoprecipitation assay buffer (RIPA), which is more denaturing than the buffer used in the established protocol (Heiman et al., 2014). In addition to switching to a more aggressive lysis buffer, the addition of stronger detergents will aid in the disassociation of membrane organelles.

Identify the role of the cephalic furrow during embryogenesis and its evolutionary function through ectopic furrow formation

The transient nature of the cephalic furrow has proven to be a large setback in determining its function and its evolutionary significance. The results in this thesis raises a few important questions that directly impacts the functionality of the CF. Specifically, can the CF only form in a "zone of competence" which is defined by explicit embryonic location specified by the Btd/Eve1 region, or is the co-expression of Btd and Eve alone sufficient to trigger CF formation?

A key tool that will help me examine the function of the CF is the Eve2-7 mutant embryo that lacks expression of Eve1 (Figure 10A and 10B, *eve*^{R13}*+Eve2-7*). By genetically ablating Eve1, I have a system in which I can examine the role of the CF during embryogenesis by examination of gastrulation events such as VF and GBE behaviors. As stated earlier, the main caveat with this embryo, is that Eve1 could have other transcriptional targets. Despite this caveat, this mutant embryo provides more spatially targeted disruption of Eve expression than the *eve* mutant embryo. Further characterization of the *eve*^{R13} *+Eve2-7* mutant embryo will provide insight as to the function of the CF during *Drosophila* gastrulation and development.

Additionally, with the establishment of the optogenetic system (Figure S6), I can further expand on the experiments performed by Dr. Bromley, and locally reduce MyoII contractility within the CF and observe embryo development. Using the optogenetic system, I will be able to disrupt CF formation, without altering the genetic components that specify the CF region.

Experimental data shown earlier in this thesis suggest the mis-expressing Btd in a more posterior region of the embryo induced wrinkles but failed to induce a full-fledges cephalic furrow like structure (Figure 12B and 13C). It has been shown that increasing the copy number of *bicoid* causes a posterior shift of the CF (Driever and Nüsslein-Volhard, 1988b). It would be

interesting to ectopically express Bcd through misexpression, rather than extending the anterior region. Additionally, the pair-ruled gene *paired* (prd) has been shown be promote CF formation (Blankenship and Wieschaus, 2001). It would be interesting to include these other factors, in addition to Btd and Eve, in the “cocktail” used for the induction of CF *de novo.*

Embryonic influence on cephalic furrow initiation events

The data I have presented shows that during CF initiation, the initiating cells take on two distinct cell behaviors (Type I and Type II). While the appearance and number of both these types is variable in any given embryo, it is possible that the initiating behavior could be influenced by the geometry of the *Drosophila* embryo. In wild-type embryos, the CF forms at an area where there is significant curvature and spatial confinement. CF position is not only dependent on Btd and Eve, but more so on the upstream maternal gene *bicoid*. Studies have shown that by increasing the copy number of *bicoid*, bcd expression extends more posterior and pushes the spatial location of the CF more posteriorly (Driever and Nüsslein-Volhard, 1988a, 1988b). Given that the lateral surface of the embryo is more curved the more posterior in the embryo, would the frequency of initiation types be affected by a more uniformly curved geometry?

Chapter 7: General discussion

Tissue-scale mechanical coupling as a denoising mechanism

From the data presented in my thesis, I have shown that CF initiation is spatially defined and refined through the overlapping expression of Btd and Eve. This spatially defined gene expression of Btd and Eve guides the differential activity of MyoII dynamics. While I have shown that the overlapping expression of Btd and Eve can confer near single cell row spatial information, the actual positional information that is used in CF specification appears to be “zone of cell competence” that has a much lower spatial resolution than what the transcription code of Btd and Eve can confer. This low resolution “zone of competence” is likely the result of the inability for the cells to convert transcriptional code into refined cellular contractility. Despite the low resolution in cellular contractility and lack of fidelity between the positional information and morphological changes , the developing embryo has managed to overcome this variability and provides a mechanism in which morphological events can precisely occur. This suggests that transcription-based spatial patterning can only provide a limited amount of information in specifying the location of morphological structure.

With spatial information providing a “zone of competence” for the CF to form, some intrinsic mechanism must be in place to ensure proper linear formation of the CF in the correct spatial location. During CF formation, the initiating cells manage to linearly align themselves, irrespective of the deviation from the positional information generated by Btd and Eve. This phenomenon indicates that instead of correcting the spatial positioning and behaviors of individual initiating cells, the epithelial tissue maintains spatial precision through the mechanical coupling of the initiating cells to ensure they remain spatially aligned.

In this thesis, my collaborators and I propose a MyoII based mechanical coupling mechanism that underlies the spatial precision of the CF, despite variability in positional information and cell behaviors. During CF initiation, we suspect that MyoII-dependent contraction of the lateral surfaces of the initiating cells provides localized tension. Through this tension, the forces generated in a single initiating cell can effectively be transmitted to the adjacent cells through the intercellular connections located at the adherens junctions. Resulting from this transmission of the MoyII generated tension, along the D-V axis of the tissue, the MyoII becomes planar polarized and aides in the straightening of the interfaces that are under tension. Through this mechanical integration, supracellular “ribbon” structures form along the D-V axis at the A-P boundaries of the cells. I propose that these supracellular “ribbons” mechanically mediate the self-organization of the initiating cells to ensure spatial alignment and precision of initiation events, despite minor deviation from the spatial information. From this, I propose that two mechanisms regulate and refine CF formation. First, the establishment of a “zone of competence” in which provides a general, but narrow, spatial localization for CF formation. Secondly, the stochastic mechanical patterning generated through tissue-scale mechanical coupling organizes the initiating behaviors within the “zone of competence” to further organize the initiating cells. Through the combination of these two mechanisms, the CF can faithfully form a linear structure despite the intrinsic variability in positional information and cellular contractility and allow the spatially precise tissue deformation to emerge from the fuzzy “zone of competence”.

While the mechanical coupling of cells at the tissue-scale appears to drive the formation of the CF, it is possible that force-dependent feedback mechanisms could be involved in the mechanical coupling as well. Previous research has suggested that applied forces could promote MyoII recruitment (Fernandez-Gonzalez et al., 2009), and effect the bulk transfer of actomyosin network components which synergizes with the activation/deactivation cycle of

MyoII contractility (Munjal et al., 2015). From these studies, it is possible that the enrichment and planar polarization of MyoII seen during CF initiation could be amplifying its own dynamics to further promote the alignment of initiating cells. In addition to the force dependent feedback, research has also shown that mechanical forces increase the strength of junctional resistance via conformational changes and the coupling strength of α-Cat (Buckley et al., 2014; Yao et al., 2014; Yonemura et al., 2010). At this stage, it is unclear if these additional mechanisms are playing a role in the mechanical coupling seen during CF formation. It is also unknown if any of these additional mechanisms are specified by the Btd and Eve transcriptional output.

One aspect that I did not address in my project is if the force transmission seen at the cell cortex are also transmitted into the nucleus to influence the spatial information generated by Btd and Eve expression. While not addressed specifically, I feel that it is highly unlikely that mechano-transcription feedback plays a role in the refinement and denoising of the CF. This is primarily due to the characteristic timescale of transcriptional feedback. In the CF system, the time it would take for transcriptional feedback to impact the spatial pattern is likely too long to be effective in denoising the minute-scale asynchrony of CF initiation. It would be interesting, however, to explore if the mechanics of CF folding have an impact on the transcription in later stages of CF formation (Gilmour et al., 2017). In particular, during the retraction of the CF, in which I have observed a loss of overlapping expression of Btd and Eve (data not shown). In which case, it would be interesting to explore if the folding process triggers the loss of overlapping expression and stimulates another mechanism that controls the retraction of the CF back into the epithelial layer.

The mechanical system underlying cephalic furrow formation

Epithelial folding requires localized changes in cell shape, being driven by either microtubule or MyoII dynamics. It has been shown previously that microtubule-based mechanical homeostasis

is driven by the remodeling of the apical-basal polarity of the cell polarity (Takeda et al., 2018; Wang et al., 2012). Additionally, localized contractility of the cell through actomyosin also has been shown to drive cell localized cell shape changes (Martin and Goldstein, 2014; Sawyer et al., 2010). I did not address microtubule dynamics directly during CF initiation, and chose to focus on the myosin dynamics during CF initiation. The initiation of the CF is initiated by myosin-dependent contraction of lateral membrane interfaces. This behavior of MyoII is distinctly different from the myosin-dependent apical constriction that has been thoroughly examined during VF formation, where the apical length of initiating cells decreases and an overall increase in lateral and cell length (Gelbart et al., 2012; He et al., 2014; Weng and Wieschaus, 2016). During CF formation, I observed a pronounced expansion of the basal surface of the initiating cells, which coincides with the disassembly and possible translocation of the basal MyoII meshwork (Figure 3A; Movie S2). This suggests that some basal relaxation mechanism allows for the rapid increase in fold depth, similar to the phase II process of VF formation (Krueger et al., 2018). This makes the initiating behavior of the CF unique from that of the VF.

CF is also distinct from the formation of the dorsal folds. During dorsal fold initiation, the adherens junctions of the initiating cells shift basally and transiently increasing the apical length prior to cell shortening (Wang et al., 2012). Examination of the CF in this project showed that the adherens junctions do not appear to shift basally, and I found that the lateral lengths decrease (Figure 5D). This demonstrates that CF initiation is also distinct from dorsal fold initiation.

At the cellular-scale, I have demonstrated that CF initiation is vastly different from the other prominent epithelial folds present during gastrulation of the *Drosophila* embryo. The unique cell behavior adds CF formation into a newly formed group of epithelial folds that are characterized by mechanical modulation of the lateral or basal surface (Krueger et al., 2018; Sherrard et al., 2010; Sui et al., 2018; Wen et al., 2017).

Evolutionary significance of the cephalic furrow

An outstanding question surrounding the CF is its biological function during *Drosophila* gastrulation. Unlike other epithelial folds in Drosophila, the CF is a transient fold that forms at the onset of gastrulation, and recedes back into the embryonic surface during mid to late gastrulation (Foe, 1989). In addition to not being maintained or undergoing further development internally, it does not serve as a starting point for the internalization and differentiating of other cells prior to the retraction back to the embryo surface. Additionally, classic fate map analysis of *Drosophila* embryogenesis suggested that the CF cells do not constitute a distinct cell fate (Hartenstein and Campos-Ortega, 1985). Given that the embryo has developed both spatial and mechanical mechanisms to ensure the formation of the CF, it is strongly implied that it serves some developmental function, thus stabilized evolutionarily in the lineage of higher flies including *Drosophila*.

It is possible that, given the precise spatial formation of the CF within the “zone of competence”, the CF is formed to ensure the specificity of cell fates. The formation of the CF is the first physical structure that potentially establishes the segmented body plan of the *Drosophila* embryo, by physically isolating the presumptive head region from the presumptive thorax. This physical isolation could restrict signaling between cells in the head and the thorax, thus allowing the cells to give rise to more specific cell fates (Gilmour et al., 2017). Additionally, the mechanical signals could induce or stabilize gene expression (Mammoto et al., 2012) of the surrounding cell populations. In which case, the CF could be acting as a potential signaling center that is required for further cell differentiation of the surrounding cells.

Another possible role of the CF is acting as a physical barrier for morphogenic processes. A recent theoretical study suggests that the CF acts as a physical barrier that promotes the directional flow of the tissue layer during GBE (Dicko et al., 2017). Because of the early

stereotypical spatial and temporal development of the CF, it is a prime candidate for acting as a barrier for other morphological events that occur during later part of *Drosophila* gastrulation. While this has yet to be confirmed experimentally, using laser ablation or optogenetics to perturb CF formation, it would be possible to examine the progression of the GBE and the outcome of embryonic development.

In conclusion, my work has addressed a long outstanding question concerning not only the CF, but tissue morphogenesis as a whole. From my data, I have shown that spatial precision of morphological events is not as simple as previously thought. Morphogenetic precision, in the context of the CF is not derived strictly from the spatial pattern laid out by the genetic patterning of the embryo. Proper morphogenetic precision of the CF relies additionally on the presence of mechanical denoising system. Through this denoising system, the initiating events self-organize to ensure morphological precision despite variability in behaviors between individual initiating cells. By having a denoising mechanism in place, the embryo can ensure that the CF forms in a robust and consistent manner, irrespective of genetic and morphological noise.

References

Aliee, M., Röper, J.-C., Landsberg, K.P., Pentzold, C., Widmann, T.J., Jülicher, F., and Dahmann, C. (2012). Physical mechanisms shaping the Drosophila dorsoventral compartment boundary. Curr. Biol. *22*, 967–976.

Allena, R., and Aubry, D. (2012). An extensive numerical simulation of the cephalic furrow formation in Drosophila embryo. Comput Methods Biomech Biomed Engin *15*, 445–455.

Ambrosini, A., Rayer, M., Monier, B., and Suzanne, M. (2019). Mechanical Function of the Nucleus in Force Generation during Epithelial Morphogenesis. Dev. Cell *50*, 197-211.e5.

Badouel, C., and McNeill, H. (2009). Apical junctions and growth control in Drosophila. Biochim. Biophys. Acta *1788*, 755–760.

Banerji, J., Rusconi, S., and Schaffner, W. (1981). Expression of a beta-globin gene is enhanced by remote SV40 DNA sequences. Cell *27*, 299–308.

Bate, M., and Arias, A.M. (1993). The Development of Drosophila Melanogaster (Cold Spring Harbor Laboratory Press).

Baumgartner, S., and Noll, M. (1990). Network of interactions among pair-rule genes regulating paired expression during primordial segmentation of Drosophila. Mech. Dev. *33*, 1–18.

Bentovim, L., Harden, T.T., and DePace, A.H. (2017). Transcriptional precision and accuracy in development: from measurements to models and mechanisms. Development *144*, 3855–3866.

Bertet, C., Sulak, L., and Lecuit, T. (2004). Myosin-dependent junction remodelling controls planar cell intercalation and axis elongation. Nature *429*, 667–671.

Blankenship, J.T., and Wieschaus, E. (2001). Two new roles for the Drosophila AP patterning system in early morphogenesis. Development *128*, 5129–5138.

Bothma, J.P., Norstad, M.R., Alamos, S., and Garcia, H.G. (2018). LlamaTags: A Versatile Tool to Image Transcription Factor Dynamics in Live Embryos. Cell *173*, 1810-1822.e16.

Buckley, C.D., Tan, J., Anderson, K.L., Hanein, D., Volkmann, N., Weis, W.I., Nelson, W.J., and Dunn, A.R. (2014). Cell adhesion. The minimal cadherin-catenin complex binds to actin filaments under force. Science *346*, 1254211.

Campos-Ortega, J.A., and Hartenstein, V. (1997). The Embryonic Development of Drosophila Melanogaster (Springer, Berlin, Heidelberg, New York).

Chu, Y., and Corey, D.R. (2012). RNA Sequencing: Platform Selection, Experimental Design, and Data Interpretation. Nucleic Acid Ther *22*, 271–274.

Clark, E. (2017). Dynamic patterning by the Drosophila pair-rule network reconciles long-germ and short-germ segmentation. PLoS Biol. *15*, e2002439.

Combs, P.A., and Eisen, M.B. (2013). Sequencing mRNA from cryo-sliced Drosophila embryos to determine genome-wide spatial patterns of gene expression. PloS One *8*, e71820.

Conte, V., Muñoz, J.J., Baum, B., and Miodownik, M. (2009). Robust mechanisms of ventral furrow invagination require the combination of cellular shape changes. Phys Biol *6*, 016010.

Costa, M., Sweeton, D., and Wieschaus, E. (1993). Gastrulation in Drosophila: Cellular mechanisms of morphogenetic movements. The Development of Drosophila Melanogaster. 425–465.

Davidson, L.A. (2012). No strings attached: new insights into epithelial morphogenesis. BMC Biol *10*, 105.

Dawes-Hoang, R.E., Parmar, K.M., Christiansen, A.E., Phelps, C.B., Brand, A.H., and Wieschaus, E.F. (2005). folded gastrulation, cell shape change and the control of myosin localization. Development *132*, 4165–4178.

Dicko, M., Saramito, P., Blanchard, G.B., Lye, C.M., Sanson, B., and Étienne, J. (2017). Geometry can provide long-range mechanical guidance for embryogenesis. PLoS Comput. Biol. *13*, e1005443.

Driever, W., and Nüsslein-Volhard, C. (1988a). A gradient of bicoid protein in Drosophila embryos. Cell *54*, 83–93.

Driever, W., and Nüsslein-Volhard, C. (1988b). The bicoid protein determines position in the Drosophila embryo in a concentration-dependent manner. Cell *54*, 95–104.

Eiraku, M., Takata, N., Ishibashi, H., Kawada, M., Sakakura, E., Okuda, S., Sekiguchi, K., Adachi, T., and Sasai, Y. (2011). Self-organizing optic-cup morphogenesis in three-dimensional culture. Nature *472*, 51–56.

Farquhar, M.G., and Palade, G.E. (1963). Junctional complexes in various epithelia. J. Cell Biol. *17*, 375–412.

Fernandez-Gonzalez, R., Simoes, S. de M., Röper, J.-C., Eaton, S., and Zallen, J.A. (2009). Myosin II dynamics are regulated by tension in intercalating cells. Dev. Cell *17*, 736–743.

Ferree, P.L., Deneke, V.E., and Di Talia, S. (2016). Measuring time during early embryonic development. Semin. Cell Dev. Biol. *55*, 80–88.

Foe, V.E. (1989). Mitotic domains reveal early commitment of cells in Drosophila embryos. Development *107*, 1–22.

Foe, V.E., and Alberts, B.M. (1983). Studies of nuclear and cytoplasmic behaviour during the five mitotic cycles that precede gastrulation in Drosophila embryogenesis. J. Cell. Sci. *61*, 31–70.

Fujioka, M., Jaynes, J.B., and Goto, T. (1995). Early even-skipped stripes act as morphogenetic gradients at the single cell level to establish engrailed expression. Development *121*, 4371–4382.

Gavin-Smyth, J., Wang, Y.-C., Butler, I., and Ferguson, E.L. (2013). A genetic network conferring canalization to a bistable patterning system in Drosophila. Curr. Biol. *23*, 2296–2302.

Gelbart, M.A., He, B., Martin, A.C., Thiberge, S.Y., Wieschaus, E.F., and Kaschube, M. (2012). Volume conservation principle involved in cell lengthening and nucleus movement during tissue morphogenesis. Proc. Natl. Acad. Sci. U.S.A. *109*, 19298–19303.

Gilmour, D., Rembold, M., and Leptin, M. (2017). From morphogen to morphogenesis and back. Nature *541*, 311–320.

Gregor, T., Wieschaus, E.F., McGregor, A.P., Bialek, W., and Tank, D.W. (2007a). Stability and nuclear dynamics of the bicoid morphogen gradient. Cell *130*, 141–152.

Gregor, T., Tank, D.W., Wieschaus, E.F., and Bialek, W. (2007b). Probing the limits to positional information. Cell *130*, 153–164.

Guglielmi, G., Barry, J.D., Huber, W., and De Renzis, S. (2015). An Optogenetic Method to Modulate Cell Contractility during Tissue Morphogenesis. Dev. Cell *35*, 646–660.

Gyoergy, A., Roblek, M., Ratheesh, A., Valoskova, K., Belyaeva, V., Wachner, S., Matsubayashi, Y., Sánchez-Sánchez, B.J., Stramer, B., and Siekhaus, D.E. (2018). Tools Allowing Independent Visualization and Genetic Manipulation of Drosophila melanogaster Macrophages and Surrounding Tissues. G3 (Bethesda) *8*, 845–857.

Haigo, S.L., Hildebrand, J.D., Harland, R.M., and Wallingford, J.B. (2003). Shroom induces apical constriction and is required for hingepoint formation during neural tube closure. Curr. Biol. *13*, 2125–2137.

Hallgrimsson, B., Green, R.M., Katz, D.C., Fish, J.L., Bernier, F.P., Roseman, C.C., Young, N.M., Cheverud, J.M., and Marcucio, R.S. (2019). The developmental-genetics of canalization. Semin. Cell Dev. Biol. *88*, 67–79.

Hardin, J., and Keller, R. (1988). The behaviour and function of bottle cells during gastrulation of Xenopus laevis. Development *103*, 211–230.

Hartenstein, V., and Campos-Ortega, J.A. (1985). Fate-mapping in wild-typeDrosophila melanogaster. Wilhelm Roux' Archiv *194*, 181–195.

He, B., Doubrovinski, K., Polyakov, O., and Wieschaus, E. (2014). Apical constriction drives tissue-scale hydrodynamic flow to mediate cell elongation. Nature *508*, 392–396.

Heer, N.C., and Martin, A.C. (2017). Tension, contraction and tissue morphogenesis. Development *144*, 4249–4260.

Heiman, M., Schaefer, A., Gong, S., Peterson, J.D., Day, M., Ramsey, K.E., Suárez-Fariñas, M., Schwarz, C., Stephan, D.A., Surmeier, D.J., et al. (2008). A translational profiling approach for the molecular characterization of CNS cell types. Cell *135*, 738–748.

Heiman, M., Kulicke, R., Fenster, R.J., Greengard, P., and Heintz, N. (2014). Cell type-specific mRNA purification by translating ribosome affinity purification (TRAP). Nat Protoc *9*, 1282–1291.

Henstridge, M.A., Johnson, T.K., Warr, C.G., and Whisstock, J.C. (2014). Trunk cleavage is essential for Drosophila terminal patterning and can occur independently of Torso-like. Nat Commun *5*, 3419.

Hong, J.-W., Hendrix, D.A., Papatsenko, D., and Levine, M.S. (2008). How the Dorsal gradient works: insights from postgenome technologies. Proc. Natl. Acad. Sci. U.S.A. *105*, 20072–20076.

Hong, L., Dumond, M., Tsugawa, S., Sapala, A., Routier-Kierzkowska, A.-L., Zhou, Y., Chen, C., Kiss, A., Zhu, M., Hamant, O., et al. (2016). Variable Cell Growth Yields Reproducible OrganDevelopment through Spatiotemporal Averaging. Dev. Cell *38*, 15–32.

Hutson, M.S., Tokutake, Y., Chang, M.-S., Bloor, J.W., Venakides, S., Kiehart, D.P., and Edwards, G.S. (2003). Forces for morphogenesis investigated with laser microsurgery and quantitative modeling. Science *300*, 145–149.

Izquierdo, E., Quinkler, T., and De Renzis, S. (2018). Guided morphogenesis through optogenetic activation of Rho signalling during early Drosophila embryogenesis. Nat Commun *9*, 2366.

James, K.E., Dorman, J.B., and Berg, C.A. (2002). Mosaic analyses reveal the function of Drosophila Ras in embryonic dorsoventral patterning and dorsal follicle cell morphogenesis. Development *129*, 2209–2222.

Karaiskos, N., Wahle, P., Alles, J., Boltengagen, A., Ayoub, S., Kipar, C., Kocks, C., Rajewsky, N., and Zinzen, R.P. (2017). The Drosophila embryo at single-cell transcriptome resolution. Science *358*, 194–199.

Kondo, T., and Hayashi, S. (2013). Mitotic cell rounding accelerates epithelial invagination. Nature *494*, 125–129.

Kong, D., Wolf, F., and Großhans, J. (2017). Forces directing germ-band extension in Drosophila embryos. Mechanisms of Development *144*, 11–22.

Kosman, D., and Small, S. (1997). Concentration-dependent patterning by an ectopic expression domain of the Drosophila gap gene knirps. Development *124*, 1343–1354.

Krakauer, D.C., and Plotkin, J.B. (2002). Redundancy, antiredundancy, and the robustness of genomes. Proc. Natl. Acad. Sci. U.S.A. *99*, 1405–1409.

Kratz, A., Beguin, P., Kaneko, M., Chimura, T., Suzuki, A.M., Matsunaga, A., Kato, S., Bertin, N., Lassmann, T., Vigot, R., et al. (2014). Digital expression profiling of the compartmentalized translatome of Purkinje neurons. Genome Res. *24*, 1396–1410.

Krueger, D., Tardivo, P., Nguyen, C., and De Renzis, S. (2018). Downregulation of basal myosin-II is required for cell shape changes and tissue invagination. EMBO J. *37*.

Kugler, J.-M., and Lasko, P. (2009). Localization, anchoring and translational control of oskar, gurken, bicoid and nanos mRNA during Drosophila oogenesis. Fly (Austin) *3*, 15–28.

Lagha, M., Bothma, J.P., and Levine, M. (2012). Mechanisms of transcriptional precision in animal development. Trends Genet. *28*, 409–416.

Larue, L., Ohsugi, M., Hirchenhain, J., and Kemler, R. (1994). E-cadherin null mutant embryos fail to form a trophectoderm epithelium. Proc. Natl. Acad. Sci. U.S.A. *91*, 8263–8267.

Lecuit, T., and Wieschaus, E. (2000). Polarized insertion of new membrane from a cytoplasmic reservoir during cleavage of the Drosophila embryo. J. Cell Biol. *150*, 849–860.

Lecuit, T., and Yap, A.S. (2015). E-cadherin junctions as active mechanical integrators in tissue dynamics. Nat. Cell Biol. *17*, 533–539.

Lee, J.-Y., and Harland, R.M. (2007). Actomyosin contractility and microtubules drive apical constriction in Xenopus bottle cells. Dev. Biol. *311*, 40–52.

Leptin, M. (1995). Drosophila gastrulation: from pattern formation to morphogenesis. Annu. Rev. Cell Dev. Biol. *11*, 189–212.

Levayer, R., and Lecuit, T. (2012). Biomechanical regulation of contractility: spatial control and dynamics. Trends Cell Biol. *22*, 61–81.

Li, X., MacArthur, S., Bourgon, R., Nix, D., Pollard, D.A., Iyer, V.N., Hechmer, A., Simirenko, L., Stapleton, M., Hendriks, C.L.L., et al. (2008). Transcription Factors Bind Thousands of Active and Inactive Regions in the Drosophila Blastoderm. PLoS Biol *6*.

Li, Y.-F., Zheng, Y., Vemireddy, L.R., Panda, S.K., Jose, S., Ranjan, A., Panda, P., Govindan, G., Cui, J., Wei, K., et al. (2018). Comparative transcriptome and translatome analysis in contrasting rice genotypes reveals differential mRNA translation in salt-tolerant Pokkali under salt stress. BMC Genomics *19*, 935.

Little, S.C., Tikhonov, M., and Gregor, T. (2013). Precise developmental gene expression arises from globally stochastic transcriptional activity. Cell *154*, 789–800.

Liu, F., Morrison, A.H., and Gregor, T. (2013). Dynamic interpretation of maternal inputs by the Drosophila segmentation gene network. Proc. Natl. Acad. Sci. U.S.A. *110*, 6724–6729.

Lott, S.E., Kreitman, M., Palsson, A., Alekseeva, E., and Ludwig, M.Z. (2007). Canalization of segmentation and its evolution in Drosophila. Proc. Natl. Acad. Sci. U.S.A. *104*, 10926–10931.

Lye, C.M., Blanchard, G.B., Naylor, H.W., Muresan, L., Huisken, J., Adams, R.J., and Sanson, B. (2015). Mechanical Coupling between Endoderm Invagination and Axis Extension in Drosophila. PLoS Biol. *13*, e1002292.

Mammoto, A., Mammoto, T., and Ingber, D.E. (2012). Mechanosensitive mechanisms in transcriptional regulation. J. Cell. Sci. *125*, 3061–3073.

Manu, null, Surkova, S., Spirov, A.V., Gursky, V.V., Janssens, H., Kim, A.-R., Radulescu, O., Vanario-Alonso, C.E., Sharp, D.H., Samsonova, M., et al. (2009). Canalization of gene expression and domain shifts in the Drosophila blastoderm by dynamical attractors. PLoS Comput. Biol. *5*, e1000303.

Martin, A.C., and Goldstein, B. (2014). Apical constriction: themes and variations on a cellular mechanism driving morphogenesis. Development *141*, 1987–1998.

Martin, A.C., Gelbart, M., Fernandez-Gonzalez, R., Kaschube, M., and Wieschaus, E.F. (2010). Integration of contractile forces during tissue invagination. J. Cell Biol. *188*, 735–749.

Mason, F.M., Tworoger, M., and Martin, A.C. (2013). Apical domain polarization localizes actin-myosin activity to drive ratchet-like apical constriction. Nat. Cell Biol. *15*, 926–936.

Matsumura, F. (2005). Regulation of myosin II during cytokinesis in higher eukaryotes. Trends Cell Biol. *15*, 371–377.

Munjal, A., and Lecuit, T. (2014). Actomyosin networks and tissue morphogenesis. Development *141*, 1789–1793.

Munjal, A., Philippe, J.-M., Munro, E., and Lecuit, T. (2015). A self-organized biomechanical network drives shape changes during tissue morphogenesis. Nature *524*, 351–355.

Nishimura, M., Inoue, Y., and Hayashi, S. (2007). A wave of EGFR signaling determines cell alignment and intercalation in the Drosophila tracheal placode. Development *134*, 4273–4282.

Nishimura, T., Honda, H., and Takeichi, M. (2012). Planar cell polarity links axes of spatial dynamics in neural-tube closure. Cell *149*, 1084–1097.

Nüsslein-Volhard, C. (1991). Determination of the embryonic axes of Drosophila. Dev. Suppl. *1*, 1–10.

Oda, H., Uemura, T., Harada, Y., Iwai, Y., and Takeichi, M. (1994). A Drosophila homolog of cadherin associated with armadillo and essential for embryonic cell-cell adhesion. Dev. Biol. *165*, 716–726.

Panousopoulou, E., and Green, J.B.A. (2016). Invagination of Ectodermal Placodes Is Driven by Cell Intercalation-Mediated Contraction of the Suprabasal Tissue Canopy. PLoS Biol. *14*, e1002405.

Pearl, E.J., Li, J., and Green, J.B.A. (2017). Cellular systems for epithelial invagination. Philos. Trans. R. Soc. Lond., B, Biol. Sci. *372*.

Peralta, X.G., Toyama, Y., Hutson, M.S., Montague, R., Venakides, S., Kiehart, D.P., and Edwards, G.S. (2007). Upregulation of forces and morphogenic asymmetries in dorsal closure during Drosophila development. Biophys. J. *92*, 2583–2596.

Pettersen, E.F., Goddard, T.D., Huang, C.C., Couch, G.S., Greenblatt, D.M., Meng, E.C., and Ferrin, T.E. (2004). UCSF Chimera--a visualization system for exploratory research and analysis. J Comput Chem *25*, 1605–1612.

Pispa, J., and Thesleff, I. (2003). Mechanisms of ectodermal organogenesis. Dev. Biol. *262*, 195–205.

Porter, J.R., Telford, W.G., and Batchelor, E. (2017). Single-cell Gene Expression Profiling Using FACS and qPCR with Internal Standards. J Vis Exp.

Reuter, R., Grunewald, B., and Leptin, M. (1993). A role for the mesoderm in endodermal migration and morphogenesis in Drosophila. Development *119*, 1135–1145.

Roper, K. (2012). Anisotropy of Crumbs and aPKC drives myosin cable assembly during tube formation. Developmental Cell *23*, 939–953.

Rünneburger, E., and Le Rouzic, A. (2016). Why and how genetic canalization evolves in gene regulatory networks. BMC Evol. Biol. *16*, 239.

Sackerson, C., Fujioka, M., and Goto, T. (1999). The even-skipped locus is contained in a 16-kb chromatin domain. Dev. Biol. *211*, 39–52.

Sanchez-Corrales, Y.E., Blanchard, G.B., and Röper, K. (2018). Radially patterned cell behaviours during tube budding from an epithelium. Elife *7*.

Sandler, J.E., and Stathopoulos, A. (2016). Quantitative Single-Embryo Profile of Drosophila Genome Activation and the Dorsal-Ventral Patterning Network. Genetics *202*, 1575–1584.

Sanson, B. (2001). Generating patterns from fields of cells. Examples from Drosophila segmentation. EMBO Rep. *2*, 1083–1088.

dos Santos, G., Schroeder, A.J., Goodman, J.L., Strelets, V.B., Crosby, M.A., Thurmond, J., Emmert, D.B., Gelbart, W.M., and FlyBase Consortium (2015). FlyBase: introduction of the Drosophila melanogaster Release 6 reference genome assembly and large-scale migration of genome annotations. Nucleic Acids Res. *43*, D690-697.

Sauer, F., Rivera-Pomar, R., Hoch, M., and Jäckle, H. (1996). Gene regulation in the Drosophila embryo. Philos. Trans. R. Soc. Lond., B, Biol. Sci. *351*, 579–587.

Sawyer, J.M., Harrell, J.R., Shemer, G., Sullivan-Brown, J., Roh-Johnson, M., and Goldstein, B. (2010). Apical constriction: a cell shape change that can drive morphogenesis. Dev. Biol. *341*, 5–19.

Schüpbach, T., and Roth, S. (1994). Dorsoventral patterning in Drosophila oogenesis. Curr. Opin. Genet. Dev. *4*, 502–507.

Sherrard, K., Robin, F., Lemaire, P., and Munro, E. (2010). Sequential activation of apical and basolateral contractility drives ascidian endoderm invagination. Curr. Biol. *20*, 1499–1510.

Shyer, A.E., Tallinen, T., Nerurkar, N.L., Wei, Z., Gil, E.S., Kaplan, D.L., Tabin, C.J., and Mahadevan, L. (2013). Villification: how the gut gets its villi. Science *342*, 212–218.

Sobek, J., Bartscherer, K., Jacob, A., Hoheisel, J.D., and Angenendt, P. (2006). Microarray technology as a universal tool for high-throughput analysis of biological systems. Comb. Chem. High Throughput Screen. *9*, 365–380.

Spencer, A.K., Siddiqui, B.A., and Thomas, J.H. (2015). Cell shape change and invagination of the cephalic furrow involves reorganization of F-actin. Dev. Biol. *402*, 192–207.

Squire, J.M., Paul, D.M., and Morris, E.P. (2017). Myosin and Actin Filaments in Muscle: Structures and Interactions. Subcell. Biochem. *82*, 319–371.

St Johnston, D., and Nüsslein-Volhard, C. (1992). The origin of pattern and polarity in the Drosophila embryo. Cell *68*, 201–219.

Struhl, G., Fitzgerald, K., and Greenwald, I. (1993). Intrinsic activity of the Lin-12 and Notch intracellular domains in vivo. Cell *74*, 331–345.

Sui, L., Alt, S., Weigert, M., Dye, N., Eaton, S., Jug, F., Myers, E.W., Jülicher, F., Salbreux, G., and Dahmann, C. (2018). Differential lateral and basal tension drive folding of Drosophila wing discs through two distinct mechanisms. Nat Commun *9*, 4620.

Sung, H., Spangenberg, S., Vogt, N., and Großhans, J. (2013). Number of nuclear divisions in the Drosophila blastoderm controlled by onset of zygotic transcription. Curr. Biol. *23*, 133–138.

Sweeton, D., Parks, S., Costa, M., and Wieschaus, E. (1991). Gastrulation in Drosophila: the formation of the ventral furrow and posterior midgut invaginations. Development *112*, 775–789.

Tada, M., and Heisenberg, C.-P. (2012). Convergent extension: using collective cell migration and cell intercalation to shape embryos. Development *139*, 3897–3904.

Takeda, M., Sami, M.M., and Wang, Y.-C. (2018). A homeostatic apical microtubule network shortens cells for epithelial folding via a basal polarity shift. Nat. Cell Biol. *20*, 36–45.

Theodosiou, N.A., and Xu, T. (1998). Use of FLP/FRT system to study Drosophila development. Methods *14*, 355–365.

Thomas, A., Lee, P.-J., Dalton, J.E., Nomie, K.J., Stoica, L., Costa-Mattioli, M., Chang, P., Nuzhdin, S., Arbeitman, M.N., and Dierick, H.A. (2012). A versatile method for cell-specific profiling of translated mRNAs in Drosophila. PLoS ONE *7*, e40276.

Vale, R.D., and Milligan, R.A. (2000). The way things move: looking under the hood of molecular motor proteins. Science *288*, 88–95.

Vasquez, C.G., and Martin, A.C. (2016). Force transmission in epithelial tissues. Dev. Dyn. *245*, 361–371.

Vavra, S.H., and Carroll, S.B. (1989). The zygotic control of Drosophila pair-rule gene expression. I. A search for new pair-rule regulatory loci. Development *107*, 663–672.

Vincent, A., Blankenship, J.T., and Wieschaus, E. (1997). Integration of the head and trunk segmentation systems controls cephalic furrow formation in Drosophila. Development *124*, 3747–3754.

Waddington, C.H. (1957). The strategy of the genes: a discussion of some aspects of theoretical biology (Allen & Unwin).

Wagner, D.E., Weinreb, C., Collins, Z.M., Briggs, J.A., Megason, S.G., and Klein, A.M. (2018). Single-cell mapping of gene expression landscapes and lineage in the zebrafish embryo. Science *360*, 981–987.

Wang, Y.-C., Khan, Z., Kaschube, M., and Wieschaus, E.F. (2012). Differential positioning of adherens junctions is associated with initiation of epithelial folding. Nature *484*, 390–393.

Wang, Y.-C., Khan, Z., and Wieschaus, E.F. (2013). Distinct Rap1 activity states control the extent of epithelial invagination via α-catenin. Dev. Cell *25*, 299–309.

Weigel, D., Jürgens, G., Klingler, M., and Jäckle, H. (1990). Two gap genes mediate maternal terminal pattern information in Drosophila. Science *248*, 495–498.

Wen, F.-L., Wang, Y.-C., and Shibata, T. (2017). Epithelial Folding Driven by Apical or Basal-Lateral Modulation: Geometric Features, Mechanical Inference, and Boundary Effects. Biophys. J. *112*, 2683–2695.

Weng, M., and Wieschaus, E. (2016). Myosin-dependent remodeling of adherens junctions protects junctions from Snail-dependent disassembly. J. Cell Biol. *212*, 219–229.

Wimmer, E.A., Simpson-Brose, M., Cohen, S.M., Desplan, C., and Jäckle, H. (1995). Trans- and cis-acting requirements for blastodermal expression of the head gap gene buttonhead. Mech. Dev. *53*, 235–245.

Wimmer, E.A., Cohen, S.M., Jackle, H., and Desplan, C. (1997). buttonhead does not contribute to a combinatorial code proposed for Drosophila head. Development *124*, 1509–1517.

Xiong, F., Tentner, A.R., Huang, P., Gelas, A., Mosaliganti, K.R., Souhait, L., Rannou, N., Swinburne, I.A., Obholzer, N.D., Cowgill, P.D., et al. (2013). Specified neural progenitors sort to form sharp domains after noisy Shh signaling. Cell *153*, 550–561.

Yao, M., Qiu, W., Liu, R., Efremov, A.K., Cong, P., Seddiki, R., Payre, M., Lim, C.T., Ladoux, B., Mège, R.-M., et al. (2014). Force-dependent conformational switch of α-catenin controls vinculin binding. Nat Commun *5*, 4525.

Yevick, H.G., Miller, P.W., Dunkel, J., and Martin, A.C. (2019). Structural Redundancy in Supracellular Actomyosin Networks Enables Robust Tissue Folding. Dev. Cell *50*, 586-598.e3.

Yonemura, S. (2011). Cadherin-actin interactions at adherens junctions. Curr. Opin. Cell Biol. *23*, 515–522.

Yonemura, S., Wada, Y., Watanabe, T., Nagafuchi, A., and Shibata, M. (2010). alpha-Catenin as a tension transducer that induces adherens junction development. Nat. Cell Biol. *12*, 533–542.

Zallen, J.A., and Wieschaus, E. (2004). Patterned gene expression directs bipolar planar polarity in Drosophila. Developmental Cell *6*, 343–355.

Acknowledgements

I would like to thank my advisors, Dr. Yu-Chiun Wang and Dr. Shigeo Hayashi for their support, and guidance in making this thesis possible. I cannot express enough how honored I am for being giving the opportunity to have studied under Dr. Wang and for his outstanding patience, understanding, and honest with me throughout my doctoral training. I may have been difficult to work with at times, but he was there for me at every step of this project, and for that I am eternally grateful. Without the assistance and guidance from Dr. Hayashi, I would not have been able to attend Kobe University and to achieve my life goal of earning a PhD. I am deeply honored to have the opportunity to work under both Dr. Wang and Dr. Hayashi. Through their tutelage, I have greatly expanded my knowledge of developmental biology and learned what it means to be an outstanding and productive scientist. Without their support, I would not be where I am today or have the opportunity to advance my scientific career.

I also wish to extend my deepest thanks to the members of my committee; Dr. Kunio Inoue, and Dr. Yuji Kageyama at Kobe University and Dr. Mitsuru Morimoto at RIKEN Center for Biosystems Dynamics Research (BDR), for taking the time to provide critical feedback that guided my project. Additionally, I would like to thank Dr. Shigeru Kuratani for guidance and philosophical discussion on developmental biology.

Parts of this thesis and the submitted manuscript would not have been possible without the help of all my co-authors and collaborators. I wish to especially thank Dr. Claire Bromley, Dr. Antonio Bolea Albero, Dr. Michiko Takeda for their skills and contributions to this project. I would also like to thank my collaborators Dr. Lucas Schütz and Dr. Steffen Lemke for generously providing the *in toto* SPIM data; Dr. Fu-Lai Wen and Dr. Tatsuo Shibata for the remarkable skills in computational simulation; and Dr. Takashi Fukaya for the generously providing the Eve-Llama flies. Additionally, I would like to thank Dr. Eric Wieschaus and Dr. Bing He for providing the

optogenetic flies. I also want to extend my gratitude to the members of the Wang and Hayashi labs for their critical feedback and support, as well as all the fly labs at RIKEN BDR.

I am also indebted to Kobe University, RIKEN Center for Biosystems Dynamics Research (BDR) and the generous funding through the RIKEN International Program Associate (IPA) fellowship for giving me the opportunity to earn my PhD, progress my scientific career, and provide me with countless opportunities. I wish to thank all members of the RIKEN support staff to helping me acclimate to living in Japan. I wish to extend a special thanks to Mrs. Yuko Fujiyama for helping me navigate the process and assembly of my thesis.

I would like to thank the agencies that have graciously provided financial support for this project. Specifically, the RIKEN IPA fellowship, the core funding through RIKEN, Japan Society for the Promotion of Science (JSPS) Grant-in-Aid grant to Dr. Yu-Chiun Wang and Dr. Takashi Fukaya, and the Human Frontier Scientific Program Young Investigators Grant to Dr. Yu-Chiun Wang and Dr. Steffen Lemke. This project would not have been possible without their gracious support.

Lastly, I would like to thank my family and friends for their emotional support and understanding, especially my mother, father, step-mother, and sister. It has been their constant encouragement and unconditional love that has kept me going throughout out my struggles. To my friends, Brittany Johnson and Matilde Miranda for providing much needed sanity boosts and a venue to vent my frustrations, I am indebted.

Figure legends

Main figures legends

Figure 1.1: Introduction figures

(A and B) Schematic representations of the genetic hierarchy that patterns the A-P and D-V axis of *Drosophila* embryo. (A) Diagram of the hierarchy of genes that establishes the A-P axis, including the maternal genes deposited during oogenesis and the further establishment of gap genes and pair-rule gene expression. Adapted from (Sanson, 2001). (B) Diagram of the genetic interactions that establishes the D-V axis within the ovary and the developing embryo. Adapted from (James et al., 2002).

(C) Invagination of the ventral furrow (VF). Developing Drosophila embryo stained with phalloidin to visualize the actin meshwork that outlines the cells. Cells along the ventral surface undergo apical constriction which leads to the invagination of the VF. Adapted from (Conte et al., 2009).

(D) Invagination of the posterior midgut (PMG). Scanning electron micrographs of the lateral surface of the developing *Drosophila* embryo during gastrulation (Stages 6-8) (dos Santos et al., 2015). Posterior midgut invagination (PMI) occurs on the dorsal surface through apical constriction which leads to the invagination of the pole cells (PC). The invagination of the PMG also applies a pulling force and drives the extension of the germband posteriorly (blue overlay and yellow arrow). Adapted from (Lye et al., 2015)

Figure 1.2: Introduction figures cont.

(A) MyoII mediated apical constriction during VF formation. MyoII accumulation at the medio-apical surface of the cell and leads to the contraction and stabilization of the apical surface. This

leads to the deformation of the apical surface and allows for the invagination of the VF initiating cells. Adapted from (Mason et al., 2013).

(B) Lateral constriction of cell interfaces in ascidian embryos. Magenta arrows indicate the apicobasal shortening of the mesectoderm cells the drives the invagination of the endoderm during gastrulation (Sherrard et al., 2010).

(C) Apical constriction independent mechanism of cell shape change. Two-photon imaging of E-cadherin-GFP (junctions) and Resille-GFP (membrane) in the posterior dorsal fold during dorsal fold formation. Individual cells are outlined in green based on Resille-GFP signal and junctions are circled in red based on E-cadherin signal. Adapted from (Wang et al., 2012).

(D) Tissue-scale planar polarization of MyoII and Bazooka/Par3 (junctional markers) during germband extension (GBE) in the *Drosophila* embryo. MyoII becomes planar polarized along the A-P segmental boundaries while Bazooka/Par3 become planar polarized perpendicular to MyoII. This leads to multiple junctions with D-V orientation (red line) to form a rosette structure that resolves by extension with the expansion along the A-P orientation (blue line). Adapted from (Kong et al., 2017).

Figure 2: CF initiation is temporally heterogeneous with two distinct initiation types

(A) Lateral *en face* projection (top) and coronal section (bottom) of a MyoII-GFP embryo during development. The annotated orientations were used in all figures unless otherwise noted. Arrowheads: orange, CF; magenta, VF; green, dorsal edge of posterior midgut. Arrows: cyan, MD2; yellow, MD6. Scale bar, 50 μm.

(B) Type I (n = 4/9) and type II (n = 5/9) initiation events shown as coronal images of Gap43-mCherry. t = 0 defined as the end of cellularization. The initiating cells are shaded in blue;

neighboring cells in red at t = 0. Colored circles label interfaces (-1), (0), (+1) and (+3) quantified in (D). Scale bars, 10 μm.

(C) Coronal images of fixed wild-type embryos stained with neurotactin (membrane) illustrating the initiation behaviors (top) and their corresponding schematic diagrams (bottom). Type II initiating events can be further categorized into the asymmetric and symmetric subtypes, based on the synchronicity of cell shortening in the two initiating cells. In the images, initiating cells are masked in blue and neighboring cells are masked in red. Colored circles mark the indexed lateral interfaces (-1), (0), (+1), and (+3). In the diagrams, blue shading denotes initiating cells; red shading denotes neighboring cells; P(0) is defined as in Figure 2 and the associated description in the Results; A, type II anterior initiating cell; P, type II posterior initiating cell. Scale bar, 10 μm.

(D) Total lengths and tortuosity of interfaces (-1), (0), (+1) and (+3) as a function of time during type I (top) and type II (bottom) initiation. t = 0 defined as the end of cellularization. High tortuosity indicates low straightness. Trend lines are a second degree polynomial fit.

(E and F) Boxplots of initiation event frequencies. Initiation events were identified in embryos expressing MyoII-GFP and Gap43-mCherry in the lateral-most region containing 9 ± 2 initiating events (Mean ± SD; n = 10 embryos). (E) Per embryo frequencies of the two initiation types with gray lines connecting frequency observations made in the same embryo. (F) D-V distribution of each type of initiation event with D-V position denoted as the center of each bin.

See also Movies S1, S2, S3.

Figure 3: The CF genetic network generates positional information with single cell-row resolution that accounts for 80% of initiating events

(A) Immunofluorescence *en-face* lateral sum projection of a fixed wild-type embryo labeled with Btd (green), Eve (red) and DAPI (blue). The yellow rectangle denotes the cropped area shown in (B-E). Scale bar, 50 μm.

(B-E) Btd and Eve expression centered on the Eve1 region shown as the *en face* sum projection of a cropped lateral region in wild-type (B), *btd* (C), *eve* (D), and *runt* (E) mutant embryos (Btd, green; Eve, red; DAPI, blue). The corresponding bar graphs display the distribution of average Btd and Eve nuclear concentration of a single D-V cell row along the A-P axis in 5 μm bins (wild-type, n = 1427 cells from 13 embryos; *btd,* n = 838 cells from 8 embryos; *eve*, n = 527 cells from 3 embryos; *runt*, n = 1856 from 11 embryos). This analysis defines the positional indexes, e.g. P(0), of cells, as annotated in (B). Scale bars, 10 μm.

(F) Eve and Runt inhibit Btd. Coronal images of wild-type (top), maternal Gal4 driving *UAS-eve* (middle, *matGal4>eve*) and maternal Gal4 driving *UAS-runt* (bottom, *matGal4>runt*) embryos displaying Neurotactin (membrane, gray), Btd (green) and Eve (red) immunofluorescence in full embryo (left) and close-up (right, from the region highlighted in yellow rectangles on the left) views. Embryos are staged based on posterior midgut morphology. *matGal4>runt* embryos often show reduced cell height. Scale bars, 10 μm.

(G and H) (G)Type III initiation in the *runt* mutant shown in a coronal images of Neurotactin (membrane) immunofluorescence. The initiating cells are shaded in blue; neighboring cells in red. Scale bar, 10 μm. (H) Boxplot of the number of initiating cells within 61.6 μm span along the DV axis in wild-type (n = 10 embryos) and *runt* (n = 5 embryos) mutant embryos. ***, $p < 0.001$.

(I) Schematics and statistics showing percentage match of type I and type II anterior cell to the P(0) position as defined in (B).

(J) Bar graphs of Btd and Eve levels comparing between the initiating and all cells. Cell positions defined as in (B). *, $p < 0.05$; ***, $p < 0.001$; n.s., not significant.

(K) Frequency distribution of Eve expression levels in the initiating cells showing increased frequency of low Eve expressing cells below the cutoff of 0.3 (purple dashed line) in *runt* mutants (13.2%, n = 30/228 initiating cells in 13 embryos), compared with wild-type (0.7%, n = 1/128 initiating cells in 13 embryos).

(L and M) Analysis of P(0) and CF alignment. (L) Boxplot for the RMSE of P(0) and cleft positions to their respective linear fits (blue and orange), and the RMSE of cleft positions to the P(0) linear fit (green). (K) Correlation analysis between the RMSE values and the per embryo P(0) percentage match. P(0) position defined as in (B); cleft positions defined as the centroid of the type I cell or the midpoint between centroids of the type II cell pair. Purple dashed line in (L) denotes the theoretical RMSE lower bound (0.4 cell diameter) with 20% mismatch to P(0) position (1 cell diameter estimated as 5 μm). ρ, Spearman rank-order correlation coefficient. n = 13 embryos.

See also Movies S3, S4.

Figure 4: Genetic perturbation of the CF region

(A) X-y scatter plots of a representative wild-type embryo centered on the Eve1 region displaying for the Eve intensities and the processing steps for top Eve expressing cell identification, registration and initiating cell mapping. Identification of the top Eve expressing cell in each D-V position (left plot) was carried out in three steps as detailed in Methods. The top Eve cells were then used to define a new set of 5 μm bins within which cell positions were re-aligned to the top Eve cell (center plot). The realigned cell positions were used to generate the bar graph in Figure 2B. For mapping of initiating cells to the gene coordinate (right plot), the

P(0) positions were defined as (phase 1 positive) ∨ (phase 2 positive) cells (∨, the Boolean “or” operation). The type I and type II initiating cells were labeled with light blue and orange circles, respectively. Initiating cells that match/mismatch P(0) position were further annotated with green dotted circles and pink dotted circles, respectively.

(B) Single z plane from an *en face* imaging stack (large left panel) of a fixed wild-type embryo stained with neurotactin (membrane, green) and DAPI (nuclei, magenta) with the Imaris re-slices (small right panels) for initiating type identification. The image on the left corresponds to the one used in (A) for the illustration of processing steps. In the left panel, type I and type II initiating cells are marked with light blue and orange circles, respectively, and numbered to correspond to the numbered right panels that show the Imaris re-slices. Yellow dashed lines (left) approximate the re-slicing planes. Scale bars,10 μm.

(C-E) Lateral *en-face* standard deviation projections of fixed, late cellularization embryos just prior to the formation of the CF cleft. Non-uniform DAPI expression is an experimental artifact of mosaic stitching. (C) Fixed wild-type, btd^{AX}, eve^{R13}, and $runt^{B5}$ embryos stained with Eve (red), Btd (green), and DAPI (blue). (D) Fixed embryo with Eve overexpression driven maternally (*matGal4>eve*), Runt overexpression driven maternally (*matGal4>runt*), or Btd overexpression driven by *nos-GAL4-GCN4-bcd3'UTR* (*Gal4-bcd3’UTR>btd*) stained with Eve (red), Btd (green), and DAPI (blue). (E) Wild-type, $runt^{B5}$ and Runt overexpression (*matGal4>runt*) embryos stained with Runt (red), Btd (green), and DAPI (blue). Scale bars, 50 μm.

(F) Schematic representation of the genetic network that specifies the CF. The network generates single cell row positional information depicted as P(-1), P(0), P(+1), and P(+2).

(G) Boxplots illustrating the per embryo frequency of initiation events in $runt^{B5}$ (top, n = 13 embryos) and *Gal4-bcd 3’UTR>btd* (bottom, n = 8 embryos).

(H and I) Immunofluorescence *en-face* lateral sum projection of a fixed *α-Cat* RNAi embryo labeled with Btd (green), Eve (red) and DAPI (blue) shown in a whole embryo view (H) and a high magnification view (I) centered on the Eve1 region. The yellow rectangle in (H) denotes the cropped area shown in (I). Scale bars, 50 μm in (H) and 10 μm in (I).

Figure 5: Interface shortening is associated with lateral myosin contractility

(A) Coronal images of a MyoII-GFP embryo undergoing type II initiation showing transient accumulation of MyoII foci (from Movie S2, bottom). t = 0 defined as the end of cellularization. Colored circles, indexed lateral interfaces; yellow arrows, MyoII foci at lateral interfaces; dotted white line, CF cleft. Scale bar, 10 μm.

(B) Mean pixel intensity of lateral MyoII foci as a function of time measured from Movie S2. t = 0 defined as the end of cellularization.

(C) Coronal images of an embryo expressing MyoII-mKate2 and α-Cat-Venus (junction) showing junctional (cyan arrow) and basal-lateral (yellow arrow) MyoII foci. t = 0 defined as the end of cellularization. Scale bar, 10 μm.

(D) Estimated total, apical and lateral lengths of interface (0) as a function of time. The lengths are normalized by the total length of the control interface (n = 5 embryos).

Figure 6: MyoII planar polarization is associated with the straightening of interface (0)

(A and B) Planar polarization of MyoII and interface straightening. (A) *En face* sum projection of Gap43-mCherry (membrane) and MyoII-GFP in the CF region (left), compared to the lack of MyoII accumulation in the GB region (right). Colored circles index lateral interfaces as in Figure 2B. (B) Time-lapse series of skeletonized Gap43-mCherry during CF initiation denoting the straightening of interfaces in the CF region (cyan segmented line), relative to control interfaces

in the head region (magenta segmented line). Depth of z projection, 5-8 μm from the embryo surface.

(C) Sum projection of MyoII-mKate2 imaged *en face* in a wild-type or *eve* mutant embryo, comparing the CF and GB regions. 14 minutes prior to MD6 onset is the estimated normal timing of CF cleft formation in the wild-type. Depth of z projection, 0-9.5 μm from the embryo surface.

(D) MyoII-mKate2 normalized mean pixel intensities and polarization as a function of time in wild-type (n = 4) or *eve* mutants (n = 4) embryos, comparing the CF and GB regions. Gray shading observed timing of CF cleft formation in wild-type. Quantitation of MyoII intensities in the CF region was terminated at -14 min, as CF cell internalization rendered quantitation unreliable. t = 0 defined as MD6 onset. Error bands, SD. The trend lines are a second-degree polynomial fit.

(E) Lateral *en-face* time-lapse series of skeletonized Gap43-mCherry (membrane) in btd^{AX}, eve^{R13}, and $runt^{B5}$ embryos. Selected time points are shown. Cyan line, a representative "ribbon" in the pre-CF domain. Magenta line, a control interface "ribbon" in the head region. Yellow arrowhead indicates an additional straightening "ribbon" in $runt^{B5}$ embryo. Scale bars, 10 μm.

(F) CF cleft depth as a function of time in wild-type (n = 6) and *btd* mutant (n = 7) embryos. Error bands, SD. t = 0 defined as the end of cellularization.

Figure 7: Effect of patterning disruption on CF initiation and invagination

(A) Time-lapse coronal images of the CF region in wild-type, btd^{AX}, $runt^{B5}$, *α-Cat* RNAi embryos expressing Gap43-mCherry (membrane, green) and MyoII-GFP (magenta). Yellow asterisks, initiating cells; red asterisks, neighboring cells. t = 0 defined as the end of cellularization. Scale bars, 10 μm.

(B) Time-lapse coronal images (upper and middle rows) of the CF region in two *btd*^{AX} embryos expressing Gap43-mCherry (membrane, green) and MyoII-GFP (magenta). One embryo is shown in each column. The pre-CF region was defined by the size of yolk stocks taken from an *en face* image of the cellularization front during mid-cellularization (yellow masks, lower row) and marked by dashed yellow lines. Cyan line in the lower row marks the plane used to generate the coronal line scan images in the upper and middle rows. Buckling was defined as the apical surface of a cell descending 4 μm from the vitelline membrane. Buckling of the epithelial layer occurs either within the CF region (light blue arrow and arrowheads, left panels) or outside the CF region (light orange arrow and arrowhead), respectively. Yellow arrowheads indicate additional buckling events that occur either anterior or posterior to the pre-CF region. White asterisks, mitotic rounding of MD6 cells. Scale bars, 10 μm.

(C) Boxplot of location and timing of epithelial buckling in *btd*^{AX} embryos. Light blue boxplot corresponds to buckling events that occur within the CF region (n = 3/7 embryos), and light orange corresponds to events outside the CF region (n = 4/7 embryos). The first buckling event in each embryo was used for quantitation. Gray shading, time range of CF cleft formation in wild-type embryos. Note that buckling occurs at least 10 minutes after the normal time range of CF cleft formation in wild-type embryos.

Figure 8: Expression confirmation of TRAP constructs in the *Drosophila* embryo

(A) Schematic of pTRAP construct. Tandem enhancers for Btd, Eve1, Eve2 and Eve5 drive the upstream expression of GFP-tagged ribosomes (GFP::Rpl10ab) followed by an SV40 terminator (see methods and materials section for details).

(B) Two-photon *en face* live imaging of the lateral surface of embryo expressing TRAP constructs. Yellow arrows indicate the position of CF formation. t = 0 defined as the appearance of the CF cleft formation. Scale bars, 50 μm

(C) Immunofluorescence *en-face* lateral sum projection of a fixed embryos expressing pTRAP constructs labeled with Btd (red), Eve (blue), GFP (green). Embryos are staged to just onset of CF cleft, approximately 10 minutes prior to time of CF cleft formation. Scale bars, 50 μm

Figure 9: Immunopurification of GFP-tagged ribosomes

(A) Schematic chart outlining the fractionation process. Raw embryo lysates were spun down at 2,000G (P2 spin) to obtain two intermediate fractions. P2 supernatant containing lysed cellular contents and the P2 pellet containing non-lysed cells and nuclei. Intermediate fractions were treated with DHPC and centrifuged down at 20,000G (P20 spin) to pellet membrane bound organelles. Fraction 1 and 2 represent the cytoplasmic pool of ribosomes, while Fractions 3 and 4 represent nuclei and membrane organelles.

(B and C) Western blot of embryos expressing ubiquitous GFP-tagged ribosomes. *MatGAL4>GFP::Rpl10ab* embryos were aged 0~12 hours (B) or 2.5-3.5 hours (C) and lysed (see methods and materials section for details). (B) 10 ug of sample from 0~12 hour lay were loaded for Fractions 1-4 and blotted using anti-GFP antibody. (C) 10ug (1x) of sample from 2.5-3.5 hour lay were loaded for Fractions 1-4 and blotted with anti-GFP antibody. Green box represents the desired molecular weight of GFP::Rpl10ab fusion protein (approx. 51.1 kD)

Figure 10: Localized requirement of Eve1 expression in CF formation

(A) Schematic diagram of the *eve^{R13}+Eve2-7* construct. The full *eve* locus was modified through homologous recombination to remove the Eve1 enhancer and the Late Element enhancer. Coding sequence for the fluorescent protein mNeonGreen replaced the stop codon of the *eve* coding region to generate a C-terminal fusion protein (see methods and materials section for details).

(B) Standard deviation projection of the lateral surface (left column) and single plane coronal (right column) of representative *wild-type*, *eve*^{R13}, *eve^{R13}+Eve1*, and *eve^{R13}+Eve2-7* embryos

immunostained for Neurotactin (membrane, green) and Eve(magenta). Yellow arrows indicate expected position of CF bulge. Scale bar, 50 μm.

Figure 11: Eve1 and the planar polarization of MyoII in the CF region

(A-D) Time lapse series of the CF region in a representative *eve* mutant embryo expressing MyoII-GFP and Gap43-mCherry (Membrane) imaged *en face* (A, B) or expressing MyoII-mKate2 imaged at a coronal section displaying either early (C) or late (D) basal MyoII disassembly. t=0 defined as MD2 mitotic cell rounding; 15 min prior to MD2 is the estimated normal timing of CF cleft formation in the wild-type. Orange arrows, basal MyoII; orange arrow with dashed line, disassembled basal MyoII.

(E-H) Sum projection of MyoII-mKate2 imaged *en face* in an embryo representative of wild-type (E), *eve* mutant (F), *eve* mutant expressing Eve1 (G), or *eve* mutant expressing Eve2-7 (H), comparing the CF and GB regions. 14 min prior to MD6 anaphase onset is the estimated normal timing of CF cleft formation in the wild-type.

(I and J) MyoII-mKate2 intensities and polarization as a function of time in wild-type (n = 4 embryos), *eve* mutants (n = 4 embryos), *eve* mutants expressing Eve1 (n = 5 embryos), and *eve* mutants expressing Eve2-7 (n = 5 embryos), comparing the CF and GB regions. t=0 defined as MD6 anaphase onset; shaded gray, observed timing of CF cleft formation. MyoII intensities are normalized mean pixel intensities. Error bands, s.d. Polarization indexes are the ratio between the means of normalized total intensities of MyoII foci with a major axis within 45º of the A-P and D-V axes. Quantitation of MyoII intensities in the CF region was terminated at -14 min because cell internalization during CF initiation rendered MyoII quantitation unreliable. The trend lines are second degree polynomial fit. Representative areas used for quantitation are shown in (E-H).

Figure 12: Phenotypic outcomes of Buttonhead misexpression

(A) Immunofluorescence *en-face* lateral sum projection of a fixed embryos expressing nuclear localized GFP using *MatGal4*, *Gal4-bcd 3'UTR*, and *Krcd1Gal4* drivers in wild-type embryos labeled with Btd (green), Eve (red) and DAPI (blue) and GFP (grey). Scale bar, 50 μm.

(B) Immunofluorescence *en-face* lateral sum projection of a fixed embryos expressing Btd using *MatGal4*, *Gal4-bcd 3'UTR*, and *Krcd1Gal4* drivers in wild-type embryos labeled with Btd (green), Eve (red) and DAPI (blue) in wild-type embryos (left two columns, refer to Fig 4D for *Gal4-bcd 3'UTR*) and in *btd* mutant embryos (right three columns). Scale bar, 50 μm.

(C) Isosurface reconstruction of Btd misexpression embryos generated by UCSF Chimera Visualization System (Pettersen et al., 2004). Embryos were fixed and staged based on progression and the morphology of the PMG. Top row, GFP driven by enhancer sequences in *wild-type* background; Middle row, Btd cDNA driven by enhancer sequences in *wild-type* background; Bottom row, Btd cDNA driven by enhancer sequences in *btd* mutant background. Magenta arrows, CF; red arrows, dorsal folds (DFs); green arrows, CF like structure; cyan arrows, ectopic bucklings. Scale bar, 50 μm.

Figure 13: Targeted misexpression of Buttonhead in Eve2 region

(A) Schematic of construct used to misexpression Btd under the control of specific cell type enhancers (Tandem enhancer). Membrane localized GFP (*CD4tdmGFP*) is flanked by FRT sites, upstream of Buttonhead cDNA. In the absence of FLP, CD4tdmGFP will be expressed. Presence of FLP will remove the *CD4tdmGFP* cassette, allowing for the expression of Btd cDNA (see methods and materials section for details).

(B) Time lapse two-photon images of un-flipped embryos expressing CD4 tandem GFP (grey) under the control of either Btd, Eve1, Eve2 or Eve5 enhancers. Yellow arrows indicate location of CF formation. t = 0 defined as the appearance of the CF cleft formation Scale bar, 50 μm

(C) Immunofluorescence *en-face* lateral sum projection of a fixed embryos expressing the misexpression construct under control of Eve2 enhancer labeled with Btd (red), Eve (blue), and GFP (green). Embryos are staged to just onset of CF cleft, approximately 10 minutes prior to time of CF cleft formation. Scale bar, 50 μm.

(D) Isosurface reconstructions generated by UCSF Chimera Visualization System (Pettersen et al., 2004). Embryos were fixed and staged based on progression and the morphology of the PMG. Magenta arrows, CF; red arrows, dorsal folds (DFs); green arrows, CF like structure; cyan arrows, ectopic bucklings. Scale bar, 50 μm.

Supplemental figure legends

Supplemental figure 1: Temporal and spatial dynamics of CF imitation through *in toto* SPIM imaging

(A) Timing of CF initiation in three representative SPIM recordings. Time was color-coded relative to the first cell that initiates (t = 0) with the position of initiation projected onto the embryonic circumference.

(B) Bilateral difference of percentage initiation as a function of time from three representative embryos analyzed in (B).

(C) Linearity of the CF structure. The CF structure is approximated by the nuclear position of the initiating cells assayed in SPIM 3D nuclear tracking (Figure S1A). A representative timepoint (left) of linearity test with a 3D planar fit (gray parallelogram) to the nuclear position (blue circles); the root mean square error (RMSE) of the fit plotted as a function of time prior to and during initiation on the scale of 8 μm representing approximately one cell diameter in live embryos (right). t = 0 defined as the time when the first cell initiates.

(D) Timing of CF nuclear internalization tracked in a SPIM recording of a H2Av-mCherry embryo (left). Time was color-coded relative to the first cell that initiates (t = 0) with nuclear positions projected onto the embryonic circumference. Time course during the first 3.5 minutes of initiation showing the lateral most nuclei (right). Gray circles, nuclear positions at the start of imaging; cyan circles, nuclei that have not started internalization; red circles, nuclei that have started initiation.

Supplemental figure 2: Laser ablation demonstrates tension along interface (0).

(A) Schematic representation of laser ablation (left) and *en face* images (right) of pre- and post-ablation at an interface (0) (top) and a control interface (bottom) in embryos expressing MyoII-GFP (green) and Gap43-mCherry (magenta). Yellow dashed lines, laser ablation lines. Scale bar, 1 μm.

(B and C) Change of distance between the two flanking vertices (recoil distance) as a function of time after laser ablation (B) and boxplot of maximal recoil distance within 20 seconds after ablation (C). Error bands, SD. **, $p < 0.01$.

(D) Correlation analysis between maximal recoil distance as in (G) and total MyoII intensity associated with the interface between the two flanking vertices. ρ, Spearman rank-order correlation coefficient. Sample size in (F-H): CF, n = 21; controls, n = 13

Supplemental figure 3: MyoII is non-uniformly enriched at interface (0)

(A) Distribution of MyoII-GFP foci (red) along the 3D rendering of a “ribbon” of interconnected interfaces (0) segmented based on Gap43-mCherry (gray mesh) across a lateral span of 8 P(0) cells (green). t = 0 defined as CF cleft formation. The cross-sections of the “ribbon” at three z planes [5 μm (gray), 15 μm (lilac), and 25 μm (dark blue) from embryo surface] is shown. A total

z depth of 28 μm from the embryo surface was imaged, representing ~75% of the apical-basal axis.

(B) Illustration of the steps required to generate the 2D grid system for MyoII intensity analysis at the cell interfaces (Figures 4D-F). Cells were segmented (cyan outline) to define the cell centroids (yellow stars, left). Single D-V cell rows (pink and purple) were established from manually identified type IIa or type I cells (yellow dots, center). The cell interfaces are registered to this grid system (right). Yellow, green, red, purple and brown boxes in the right panel indicate the regions representing interfaces (-2), (-1), (0), (+1) and (+2) respectively.

(D and E) Cumulative (D) and time-dependent (E) total MyoII intensity associated with each "ribbon" of interconnected interfaces for a total z depth of 28 μm analyzed in a D-V row of (Embryo 1) or 6 (Embryo 2 and 3) cells. t = 0 defined as CF cleft formation.

(F) Pair-wise comparison of time-dependent total MyoII intensities at each D-V cell row between interface (0) and (-1) in the three embryos analyzed in (D) and (E). t = 0 defined as CF cleft formation. Initiating cell type annotations: I, type I; IIa, type II anterior; IIp, type II posterior cell mis-positioned at P(0). Pink rectangles highlight times and locations where interface (+1) contains higher MyoII than (0).

Supplemental figure 4: Variability in MyoII behavior does not scale with patterning noise

(A) Illustration of the steps required to generate the 2D grid system for MyoII intensity analysis at the cell interfaces (Figures 4D-F). Cells were segmented (cyan outline) to define the cell centroids (yellow stars, left). Single D-V cell rows (pink and purple) were established from manually identified type IIa or type I cells (yellow dots, center). The cell interfaces are registered to this grid system (right). Yellow, green, red, purple and brown boxes in the right panel indicate the regions representing interfaces (-2), (-1), (0), (+1) and (+2) respectively.

(G-I) Correlation analyses between MyoII-mKate2 and Eve-LlamaTag intensities at three different scales: (G) time-dependent at the cellular scale, (H) cumulative at the cellular level, and (I) cumulative at the tissue scale (“ribbon” of interfaces). Intensities were normalized to the min and max intensities within each embryo. For each cell (G and H) or each row of cells (I) expressing Eve, two correlation analyses (“A” and “P”; see Figure S4E) were performed, each for MyoII at the anterior and posterior interfaces, respectively. Imaging dimensions: total z depth = 57 μm; D-V span = 8 ~ 9 cells. n = 4 embryos. ρ, Spearman rank-order correlation coefficient.

(F-G) Embryo-by-embryo analysis of Eve and MyoII intensities from -4 to 0 min with t0 defined as CF cleft formation. (F) The bar graphs of mean Eve-LlamaTag intensities at each position. The Eve-LlamaTag intensity was normalized to the min and max within each embryo at a given time. For each cell, the mean over the duration of analysis was used to represent its Eve intensity. (G) Cumulative MyoII intensities as a function of time at each interface normalized to the min and max within the embryo.

(J) Coefficient of variation (CV) showing the spatial variability of MyoII-mKate2 and Eve-LlamaTag along each “ribbon” of interfaces (MyoII) or cell position (Eve-LlamaTag) along the D-V axis. MyoII and Eve intensities were normalized as in (G). n = 4 embryos.

Scale bars, 10 μm. See also Movies S3.

Supplemental figure 5: Force transmission between adherens junctions spatially aligns CF initiation

(C) Boxplot of CF cleft depths in wild-type (n = 6) and *α-Cat* RNAi (n = 5) embryos at the end of cellularization. The wild-type dataset is the same as the one used in Figure 5C.

(G and H) CF alignment in wild-type and *α-Cat* RNAi embryos. (G) Angle analysis for cellular scale alignment shown as boxplot and representative images. The θ's denote angles formed by

the interconnected interfaces (0) that are analyzed in the boxplot. Green segmented lines, interfaces (0). Magenta segmented cells, initiating cells. (H) Tissue scale alignment shown as boxplots for 3D tortuosity (left) and change in tortuosity along the z axis relative to the z slice 4 μm below embryo surface (right). These analyses were performed in a D-V span of 15 ± 3 cells in wild-type (n = 7 embryos) and 13 ± 2 cells in *α-Cat* RNAi (n = 7 embryos). One frame prior to the first cell descended below the surface was analyzed. Angles (G) and 3D tortuosity (H) were analyzed at z = 4 μm below embryo surface. **, $p< 0.01$; ****, $p< 0.0001$.

(D) Boxplot comparing wild-type (n = 6) and *α-Cat* RNAi (n = 5) embryos for the percentage of voxels within the “ribbon” of interfaces (0) that contain MyoII intensity above the background. The background for a given embryo was set as the highest voxel intensity of MyoII in a control ribbon located 3-4 cell rows anterior to interface (0). n.s., not significant.

(I and J) Linear fit of P(0) and CF cleft positions, and the offset between CF cleft positions to the P(0) linear fit in *α-Cat* RNAi (n = 10) embryos. Linear fit (I) and percentage match to P(0) (J) were analyzed in fixed embryos the same way as, and compared to the data, in Figures 2I and 2L. Purple dashed line defined as in Figure 2L. *, $p< 0.05$; **, $p< 0.01$; n.s., not significant.

Scale bars, 10 μm. See also Figure S4, S5, S6; Movies S4, S5, S6.

(E) Boxplot of location and timing of epithelial buckling in btd^{AX} embryos. Light blue boxplot corresponds to buckling events that occur within the CF region (n = 3/7 embryos), and light orange corresponds to events outside the CF region (n = 4/7 embryos). The first buckling event in each embryo was used for quantitation. Gray shading, time range of CF cleft formation in wild-type embryos. Note that buckling occurs at least 10 minutes after the normal time range of CF cleft formation in wild-type embryos.

(A) 3D representation of the “unwrapping” procedure and interface (0) for a representative wild-type embryo. See Methods for definition for the z, z′ stacks, and the “reference arc”. z_{ref} and z'_{ref}, the reference surface for the z and z′ stacks, respectively.

(B) Representative images of the original z image at 16 μm below the reference surface z_{ref} and the “unwrapped” z′ image at 4 μm below the reference surface z'_{ref}. The purple segmented line denotes interface (0).

(C and D) 3D visualization (C) of the procedures that approximate the shortest the distance (the “reference arc”) between the two ends points of interface (0), and the representative plot (D) of the arc length as a function of iterations for that approximation. See Methods for definition for the initial and reference arcs, and the description of the iterations.

Supplemental figure 6: Local reduction of myosin contractility via optogenetics increases imprecision in CF spatial alignment

A) CRY2-mCherry-DNRho1 membrane recruitment shown as normalized increase of fluorescence as a function of time, comparing control (without pm-CIBN, n = 8) and experimental (with pm-CIBN, n = 6) embryos. Error bands, SD.

(B and C) Time lapse series of a control (B) and experimental (C) embryo imaged *en face* (top, 11 μm below embryo surface) and at a coronal section (bottom) showing the effect of opto-DNRho1. t = 0 defined as MD2. Imaging (λ = 1040 nm) and photoactivation (λ = 950 nm for a duration of 28 s) were executed at the same z-depth (11-15 μm below embryo surface). Cyan rectangles, ROIs for optogenetic activation.

(D) Timing of CF cleft formation in control embryos. t = 0 defined as MD2. Purple dashed line denotes 400 s prior to MD2, when data in (E) is measured. n = 7 embryos.

(E) Boxplot of CF cleft depth measured 400 s prior to MD2, comparing control (n = 7) and experimental (n = 6) embryos. ***, $p < 0.001$.

(F and G) Time lapse series of max projection of a control (F) and experimental (G) embryo imaged *en face* (top) with coronal views (middle and bottom) imaged within (at the orange line, top) or outside (at the blue line, top) the activation ROI (cyan rectangular masks in the top rows). t = 0 defined as CF cleft. Left, one frame prior to first cell descending when the angle analyses (I) were performed. Right, time point at which all cells descended. Imaging (λ = 1040 nm) and photoactivation (λ = 950 nm for a duration of 10 s) were executed at the same z-depth (11-15 μm below embryo surface). Green segmented line, interface (0). Magenta segmented cells, initiating cells. “I”-shape red symbols denote CF cleft depths at t = 0. Annotations at t = 0 in the top row depict alignment analysis performed in (J and K). Lines were drawn to fit the furrow structures from dorsal (dashed green) and ventral (dashed orange) sides, with connecting lines shown in yellow. θ_1 and θ_2 are the two angles measured to estimate the deviation from perfect alignment as in (J).

(H and I) Boxplots of time gaps (H) between the descent of last cells within and outside activation ROI (at timepoints as in the center and right panels of F and G), and angles (I) formed by the interconnected interfaces (0) (measured at timepoints as in the left panels of F and G, one frame prior to the first cell descended). *, $p < 0.05$; **, $p < 0.01$; n.s., not significant. Sample size: controls, n = 7; experimental, n = 12.

(J) Schematics of alignment analysis performed in (K) for the optogenetically bisected furrow structures. θ_1 and θ_2 defined as in (F and G)

(K) Boxplot of degrees of deviation from 360˚ as an estimate of the misalignment between the optogenetically bisected furrow structures. *, $p < 0.05$. Sample size: controls, n = 7; experimental, n = 12.

Scale bars, 10 μm.

Supplemental figure 7: 3D vertex modeling reveals that a CF-like mechanical system is robust against spatial and temporal noise

(A) Visual representation of the 3D vertex model under the settings of tension pattern (a) depicted in (B) at the start (t = 0) and end (t = 80) of simulation.

(B) Schematics of 6 tension patterns designed to mimic the observed MyoII spatial distribution and initiating cell behaviors for simulation performed in (D).

(C) Visual representation of apical vertices of tension pattern (a) at the start (t = 0) and end (t = 80) of simulation. Color map denotes z position of the vertices. Color-coded horizontal lines drawn at t = 0 denote cross-sectional slicing planes used for analyses performed in D4 and E4.

(D and E) Quantitation of four morphological features during CF-like folding (interface alignment, fold depth, D-V and A-P cross-sectional profiles) in response to noise. Spatial noise (D) was introduced via 6 designed tension patterns (B), while temporal noise (E) was introduced as Gaussian white noise at varying strengths given by the SD, σ. Quantitation (mean value with an error bar as SD) is shown as a function of time (D1 and D2), as a function of noise strength at the final (t = 80) timepoint (E1 and E2), as cross-sectional profiles at the final timepoint along the D-V axis (D3 and E3), or the A-P axis. Simulation data quantified along the slicing plane AP axis #3 shown in (C) from all six tension patterns were superimposed for D4, while all seven simulation iterations with the noise strength σ = 1.0 were superimposed for E4. D2-D4 and E2-E4 were plotted on the scale of half-cell height.

See also Figure S8 and Methods, 3D vertex modeling.

Supplemental figure 8: 3D vertex modeling reveals that a CF-like mechanical system is robust against spatial and temporal noise

(A and B) Fold depths (A) and planar alignment of the central interface along the D-V axis (B) with mechanical settings that simulate CF-like [blue; “CF”; Eq(3) Methods], isotropic lateral contraction (black; “CF_{homo}”), VF-like [red; “VF”; Eq(4) Methods], and GBE-like [green; “GBE”; Eq(5), Methods] mechanical manipulations. Note that only the CF-like mechanical condition results in deep folding and efficient alignment of the central interface.

(C) Coefficient of variation for assessing the spatial variability of contractility in the simulations of temporal noise (Figure S7E1 and S7E2) with noise strengths at SD (σ) = 0.9, 1.0 and 1.2. For a given simulation of σ, data from 80 simulation time points and of all 10 iterations of simulations were aggregated.

Movie figure legends

Movie S1. Time-lapse, whole embryo SPIM recording of a H2Av-mCherry embryo during the onset of gastrulation (left). Transverse view of projected initiating cells provides visualization of the temporal and spatial pattern of nuclear internalization (right). Gray circles, nuclei position at the start of imaging; cyan circles, nuclei that have not started internalization; red circles, internalized nuclei as defined by a 5 μm drop from the initial position indicated as gray circles (right). This movie is analyzed in Figure S1A.

Movie S2. Time-lapse coronal images of two wild-type embryos expressing Gap43-mCherry (membrane, left column) and MyoII-GFP (right column) for type I and type II initiation cell behaviors (top and bottom panels, respectively). Scale bars, 10 μm. Stills of this movie are shown in Figures 1E and 3A; MyoII intensity of the bottom panels is analyzed in Figure 3B.

Movie S3. Time-lapse sum projected *en face* lateral images of wild-type (top) and *runt*^{B5} (bottom) embryos expressing Gap43-mCherry (membrane, left column) and MyoII-GFP (right

column). Cyan and orange boxes indicate regions shown as still images for the CF and GB regions, respectively (Figures 3F and 4E). Scale bars, 10 μm.

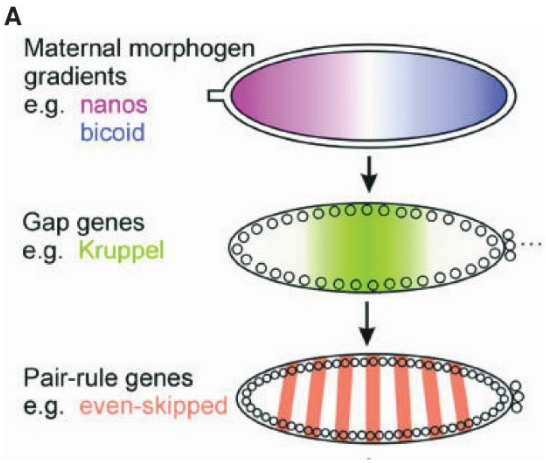
Movie S4. Time-lapse coronal images of wild-type, *btd*^{AX}, and *runt*^{B5} embryos expressing Gap43-mCherry (membrane, left column) and MyoII-GFP (right column). Stills of this movie are shown in Figure S5A. Scale bars, 10 μm.

Movie S5. Time-lapse images of two *eve* mutant embryos expressing MyoII-mKate2**.** For each embryo, three views were shown: sum projected *en face* lateral view (upper left), coronal view (lower left) and enlarged view of the presumptive CF region highlighted by the white rectangular ROI (right). Scale bars, 10 μm.

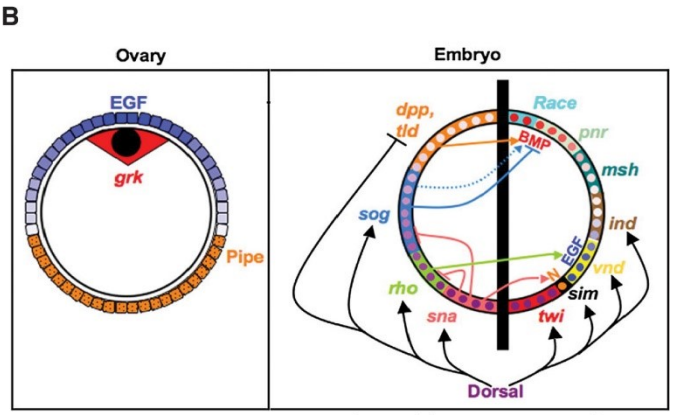
Movie S6. Time-lapse sum projected lateral *en face* images of *btd*^{AX} (top) and *eve*^{R13} (bottom) embryos expressing Gap43-mCherry (membrane, left column) and MyoII-GFP (right column). Cyan boxes, CF region; orange boxes, GB region. Cyan and orange boxes that labeled the *btd*^{AX} images are used as still images shown in Figure 4D. Scale bars, 10 μm.

Figures

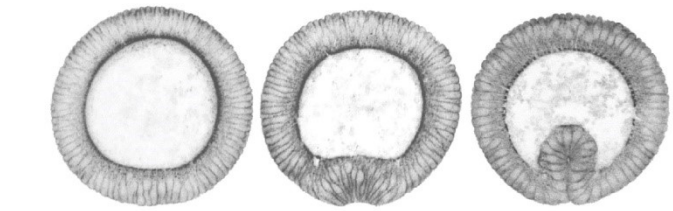
Figure 1.1



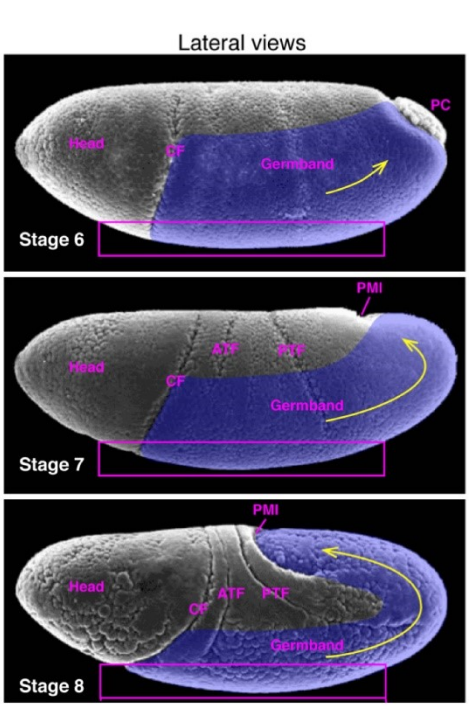
adapted from Sanson, 2001



adapted from James et al., 2002

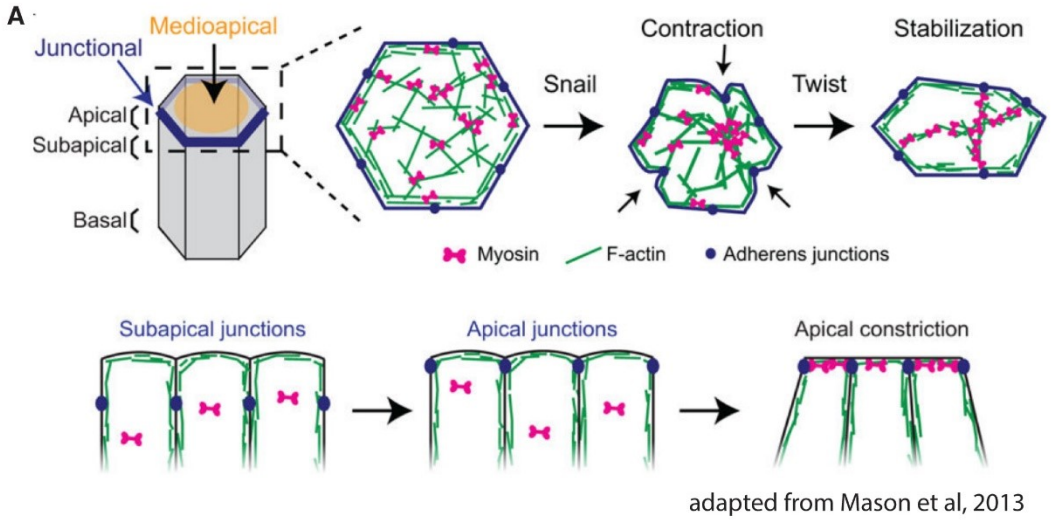


adapted from Conte et al., 2003

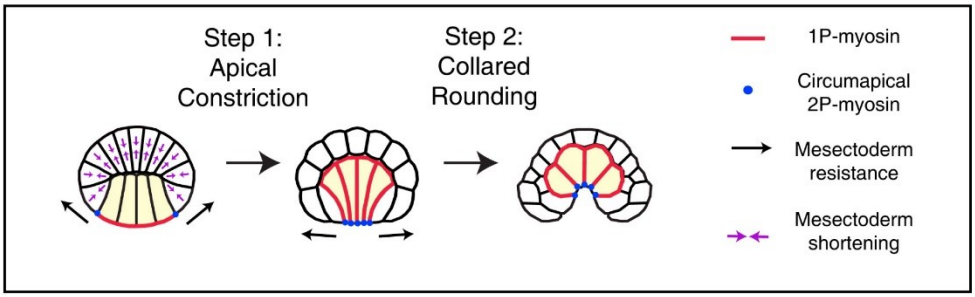


adapted from Lye et al., 2015

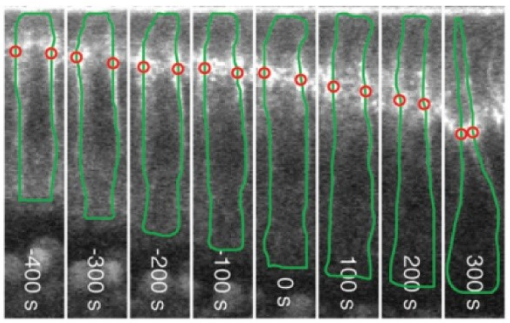
Figure 1.2



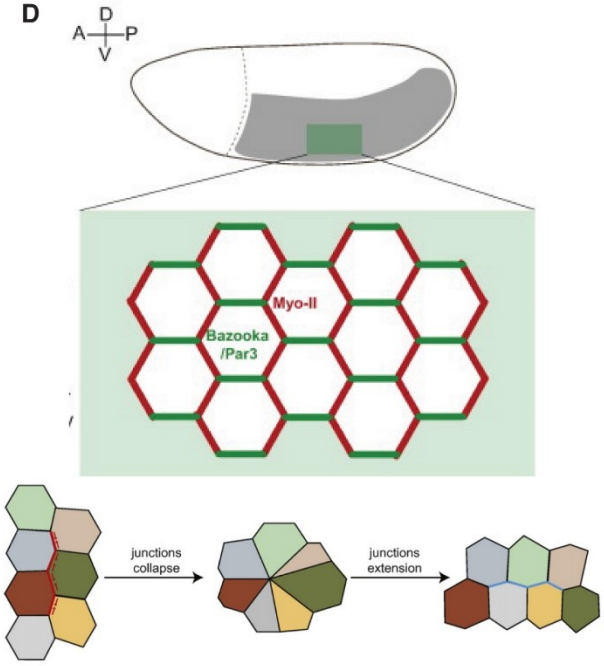
adapted from Mason et al, 2013



adapted from Sherrard et al., 2010



adapted from Wang et al., 2012



adapted from Kong et al., 2017

Figure 2

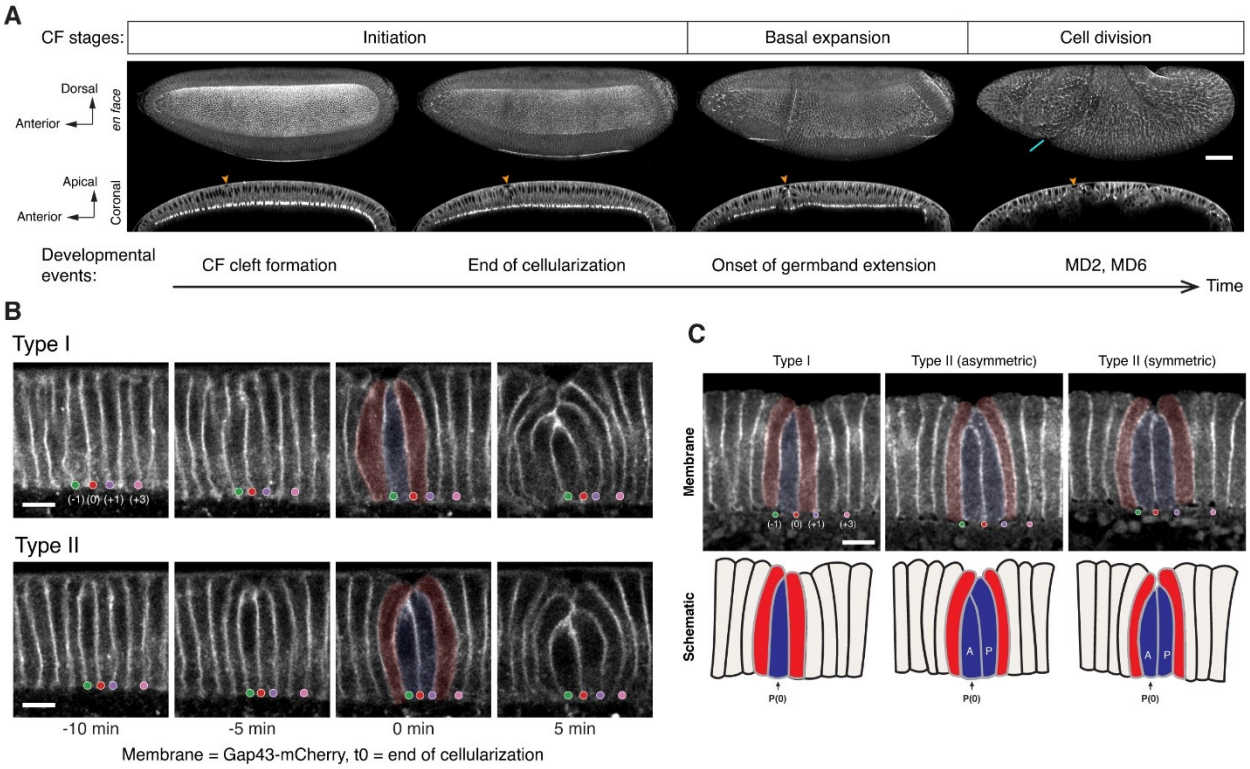

A
CF stages:
Initiation
Basal expansion
Cell division
Dorsal
Anterior
en face
Apical
Anterior
Coronal
Developmental events:
CF cleft formation
End of cellularization
Onset of germband extension
MD2, MD6
Time
B
Type I
Type II
(-1) (0) (+1) (+3)
-10 min
-5 min
0 min
5 min
Membrane = Gap43-mCherry, t0 = end of cellularization
C
Type I
Type II (asymmetric)
Type II (symmetric)
Membrane
Schematic
A
P
P(0)
D
Type I
Type II
Normalized length
Tortuosity
Time (min)
(-1)
(0)
(+1)
(+3)
t0 = end of cellularization
E
Frequency
Type I
Type II
F
Type I
Type II
Frequency
DV position (μm)
5.2
15.4
25.8
36.1
46.4
56.6

Figure 3

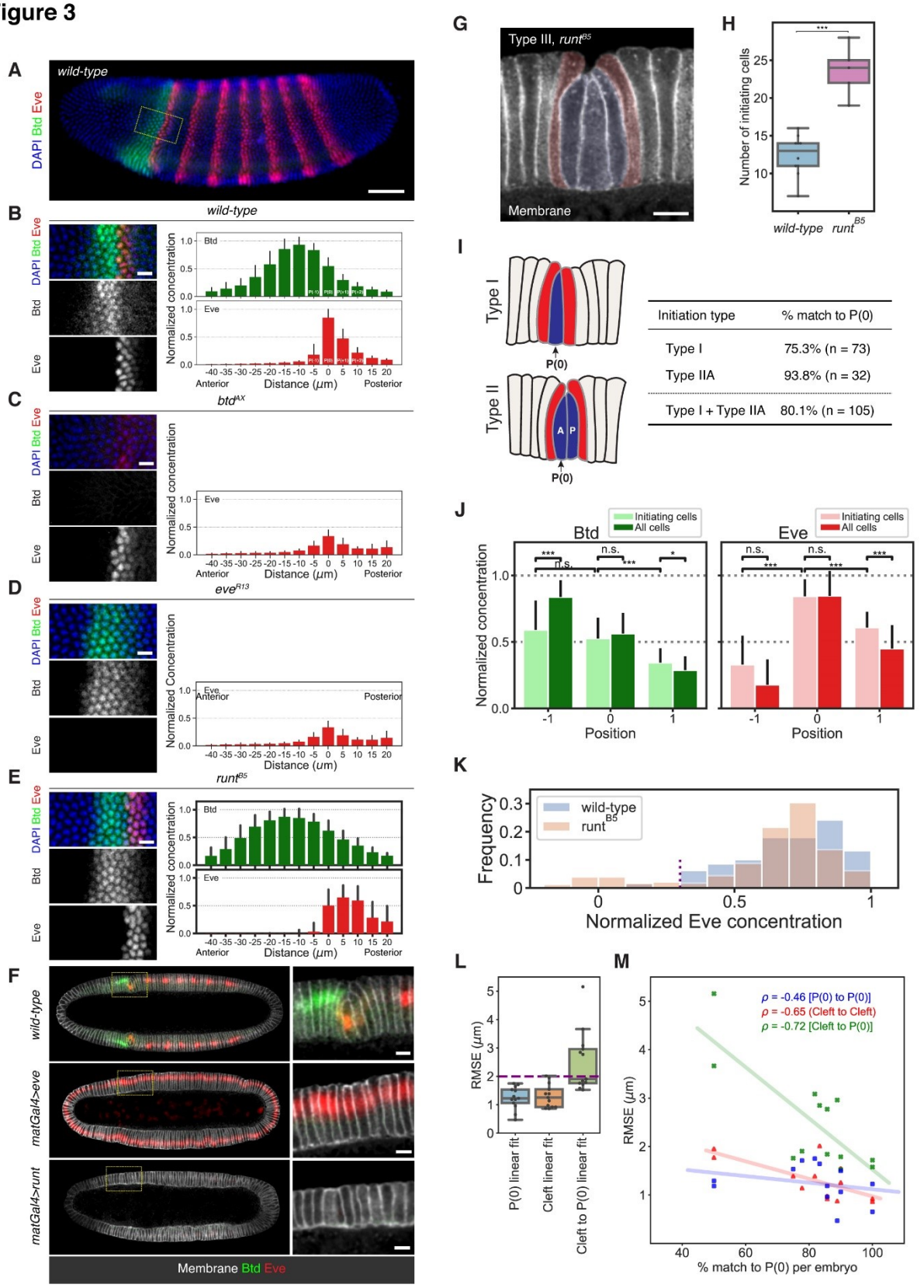

A
wild-type
DAPI Btd Eve
B
wild-type
DAPI Btd Eve
Btd
Eve
Normalized concentration
Btd
Eve
Anterior
Distance (μm)
Posterior
btd^AX
C
eve^R13
D
runt^B5
E
F
wild-type
matGal4>eve
matGal4>runt
Membrane Btd Eve
G
Type III, runt^B5
Membrane
H
Number of initiating cells
wild-type
runt^B5
I
Type I
Type II
P(0)
A P
Initiation type
% match to P(0)
Type I
75.3% (n = 73)
Type IIA
93.8% (n = 32)
Type I + Type IIA
80.1% (n = 105)
J
Btd
Eve
Initiating cells
All cells
n.s.
Normalized concentration
Position
K
wild-type
runt^B5
Frequency
Normalized Eve concentration
L
RMSE (μm)
P(0) linear fit
Cleft linear fit
Cleft to P(0) linear fit
M
ρ = -0.46 [P(0) to P(0)]
ρ = -0.65 (Cleft to Cleft)
ρ = -0.72 [Cleft to P(0)]
RMSE (μm)
% match to P(0) per embryo

Figure 4

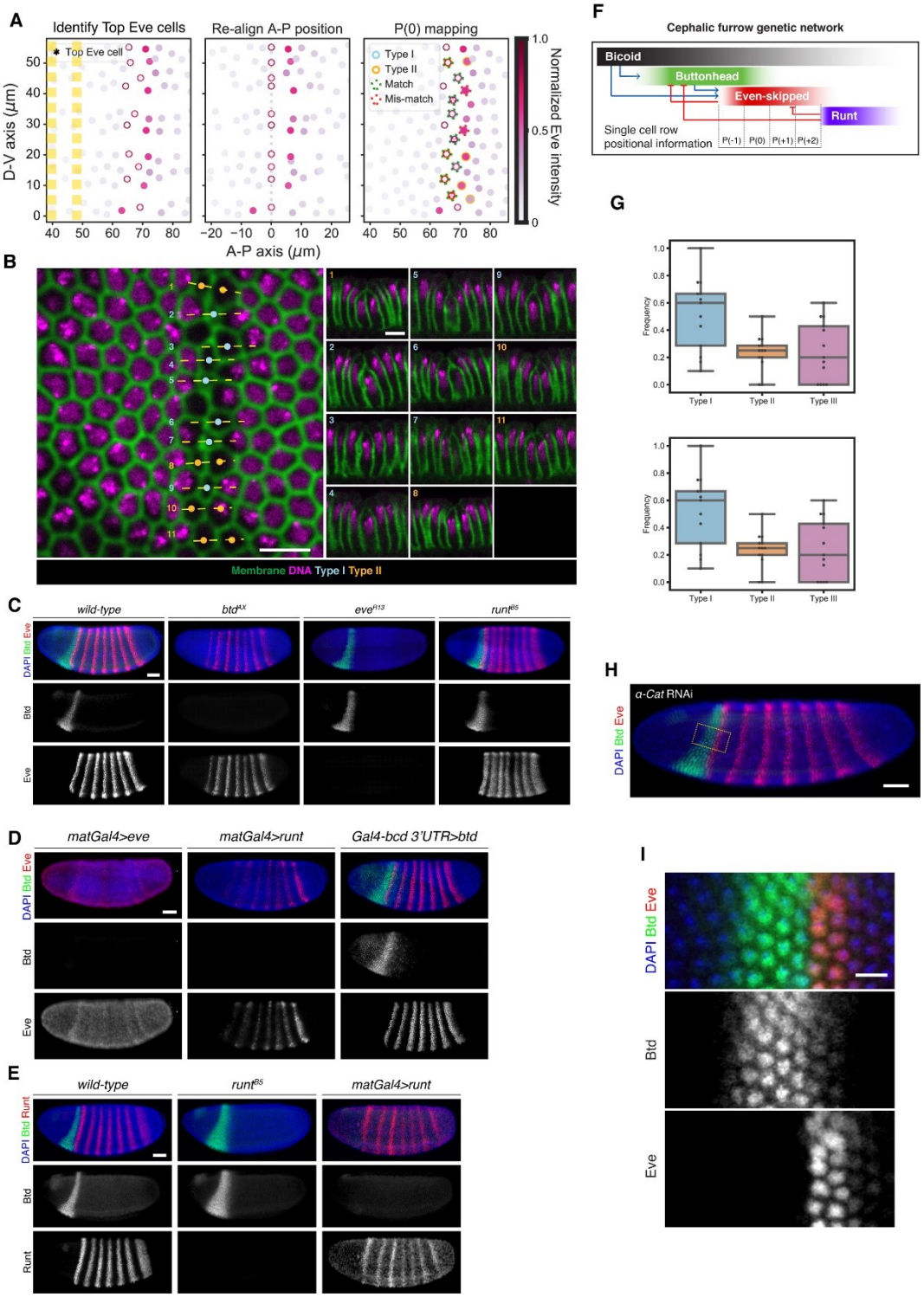
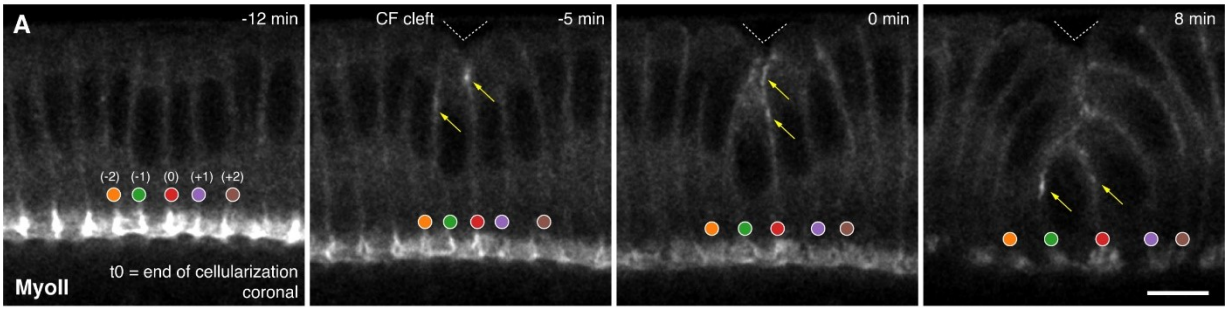
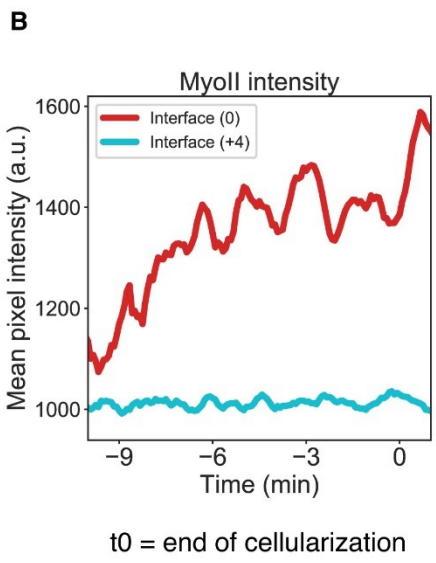
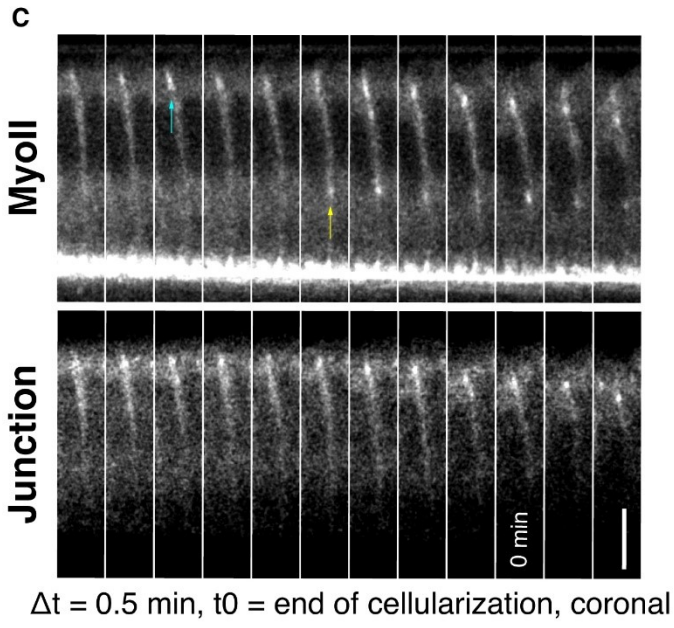

A
Identify Top Eve cells
Re-align A-P position
P(0) mapping
Top Eve cell
Type I
Type II
Match
Mis-match
D-V axis (μm)
A-P axis (μm)
Normalized Eve intensity
B
Membrane DNA Type I Type II
C
wild-type
btd^AX
eve^R13
runt^RS
DAPI Btd Eve
Btd
Eve
D
matGal4>eve
matGal4>runt
Gal4-bcd 3'UTR>btd
E
wild-type
runt^RS
matGal4>runt
DAPI Btd Runt
Runt
F
Cephalic furrow genetic network
Bicoid
Buttonhead
Even-skipped
Runt
Single cell row positional information
P(-1)
P(0)
P(+1)
P(+2)
G
Frequency
Type I
Type II
Type III
H
α-Cat RNAi
DAPI Btd Eve
I
DAPI Btd Eve
Btd
Eve

Figure 5


A
-12 min
CF cleft
-5 min
0 min
8 min
(-2) (-1) (0) (+1) (+2)
MyoII
t0 = end of cellularization
coronal


B
MyoII intensity
Interface (0)
Interface (+4)
Mean pixel intensity (a.u.)
1600
1400
1200
1000
−9
−6
−3
0
Time (min)
t0 = end of cellularization


C
MyoII
Junction
0 min
Δt = 0.5 min, t0 = end of cellularization, coronal

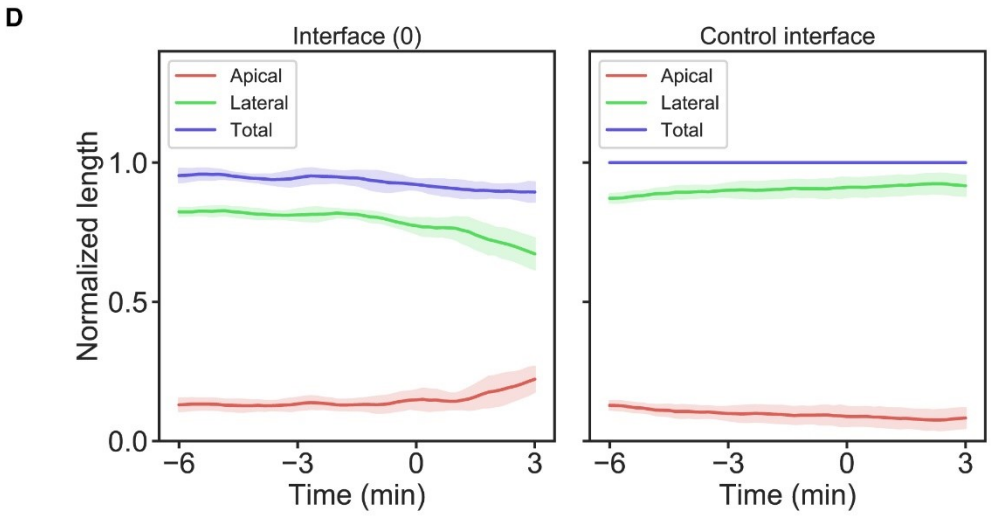

D
Interface (0)
Control interface
Apical
Lateral
Total
Normalized length
1.0
0.5
0.0
−6
−3
0
3
Time (min)
t0 = end of cellularization

Figure 6

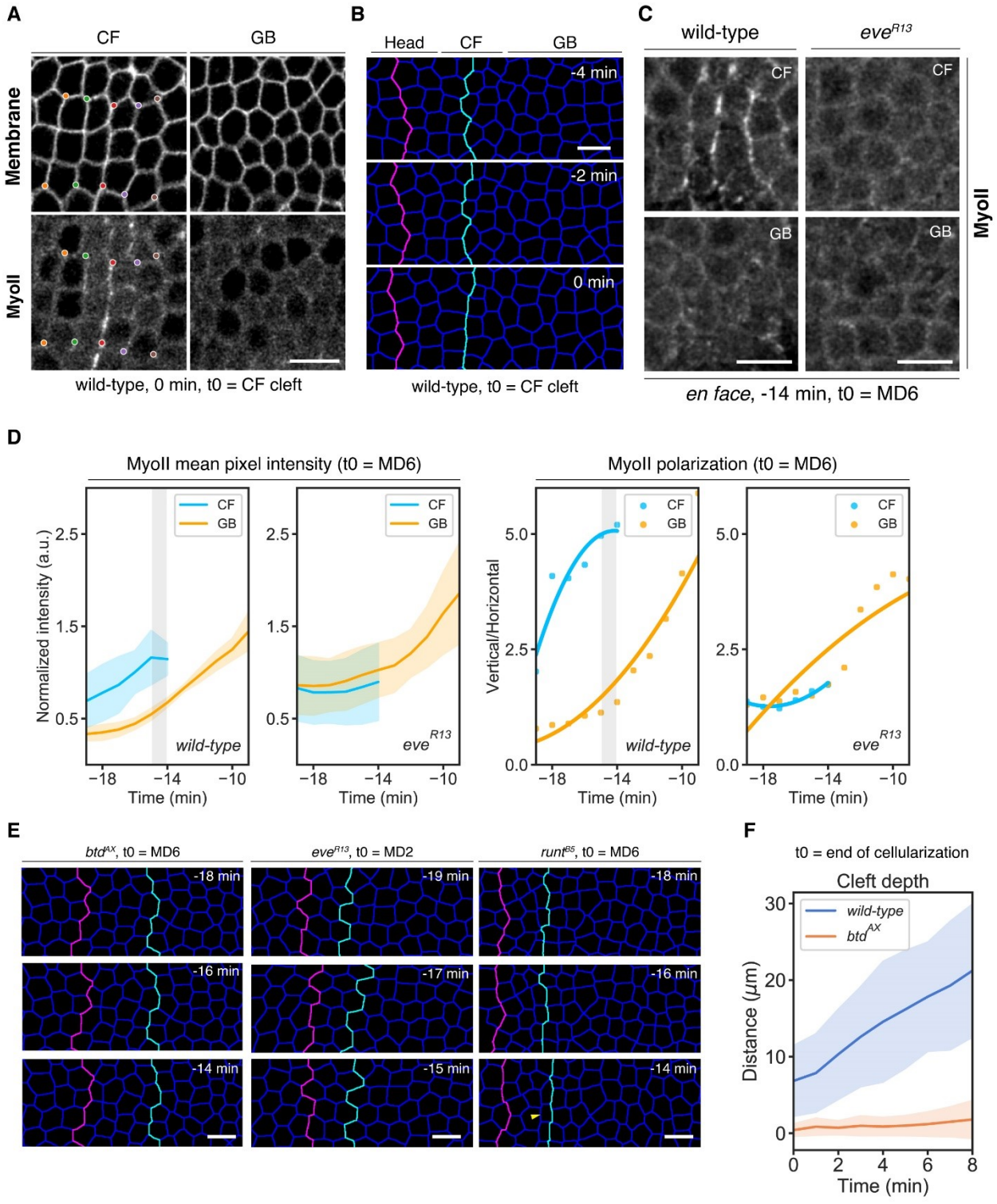

A
CF
GB
Membrane
MyoII
wild-type, 0 min, t0 = CF cleft
B
Head
CF
GB
-4 min
-2 min
0 min
wild-type, t0 = CF cleft
C
wild-type
eve^R13
CF
GB
MyoII
en face, -14 min, t0 = MD6
D
MyoII mean pixel intensity (t0 = MD6)
MyoII polarization (t0 = MD6)
Normalized intensity (a.u.)
Vertical/Horizontal
Time (min)
wild-type
eve^R13
E
btd^AX, t0 = MD6
eve^R13, t0 = MD2
runt^B5, t0 = MD6
-18 min
-19 min
-16 min
-17 min
-14 min
-15 min
F
t0 = end of cellularization
Cleft depth
Distance (μm)
Time (min)
wild-type
btd^AX

Figure 7

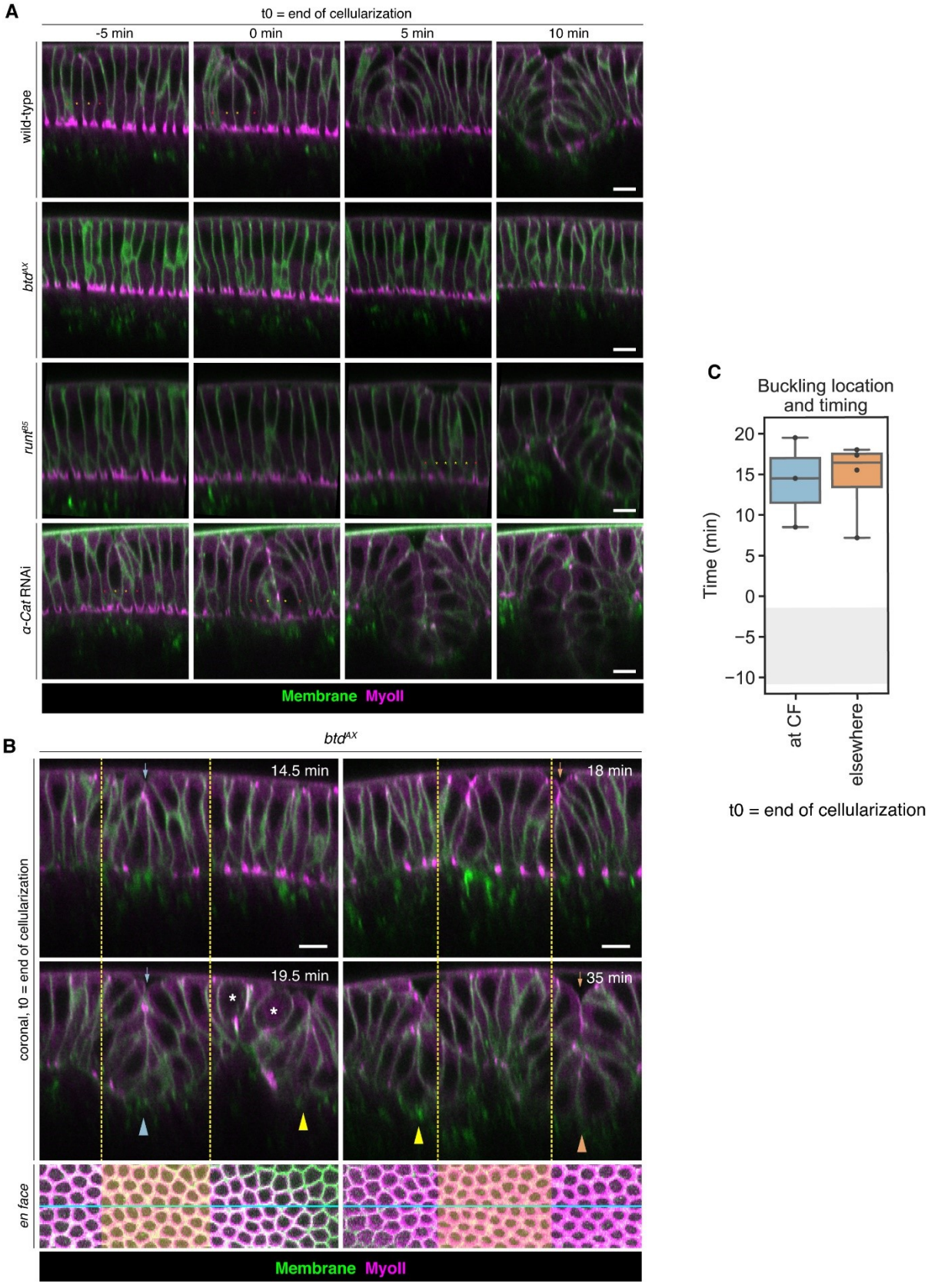

A
t0 = end of cellularization
-5 min
0 min
5 min
10 min
wild-type
btd^AX
runt^B5
α-Cat RNAi
Membrane MyoII
B
btd^AX
14.5 min
18 min
19.5 min
35 min
coronal, t0 = end of cellularization
en face
Membrane MyoII
C
Buckling location and timing
Time (min)
20
15
10
5
0
−5
−10
at CF
elsewhere
t0 = end of cellularization

Figure 8

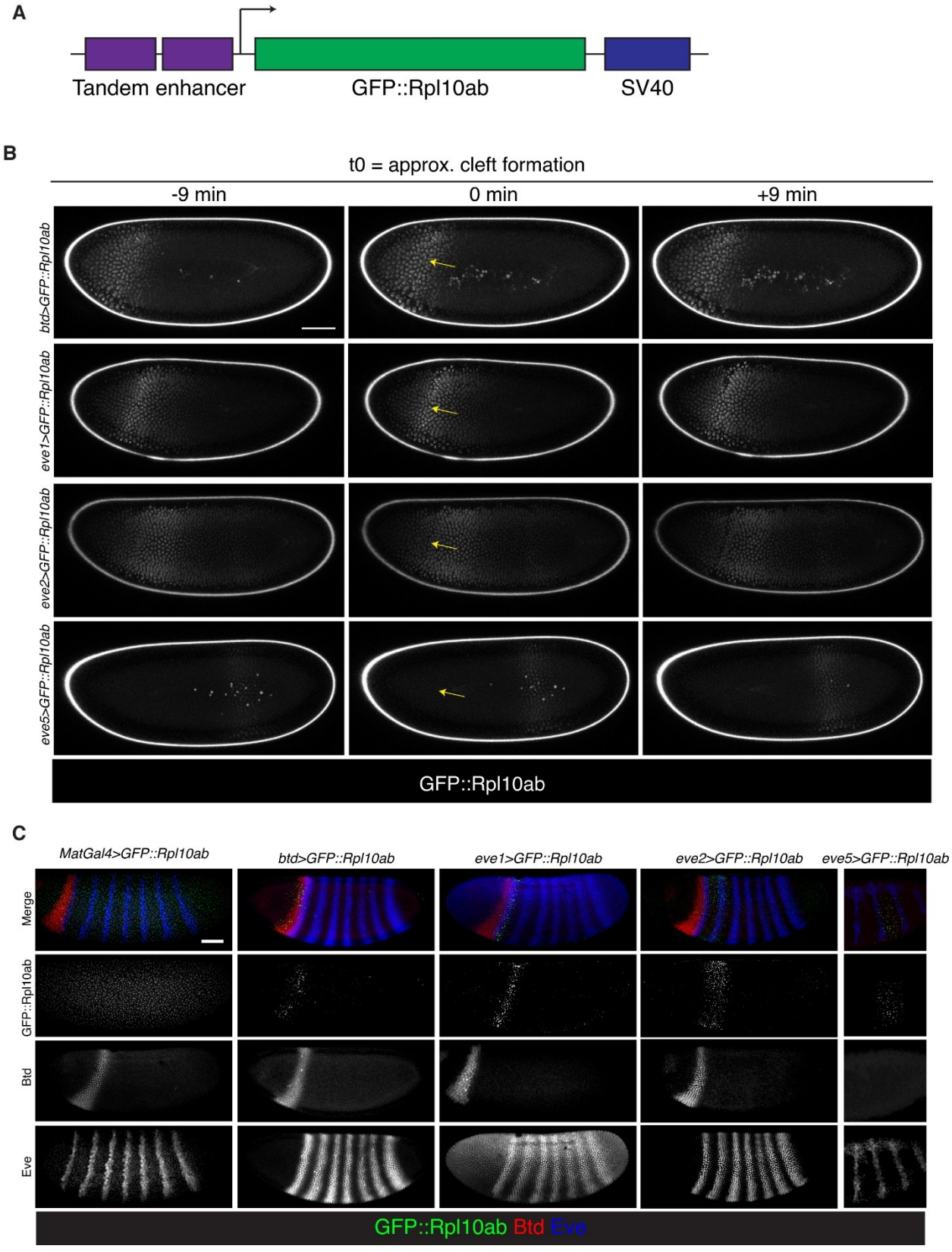

A
Tandem enhancer
GFP::Rpl10ab
SV40
B
t0 = approx. cleft formation
-9 min
0 min
+9 min
btd>GFP::Rpl10ab
eve1>GFP::Rpl10ab
eve2>GFP::Rpl10ab
eve5>GFP::Rpl10ab
GFP::Rpl10ab
C
MatGal4>GFP::Rpl10ab
btd>GFP::Rpl10ab
eve1>GFP::Rpl10ab
eve2>GFP::Rpl10ab
eve5>GFP::Rpl10ab
Merge
GFP::Rpl10ab
Btd
Eve
GFP::Rpl10ab Btd Eve

Figure 9

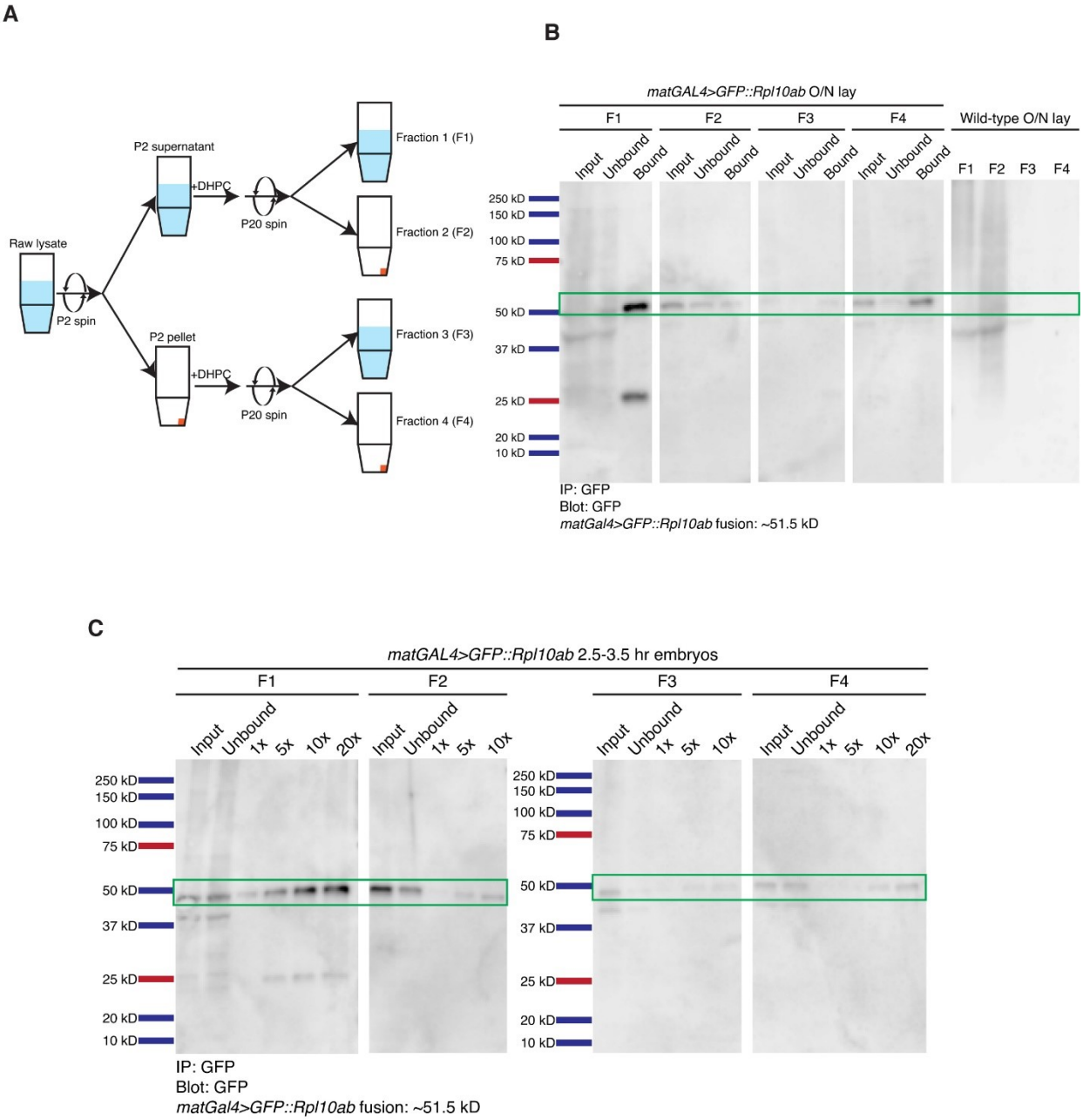

A
Raw lysate
P2 spin
P2 supernatant
+DHPC
P20 spin
Fraction 1 (F1)
Fraction 2 (F2)
P2 pellet
+DHPC
P20 spin
Fraction 3 (F3)
Fraction 4 (F4)
B
matGAL4>GFP::Rpl10ab O/N lay
F1
F2
F3
F4
Wild-type O/N lay
Input
Unbound
Bound
F1
F2
F3
F4
250 kD
150 kD
100 kD
75 kD
50 kD
37 kD
25 kD
20 kD
10 kD
IP: GFP
Blot: GFP
matGal4>GFP::Rpl10ab fusion: ~51.5 kD
C
matGAL4>GFP::Rpl10ab 2.5-3.5 hr embryos
F1
F2
F3
F4
Input
Unbound
1x
5x
10x
20x
250 kD
150 kD
100 kD
75 kD
50 kD
37 kD
25 kD
20 kD
10 kD
IP: GFP
Blot: GFP
matGal4>GFP::Rpl10ab fusion: ~51.5 kD

Figure 10

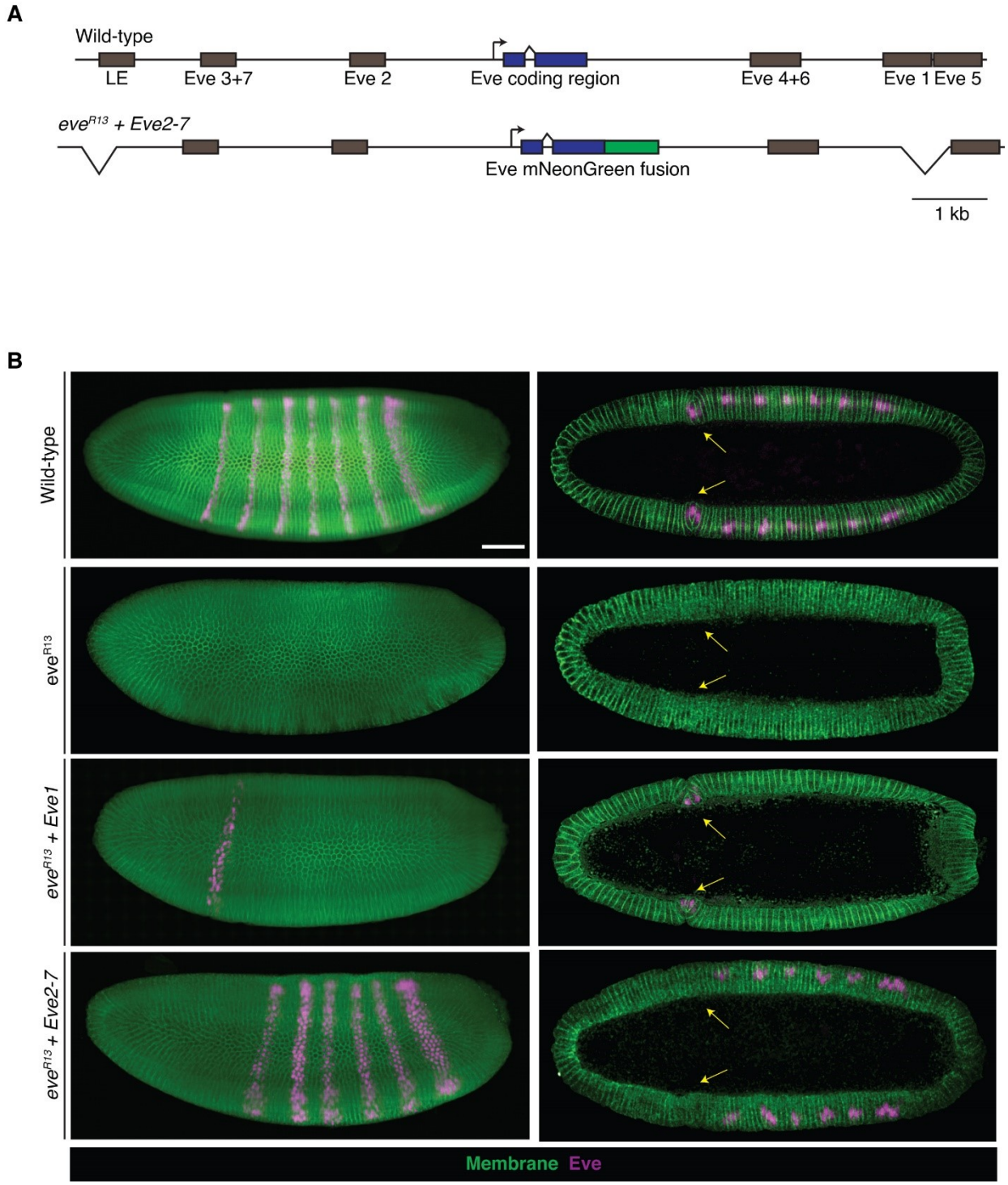
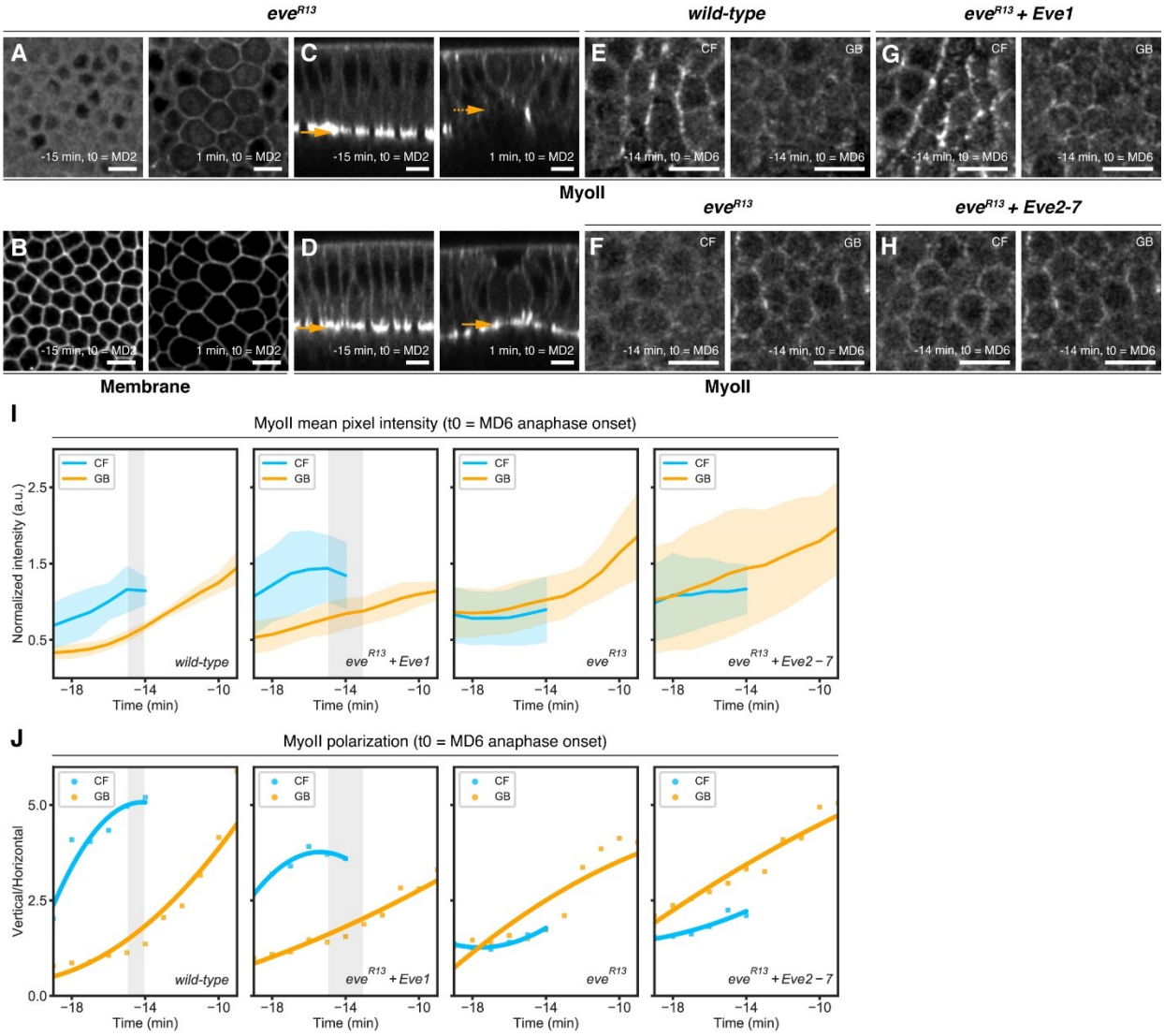

A
Wild-type
LE
Eve 3+7
Eve 2
Eve coding region
Eve 4+6
Eve 1
Eve 5
eveR13 + Eve2-7
Eve mNeonGreen fusion
1 kb
B
Wild-type
eveR13
eveR13 + Eve1
eveR13 + Eve2-7
Membrane Eve

Figure 11



note: scale bar = 10 um

Figure 12

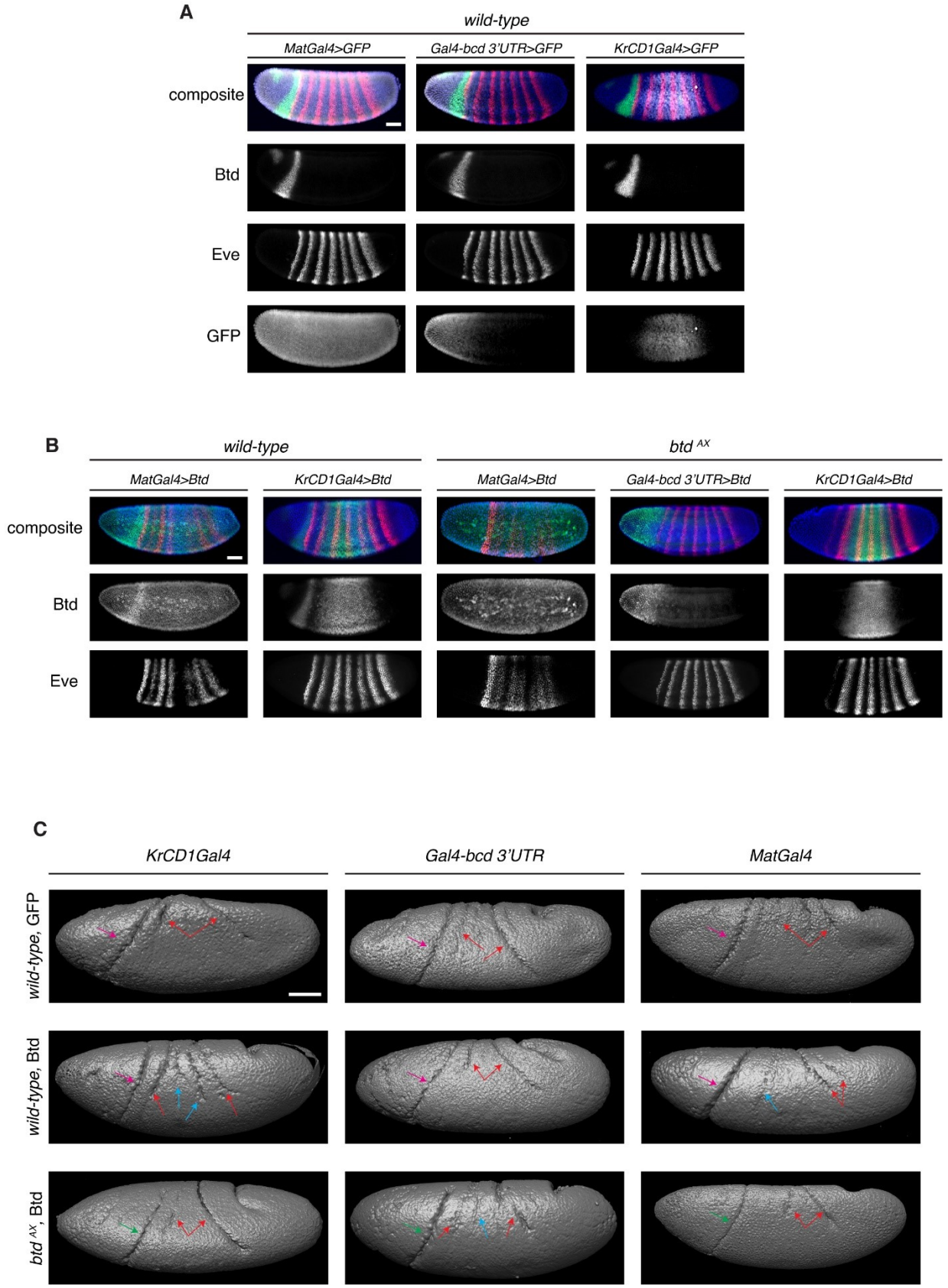
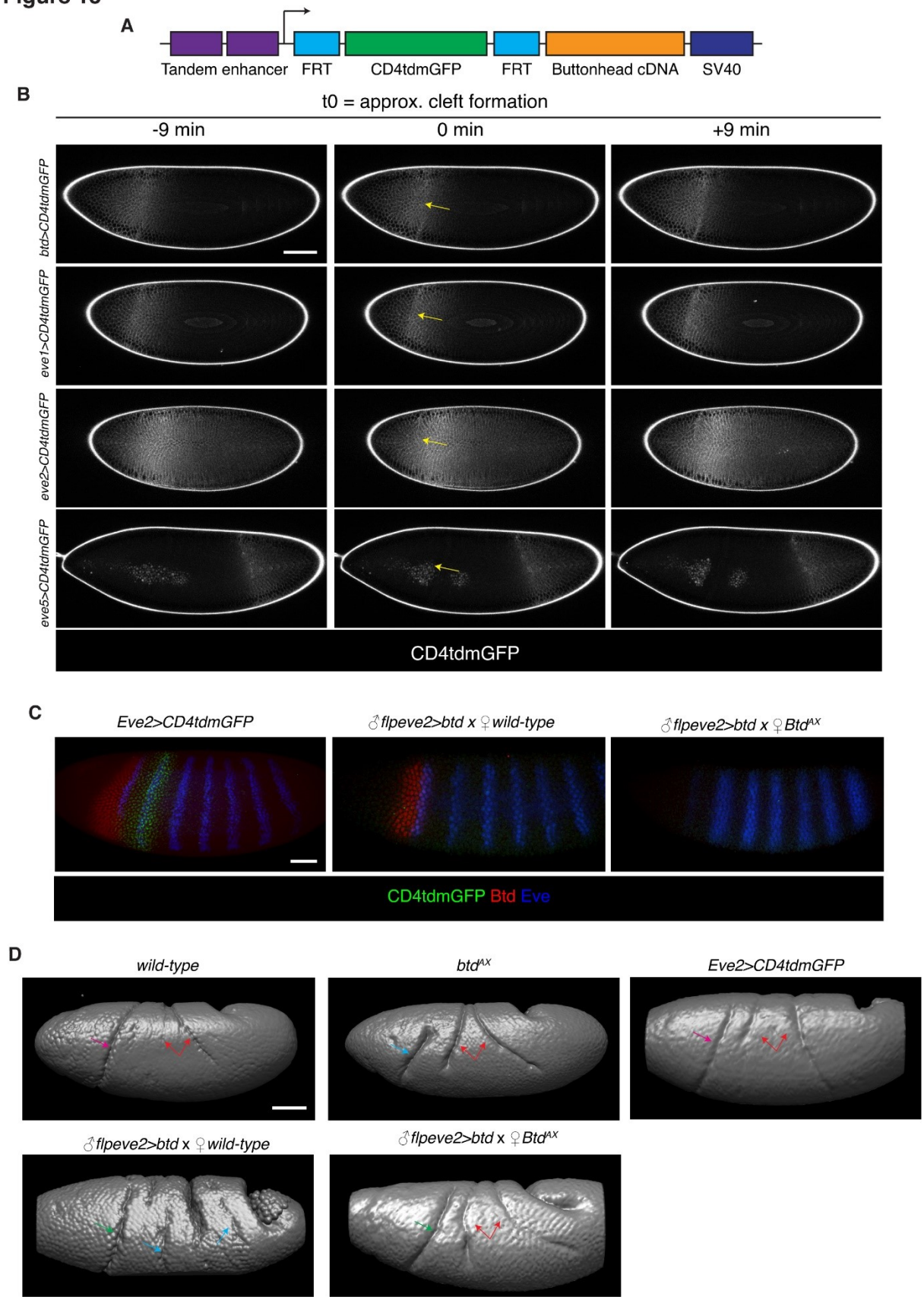
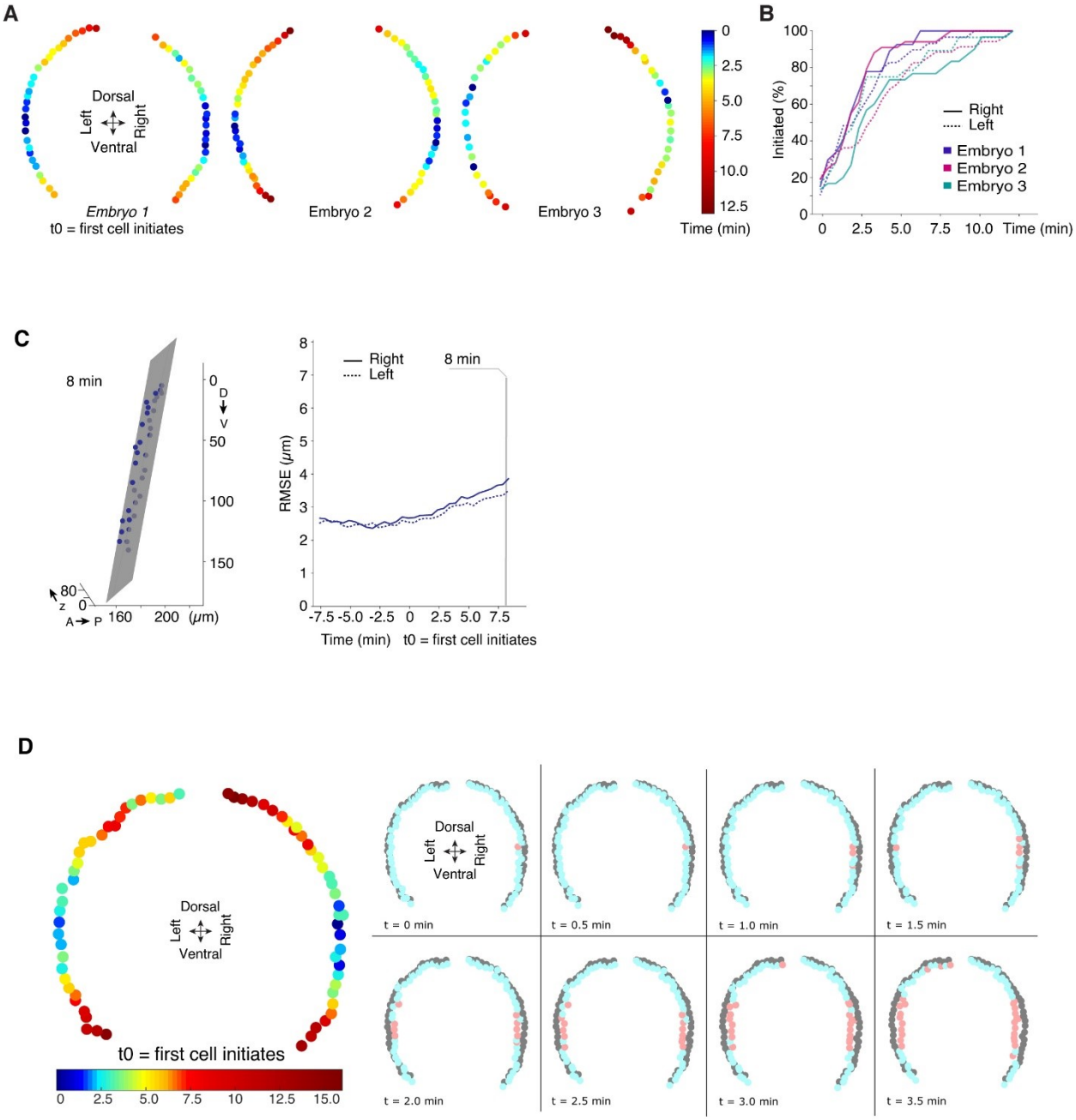

A
wild-type
MatGal4>GFP
Gal4-bcd 3'UTR>GFP
KrCD1Gal4>GFP
composite
Btd
Eve
GFP
B
wild-type
btd AX
MatGal4>Btd
KrCD1Gal4>Btd
MatGal4>Btd
Gal4-bcd 3'UTR>Btd
KrCD1Gal4>Btd
composite
Btd
Eve
C
KrCD1Gal4
Gal4-bcd 3'UTR
MatGal4
wild-type, GFP
wild-type, Btd
btd AX, Btd

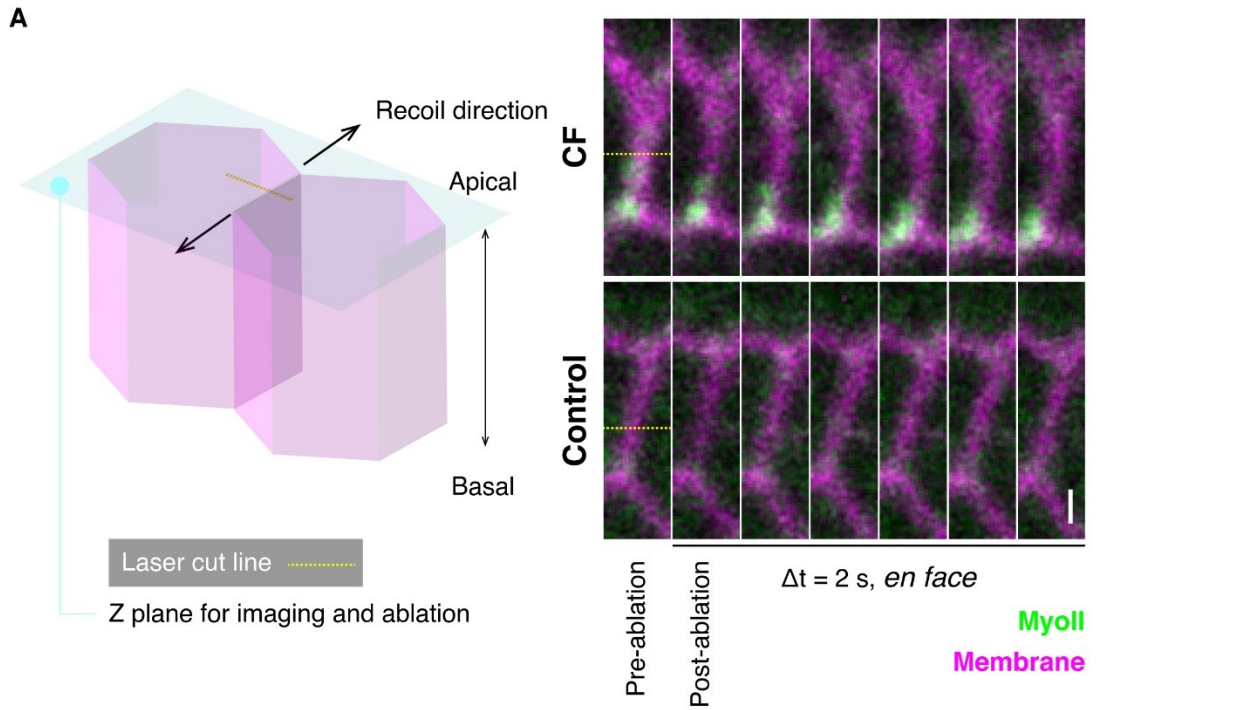
Figure 13

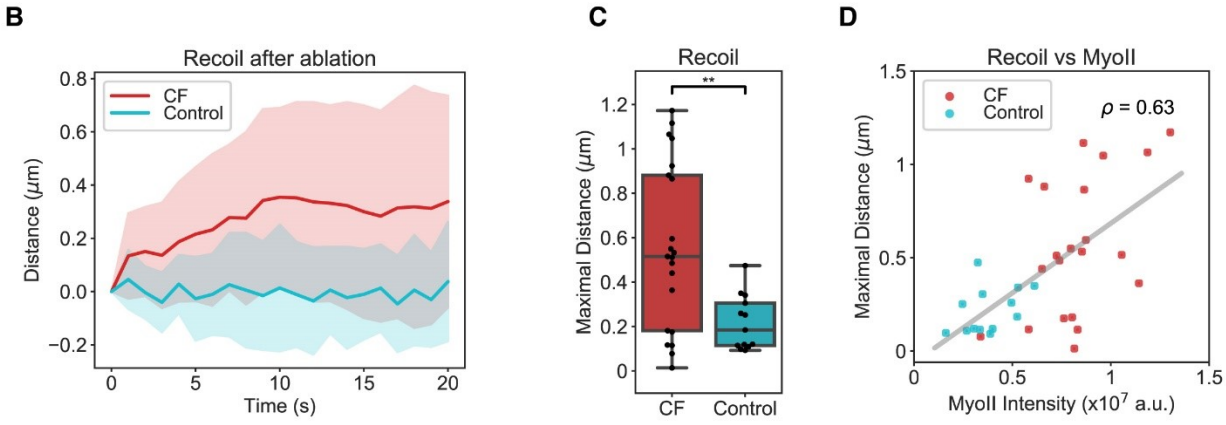

A
Tandem enhancer
FRT
CD4tdmGFP
FRT
Buttonhead cDNA
SV40
B
t0 = approx. cleft formation
-9 min
0 min
+9 min
btd>CD4tdmGFP
eve1>CD4tdmGFP
eve2>CD4tdmGFP
eve5>CD4tdmGFP
CD4tdmGFP
C
Eve2>CD4tdmGFP
♂flpeve2>btd x ♀wild-type
♂flpeve2>btd x ♀Btd^ΔX
CD4tdmGFP Btd Eve
D
wild-type
btd^ΔX
Eve2>CD4tdmGFP
♂flpeve2>btd x ♀wild-type
♂flpeve2>btd x ♀Btd^ΔX

Supplamental Figure 1

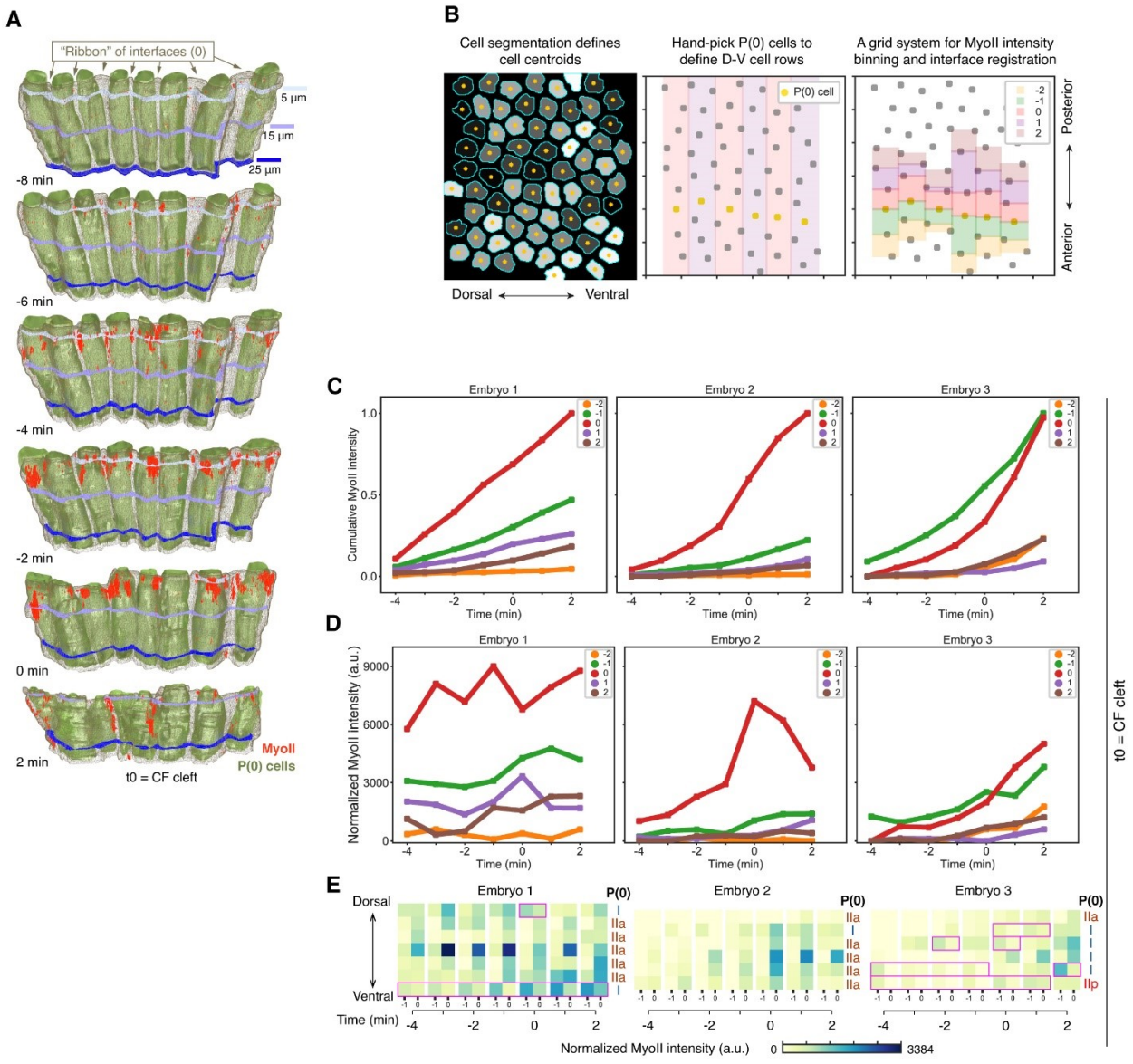


Supplamental Figure 2

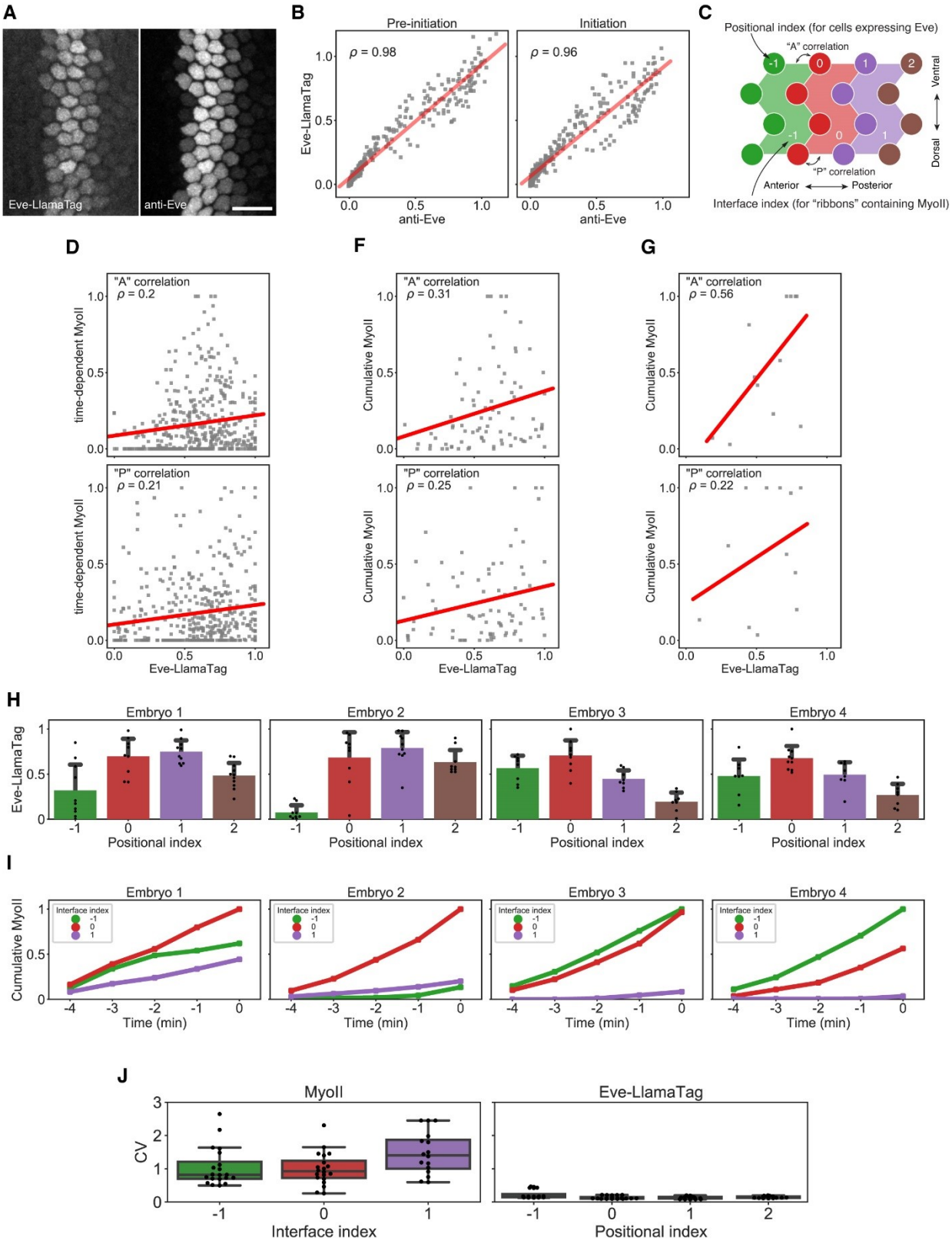




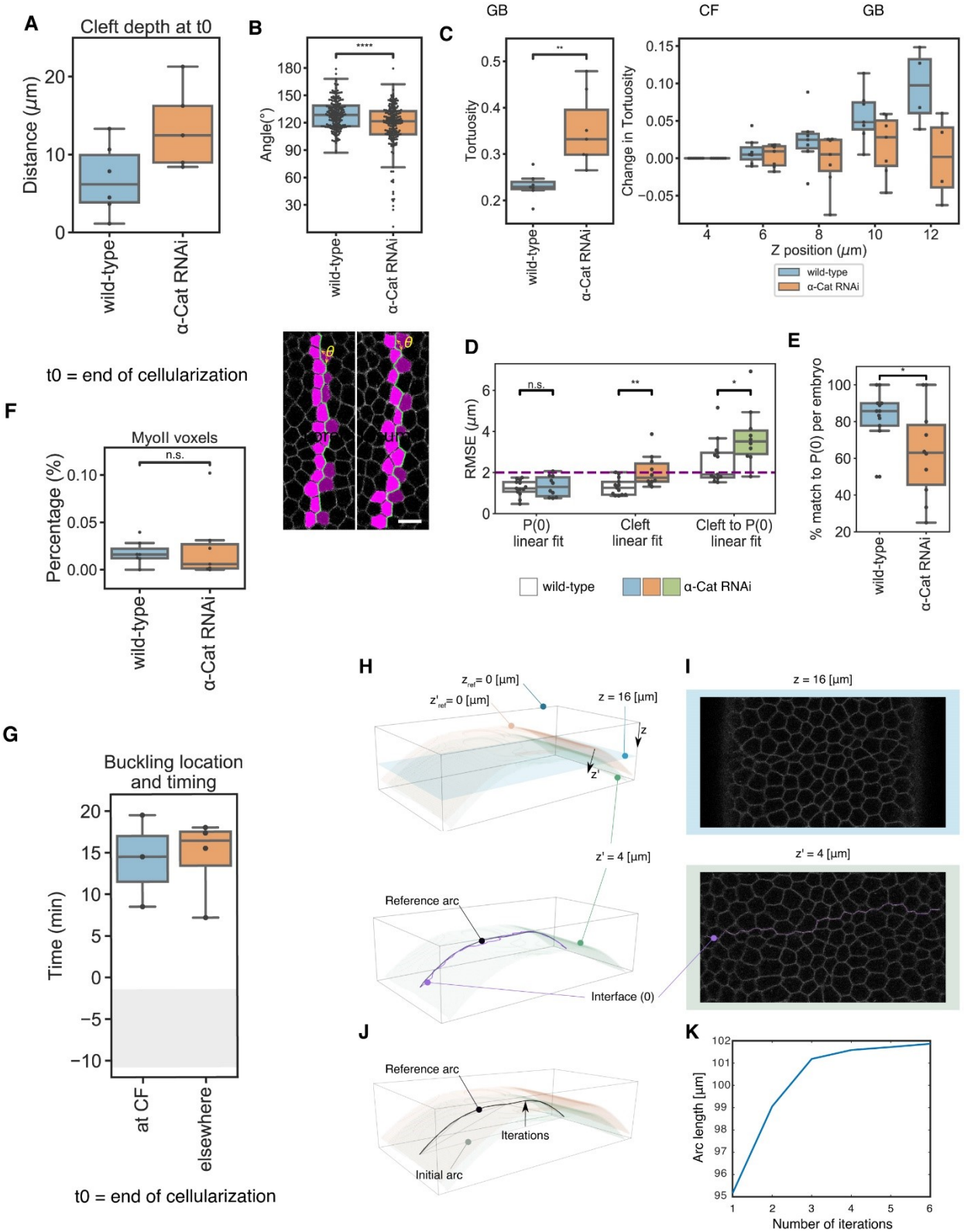
Supplamental Figure 3



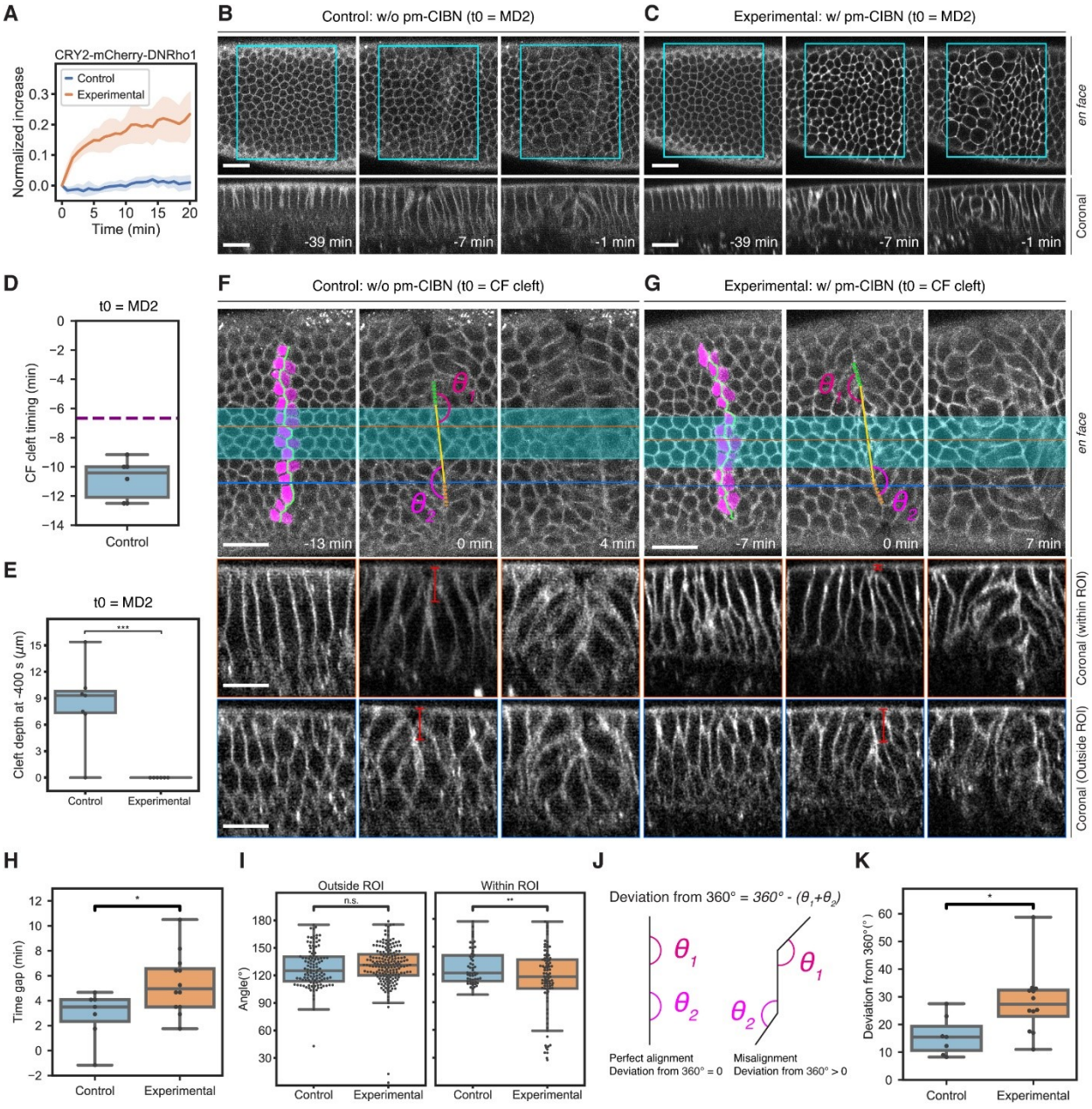
Supplamental Figure 4



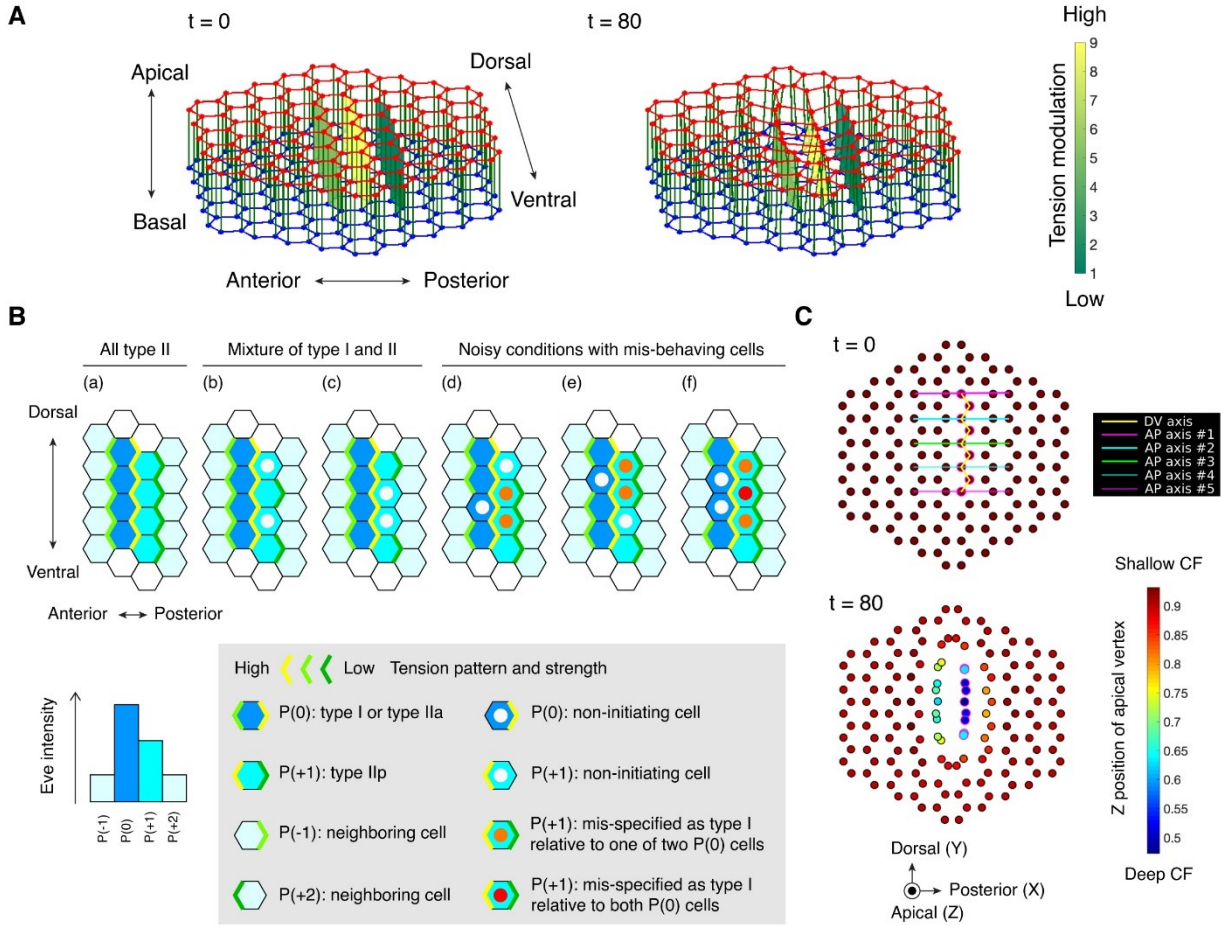
Supplamental Figure 5



Supplamental Figure 6



Supplemental Figure 7



Supplamental Figure 8

